Title
High-Fidelity Simulation and Low-Order Modeling of Bio-inspired Fluid Dynamics

Author
Wang, Chengjie

Publication Date
2014

Peer reviewed|Thesis/dissertation

University of California
Los Angeles

High-Fidelity Simulation and Low-Order Modeling of Bio-inspired Fluid Dynamics

A dissertation submitted in partial satisfaction
of the requirements for the degree
Doctor of Philosophy in Mechanical Engineering

by

Chengjie Wang

2014

Abstract of the Dissertation

High-Fidelity Simulation and Low-Order Modeling of Bio-inspired Fluid Dynamics

by

Chengjie Wang

Doctor of Philosophy in Mechanical Engineering

University of California, Los Angeles, 2014

Professor Jeffery Eldredge, Chair

Unsteady fluid dynamics at low to moderate Reynolds number, i.e. $O(10^2) \sim O(10^4)$, has drawn increasing attention during the past decades as a result of the growing interest in the biological and bio-inspired locomotion like the flying and swimming of different creatures. In this work, several numerical methods, including low-order modeling and high-fidelity simulations, are developed and explored, which target to explore and understand the moving capabilities observed in nature as well as provide general guidances for the future development of similar agile air/underwater vehicles.

In the first part of the work, a low-order point vortex model for the two-dimenional unsteady aerodynamics of a flat plate wing section is developed. The flow field is described by several point vortices, which can be divided into two categories. A variable-strength vortex is referred to the one just released from either leading or trailing edges of the sharp edge and the strength of each is determined by enforcing the Kutta condition at the edges. The vortex is moved into the second category when its strength reaches its extremum and is frozen. The motion of the fixed-strength vortices is easy to find according to the potential flow theory, while the motion of the vortices with variable-strength requires special evolution equations. Two ways are considered in our work. In the first approach,

the Brown-Michael equation is used in order to ensure that no spurious force is generated by the branch cut associated with each vortex. In the second approach, a new evolution equation for a vortex by equating the rate of change of its impulse with that of an equivalent surrogate vortex with identical properties but constant strength. The results of the new model, when applied to a pitching or perching plate, agree better with experiments and high-fidelity simulations than the Brown-Michael model, using fewer than ten degrees of freedom. The model performance is also assessed on the impulsive start of a flat plate at various angles of attack.

In the second part of the work, a strong coupling algorithm is presented for simulating the dynamic interactions between incompressible viscous flows and rigid-body systems in both two- and three-dimensional problems. The incompressible flow is solved by the vorticity-based immersed boundary projection method, and dynamical equations for arbitrary rigid-body systems are also developed. The resulting partitioned system of equations is solved with a simple, physically-motivated relaxation scheme, based on an identification of virtual inertia from the fluid. Several two- and three-dimensional numerical examples are conducted to validate and demonstrate the method, including a falling cylinder, flapping of flexible wings, self-excited oscillations of a system of linked plates in a free stream, passive pivoting of a finite aspect ratio plate in a free stream and gravity and self-propelled motion of a flexible flapping tail. The results from the current method are compared with previous experimental and numerical results and good agreements are achieved.

The dissertation of Chengjie Wang is approved.

Xiaolin Zhong

John Kim

Christopher Anderson

Jeffery Eldredge, Committee Chair

University of California, Los Angeles

2014

To my parents

Table of Contents

List of Figures

List of Tables

Acknowledgments

First of all, I would like to express my sincere gratitude and appreciation to my advisor Professor Jeff Eldredge for his continuous guidance, support, and encouragement during my doctoral study. His extensive knowledge, excitement for mechanics, and enthusiasm will always be my inspiration. I also thank Professor Chris Anderson, Professor John Kim and Professor Xiaolin Zhong for their constructive comments and guidance as well as serving in my doctoral committee. I am also indebted to Professor Zhenfu Tian from Fudan University, Shanghai, who introduced me to the world of computational fluid dynamics during my undergraduate study.

I'm grateful to have wonderful colleagues in SOFIA lab, Dr. Albert Medina, Dr. Maziar Hemati, Dr. Kwitae Chong, Ethan Young, Peggy Huang, Darwin Darakananda, just to name a few. Their helps and encouragements turned the lab to a comfortable place to work and stay. I would also like to acknowledge all of my friends for making my stay at UCLA such enjoyable and memorable. Special thanks are given to UCLA CSST program and Dr. Ren Sun for bringing me to this beautiful campus as an exchange student back to six years ago.

I also own my outdoor partners lots of appreciations for filling my leisure time with beautiful sceneries and great adventures. Especially, I want to mention my climbing partners, Cassie, Leo and Song, for belaying me all these years. Thank you for holding my life and not letting it go.

Finally, I want to thank my parents for their constant love and support all these years. This work is dedicated to them.

Vita

2009	B.S. (Mechanical Engineering), Fudan University, Shanghai, China.
2009–2014	Graduate Student Researcher, MAE Department, UCLA.
2013	M.S. (Mechanical Engineering), UCLA, Los Angeles, California.

Publications

C. Wang and J. D. Eldredge "Strongly coupled fluid/rigid-body dynamics in an immersed boundary projection method" *Submitted to J. Comput. Phys.*

C. Wang and J. D. Eldredge [2012], "Low-order phenomenological modeling of leading-edge vortex formation." *Theor. Comput. Fluid Dyn.*, 1-22.

M. V. OL, J. D. Eldredge, and C. Wang [2009], "High-amplitude pitch of a flat plate: an abstraction of perching and flapping." *International Journal of Micro Air Vehicles* **1**(3): 203-216.

J. D. Eldredge and C. Wang [2012], "Low-order modeling of biologically-inspired flight mechanics," Proceedings of the 23rd International Congress of Theoretical and Applied Mechanics, Beijing, August 2012

J. D. Eldredge and C. Wang [2011], "Improved low-order modeling of a pitching

and perching plate (invited)," 41st AIAA Fluid Dynamics Conference, Honolulu, June 2011, AIAA Paper 2011-3579.

J. D. Eldredge and C. Wang [2010], "High-Fidelity Simulations and Low-Order Modeling of a Rapidly Pitching Plate (invited)," 40th AIAA Fluid Dynamics Conference, Chicago, June 2010, AIAA Paper 2010-4281.

J. D. Eldredge, C. Wang and M. OL [2009], "A Computational Study of a Canonical Pitch-Up, Pitch-Down Wing Maneuver (invited)," 39th AIAA Fluid Dynamics Conference, San Antonio, June 2009, AIAA Paper 2009-3687.

CHAPTER 1

Introduction

The study of the unsteady fluid dynamics at moderate Reynolds number, i.e. $O(10^2) \sim O(10^4)$, is an interesting yet challenging fluid topic. Many biological and bio-inspired locomotions fall into this flow regime, like flight of small birds and insects, swimming of aquatic organisms. These locomotions are always associated with a wide range of maneuvers or large deformation of bodies/wings, which enables very quick and agile movements of these creatures. The agility in motion is also an important feature in the development of micro air vehicle (MAV) and autonomous underwater vehicle (AUV). However, the moderate Reynolds number brings the challenges to the research that the inertia and viscosity play equally important roles at flow behaviors. The nonlinearity is therefore introduced (according to the Navier-Stokes equation) and make it difficult to solve such problems.

Our work is divided into two parts to deal with these problems. The first part of our research is on the development of the low-order model of the biologically-inspired unsteady aerodynamics. The resulting two dimensional model is applied to simulate various plate maneuvers. The comparisons are made between our model and other methods, including experiments and high-fidelity simulations. The second part is on the construction of the high-fidelity simulation tool toward the fluid-structure interaction (FSI) problems. A strongly coupled algorithm is developed for simulating the dynamics interaction between incompressible viscous flows and rigid-body systems in both two- and three-dimensional problems.

Several numerical tests are conducted to validate and demonstrate the method.

In the following part of this chapter, a general overview of the unsteady fluid dynamics is discussed, including the multiple research methods and some significant phenomena observed. Chapters 2 and 4 mainly focus on two different low-order models and the corresponding results. The development of high-fidelity simulation tool is covered in Chapters 4 to 6, with results validation and demonstration. The concluding remarks and extension of future work is discussed in Chapter 7.

1.1 Research Approaches

1.1.1 Experimental Observation

Humans have observed hundreds of thousands of species of flying creatures in our world. Among them, insects prove themselves as experts in aerodynamic performance and maneuverability, especially for the flapping motion. Researchers started the averaged force measurement through delicate balances in the 1940s. Hollick [51] studied the flying insect in both 'still air' and a stream of air. The mean resultant of force was measured and different patterns of flapping were observed under different flow conditions. In 1965, Jensen [55] also measured the averaged force generated by a locust, and obtained detailed flapping movements. With the development of technology, the time-dependent force measure became available. Cloupeau et al. [17] used a piezo-electric probe to measure the instantaneous lift in flying locusts and found the discrepancy from the averaged one. Wilkin and Williams [129] made the force measurement through a strain-gauge probe. The results were compared with a quasi-steady model, and good agreement was achieved in upstroke. With the availability of flow visualization technology, researchers also started investigation on flow structures associated with insect flights. Ellington et al. [36, 130] studied the flapping insect wings by visualizing

the flow and argued that leading-edge vortex with sufficient strength is the source of high lift force. This vortex is believed to be created by dynamical stall rather than the rotation and stabilized by spanwise flow along the wing. Srygley and Thomas [107] performed the experiments on trained butterflies to investigate the mechanisms of force generation. Flow visualizations indicated that various unconventional aerodynamic mechanisms are responsible for generating force, while none of them can be regarded as 'key' to insect flight.

However, all these experiments are done on living insects, whose movements are different for each individual. This introduces significant uncertainties into the force measurements of a single wing. In order to obtain more accurate measurements and more direct comparison between airfoils and wings, researchers have made their efforts to build their own flapping wing devices. Van den Berg and Ellington [120] built a robotic model which mimics the 'hovering' motion of a hawkmoth. Flow visualization and detailed analysis were able to be conducted and proved the dynamic stall is responsible for high lift generation. A systematic series of experimental investigation were first brought by Dickinson and Götz [27], which provided precise data of the unsteady force generated by wings. This experiment focused on a simple and canonical motion, rapid acceleration from rest to a constant velocity at a fixed angle of attack, in the moderate Reynolds number regime ($10 < Re < 1000$) consistent with small insect flight. The wing model used was a rectangular wing section, while the force on the wing was measured by a two-dimensional force transducer. An unsteady process of vortex generation at large angle of attack was believed to be the source of aerodynamic force generation. Particularly, the attached leading-edge vortex at angles of attack larger than 13.5° is argued to contribute 80% increase in lift at the first 2 chord lengths of travel. As a follow up of the previous two dimensional study, Dickinson et al. [28] extended their experimental setup to three dimensions, including insect-like wing shape and the rotational motion. The rotational circulation and wake capture mechanisms

were investigated and shown to be provide two additional contirbutions to insect flight. Lentink and Dickinson [69, 68] performed an investigation on the stability of the leading edge vortex via experiments on an insect-like plate (air bubble visualization and force measurements) as well as simulation. Rossby number, the ratio of inertia to Coriolis force, was chosen as an important parameter to characterize the attachment of the leading-edge vortex. They found that the Rossby number of flies is about $Ro = 3$ which is quite general for most wings and fins in nature.

In addition to the experiments on insect-like wings with complicated motions, researchers have also performed experiments with simple geometry (flat plate) and motions (translation, pitching-up or pitching-down) to investigate some basic flow phenomena. Ringuette et al. [96] studied the unsteady vortex formation through experiments on a low-aspect-ratio flat plate. The plate moved in a simple translating start-up. The tip vortex was proved to be the source of a maximum in the plate force. Granlund et al. [47] conducted experiments on abstractions of perching. The motions consist of pitching from $\alpha = 0^\circ$ to 45° for a SD7003 airfoil and pitching from $\alpha = 0^\circ$ to 90° for a flat plate. A large number of cases were analyzed to explore the effect of axis location, rotational rate and angle of attack.

1.1.2 Theoretical Analysis

Theoretical analysis on force of insect wings has been attempted for almost a century. Most of them are conducted through the investigation on similarities and differences between an insect wing and a classical airfoil. Weis-Fogh and Jensen [128] started a series of reviews on the study of locust flight. At that time, most of the analyses were done under the quasi-steady assumption that instantaneous force is determined only by current motion and not related to the history. Later, Weis-Fogh [127] proposed the clap-and-fling mechanism to explain the high lift production in the hovering animals. This mechanism in *Locusta* flight was also observed and filmed by Cooter and Baker [19]. Lighthill [71] and Sunada et al.

[109] gave detailed theoretical analysis on the mechanism in two dimensions and three dimensions respectively, while experimental investigations were performed by Bennett [6], Maxworthy [78] and Spedding and Maxworthy [106]. In theoretical analysis, the models were essentially inviscid and included the viscous effect via the shedding of the vortex.

Von Karman and Sears [122] derived a theoretical model for two dimensional fluttering airfoil. Only a trailing edge vortex was included in the analysis, and they were released at every interval and restricted to a horizontal line behind the airfoil. The results agree well with experiments for small angle of attack. As for the effect of leading edge vortex, the exact solutions for flow over a wing was first presented by Saffman and Sheffield [98]. A free vortex is assumed to stand over the wing and its location and strength are then obtained through two-dimensional inviscid potential flow theory. The lift on the wing was shown to be significantly increased by the free vortex.

Although the theoretical work brings researchers tremendous simplification and insight into the problem, it is hard to break the problem into such easy and simple small parts that we can solve by hand, yet remain faithful to the physics. The computational requirement of a sophisticated theoretical model is still intensive.

1.1.3 Computational Approaches

With the development of computational capability, researchers pay increasing attention to computational approaches, either the detailed calculation of previously developed theoretical model or computation based high fidelity simulations.

1.1.3.1 High Fidelity Simulation

High fidelity simulation is a good way to reveal and investigate detailed flow features carefully. The manner is to solve the Navier-Stokes equations directly without any simplification. There are a large number of high fidelity methods which can be divided into several families based on the grids used.

The first and probably the earliest family of methods are developed via stationary, body-fitted computational grid, in which the reference frame is changed to one moving with the body. Gustafson and Leben [48] applied the method to a 2D single hovering airfoil and obtained excellent spatial and temporal correlation with laboratory studies. Later, Wang [125] improved the method with a high-order numerical scheme for the study on forward flapping wing.

The second family is also based on body-fitted grid. The difference from the previous one is that it is no longer stationary but time-dependent, along with the body movement. Sun and Tang [108] conducted a three-dimensional simulation for the flow around a fruitfly wing through this kind of grid. The results were compared with the experiments by Dickinson et al. [28]. Liu and Kawachi [74] simulated the three-dimensional flow field around a hawkmoth's wing undergoing flapping motion in a similar method. The model successfully captured the important leading-edge vortex structure. In addition to the finite difference algorithm, a finite element solution has also been introduced to this kind of grid. Ramamurti and Sandberg [92] employed a finite element method to compute three-dimensional flow around a fruitfly's wing and good force prediction was achieved compared with a previous experimental study. An arbitrary Lagrangian-Eulerian (ALE) form of the governing equations was applied to enable the near-wing grids to move as the wing does.

Although the body-fitted grid allows an easy and direct enforcement on boundary conditions, a big challenge lies in grid generation, especially for the large

displacement and deformation associated with insect flight. In the third family, researchers choose a regular Cartesian grid and immerse the boundary into it. As for the treatment of the boundary, it can be enforced through interpolation of the surface velocities to nearby grid points, which is regarded as a 'direct forcing'. Another way is to enforce it indirectly by setting some sort of singularity distribution (such as forcing terms or a vortex sheet). Udaykumar and Mittal and coworkers [132, 118, 84] developed a finite volume method, which uses a direct Cartesian grid boundary enforcement in both two and three dimensions. Balaras [5] introduced a novel interpolation of the boundary treatment into three dimensional immersed boundary method, which helps to preserve the overall accuracy of the scheme. On the other hand, Peskin [88] chose the indirect approach to treat boundary condition in the study of blood flow in the heart, where the elastic boundary is replaced by singular distribution of force. A more accurate approach was developed as a follow-up by Lai and Peskin [67], which is shown to have less numerical viscosity. Based on this method, Miller and Peskin [82] explored the classic 'clap and fling' stroke and 'fling' half-stroke at low Reynolds number. Taira and Colonius [110, 18] applied boundary force acting as a Lagrange multiplier to the boundary treatment and used a projection to eliminate slip and non-divergence-free components of the velocity fields.

The fourth family is particle-based computational methods, which have great differences with previous grid-based schemes. Among them, vortex particle methods are widely used for inviscid simulations of aerodynamics, as the vortex is regarded as a basic flow structure in physics. The advantages of this kind of method is that no finite flow region needs to be specified for simulation, so that flow around objects with large movements, like flapping wing, is no longer an obstacle. However, the means for enforcing boundary conditions needs more attention, as it is less straightforward. Koumoutsakos [63] reviewed most of vortex particle methods and their use on multiscale flow simulations. Eldredge [31, 32]

developed a viscous vortex particle method (VVPM) for viscous flow around both rigid body and coupled fluid-body interactions. This method is used in the present work as a reference tool for low-order model. Zhang and Eldredge [134] extended VVPM to continuously deforming two-dimensional bodies, like undulating fishes. In three-dimensional study, Winckelmans and Leonard [131] reviewed several contributions to vortex particle methods, both singular and regularized. They provided a version of the regularized method which can account for viscous diffusion by redistributing the particle strength vectors.

1.1.3.2 Low-Order Models

High fidelity simulations provide us a detailed flow field which can be investigated carefully. However, the requirement of computational time and capacity is intense, as the number of degrees of freedom is usually larger than $O(10^5)$. Due to the cost of computation, this kind of model is not suitable for some real engineering problems, like control, optimization etc. We hope to construct some low-order models whose number of degrees of freedom is much smaller but still give a reasonable prediction on some specific target outputs, like force and moment, for the purpose of control and optimization.

Researchers in fluid dynamics have recently drawn from tools developed in dynamical systems theory in order to simplify complex fluid flows. For example, the method of Proper Orthogonal Decomposition (POD) can be used on results from an experiment or high fidelity simulation. Then, a reduced model can be built by selecting a small number of modes. This method was first proposed in the study of turbulent flow. Rempfer [94, 95] reviewed the low-dimensional Galerkin model and its application in turbulence and shear layer study. Brunton and Rowley [10] obtained POD mode via Galerkin projection of the Navier-Stokes equations. It was shown that a two degrees of freedom model is able to capture the laminar vortex shedding behind a plate at high angle of attack. In a following study [12],

they provided an improved method, the eigensystem realization algorithm (ERA), to derive the model. The method is proved to be more efficient to compute and more suitable for incorporation into a flight control method. For pitching and plunging test cases, an ERA model of order 4 and 6 was sufficient to capture Wagner's indicial response. However, the method requires linearization about a flow condition, and therefore is only suitable for small departures from this condition.

From the fluid point of view, researchers have often relied on inviscid vortex models and tried to represent the flow with a small number of point vortices or vortex sheets. Sarpkaya [100] used a discrete point vortex method to study the vortex shedding behind an inclined flat plate in two dimensions. Potential flow theory and Joukowsky mapping are used in the derivation of the method and the classical Kutta condition is required at two sharp edges. In the calculation, the point vortices were shed from these two edges at every time step, and their circulation was determined by the velocity difference at each edge. The results indicated that the model did a fairly good job in predicting flow patterns and over-predicted the force by 20% compared with experiment. Kiya and Arie [62] attacked the same problem with a slightly different method. In their method, point vortices are released from some fixed points near the edges, but the Kutta condition still needs to be satisfied. An appropriate choice of the nascent vortex position helped to match force prediction. Other than the classical Joukowsky transform, a vortex sheet is also used to represent objects with complex shape or deformation, which cannot be transformed by conformal mapping. Katz [61] used a discrete vortex method to model the flow around a cambered airfoil which is represented by a vortex sheet. The location of the separation point is given by experimental of flow-visualization data. However, all these methods model the shedding of vorticity from a sharp edge by introducing new vortex elements, whose strength, position and velocity are chosen arbitraily to match the results

from experiments. As Sarpkaya [101] remarked in his review paper, 'almost every paper, at least in part, represents a new method.'

In 1993, Cortelezzi and Leonard [23] studied the two dimensional unsteady separated flow past a semi-infinite plate with various strength point vortex model. A great improvement of this work is that they introduced an asymptotic means to release new vortex elements for a power-law starting flow. Later, Cortelezzi [20] gave a more detailed derivation of the starting vortex motion, which is determined by the Brown-Michael equation [9]. This approach is less ad hoc than previous ones, and it has been used and improved in following work. Jones [57] applied the asymptotic solution to the vortex sheet method for the derivation of small time vortex behavior in the study of separated flow around a plate. Jones and Shelley [58] investigated the motion of falling cards with the same numerical method. A similar numerical model was used to study the accelerating plate at fixed incidence by Pullin and Wang [91]. The governing equation modeling evolution of vortex sheets is the Birkhoff-Rott equation, which was developed for the generation of finite vorticity at a wedge in hypersonic flow [97]. Shukla and Eldredge [103] developed an inviscid vortex sheet model for flow past a deforming body. In addition, Ansari et al. [3, 4] developed a similar vortex method which considers the general motion of insect wing flapping and can be extended to three dimensions by a blade-element method.

Although the number of degrees of freedom has been greatly decreased in these vortex models, it is still not practical to fit them into a control system for a real engineering work. To further reduce the number of degrees of freedom, we can enforce some constraints on vortices for some specific problems. For example, in the study of non-uniform flow around an airfoil at low angle of attack, von Karman and Sears [122] neglected the leading-edge vortex contribution and constrained the vertical position of the trailing-edge vortices. In this way, the force is calculated by counting the effect into a "wake" of vorticity and good agreement was achieved.

Recently, Tchieu and Leonard [112] provided an one-equation aerodynamic model with similar assumptions made by Von Karman and Sears. In their model, fewer point vortices are released yet better agreement is obtained, especially for the early time Wagner effect.

Another reason preventing the model from control strategies is the increase of point vortices along with time. To overcome this problem, researchers have tried to cluster point vortices into one vortex, whose strength is time dependent. However, this introduces a problem in the model. For two-dimensional problems, the unsteady vortex strength will introduce a multi-valued time derivative of the velocity potential, which results in an unbalanced force and moment, which is non-physical. To resolve this problem, Brown and Michael [9] provided a governing equation for this kind of vortex in their study on a hypersonic delta wing, so that the unbalanced force can be canceled out by the movement of the vortex. Howe [53] derived another form, which is designed to eliminate the unbalanced moment. Different flow features were revealed in this form in the study of sound generation. Recently, Michelin and Llewellyn Smith [79, 80] developed a point vortex method based on Brown-Michael equation for the study of coupled motion of a general sharp-edged solid body with the surrounding flow. Good results were obtained with only 5 point vortices in the flow from a falling card; the model has also been used to study the flow past a flapping flag [80]. Rather than use the Brown-Michael equation, Minotti [83] investigated a flapping wing with only two point votices, whose strengths are determined through experiment. Qualitative agreement is achieved for flapping motion, but a discontinuity in the force occurs at the start of reverse translation.

1.1.3.3 Relation Between High Fidelity Simulation and Low-Order Model

The essence of high fidelity simulation is to solve the full Navier-Stokes equations without any simplification. Usually, only basic flow properties are retrieved as results, like velocity field (or vorticity field), pressure and density. Providing an appropriate and precise interpolation of these quantities is an essential work in the analysis. This shares many common elements with experimental results analysis. On the other hand, in most physics-based low order models, some simplifications have already been made to omit the minor effects, so that the flow features we are interested in are highlighted. In this way, instead of solving the full Navier-Stokes equations, researchers calculate the governing equation derived for the flow features, like point vortices, which saves significant computational expense. However, for a priori models, it can be difficult to make direct comparison of flow behavior with high-fidelity results, because their relationship is not clear.

An alternative way to relate a low-order model to high fidelity simulation is to collect information from high fidelity results and reduce it to provide an empirical formula for low-order model. For example, in the study of pitching plate, high fidelity simulation provides us a complete flow field. We can characterize it by several vortices, such as the leading-edge vortex, trailing-edge vortex, wake vortex, etc. Then, we can pass the strength and position of all these vortices to low-order model to reproduce the dominant flow features. Further, if we are able to abstract empirical formulas for all these vortices, a new low-order model is then created. For this approach, the difficulty lies in the characterization of the high fidelity flow field. An unambiguous method to divide the flow field plays a key role here. Therefore, Lagrangian Coherent Structures (LCS) have drawn many researchers' attention. An LCS is a ridge of the finite-time Lyapunov exponent (FTLE) field, which characterizes the amount of local stretching of the flow map. The FTLE field provides us information about where the fluid particles come from are headed

to, and its ridges are material surfaces in the flow. Therefore, the LCS helps us to define the vortex region in experimental and numerical data. Mohseni and co-workers used this tool to study the flow structure behind jellyfish [72] and two-dimensional airfoil [13]. However, the calculation of the FTLE field or LCS is intensive, as a long time integral of flow map is needed for every time step. To resolve this problem, Lipinski and Mohseni [73] developed an efficient ridge tracking algorithm to calculate the LCS. Only the FTLE field near the possible position of the LCS is calculated to save the time. Brunton and Rowley [11], on the other hand, put their attention on the time-consuming flow map integral in the calculation of FTLE field. They conducted a standard computation of FTLE at each time step, and approximated the flow map through interpolation. In this way, there is no need to reload the velocity data, which is usually a large dataset. Then, a significant amount of time is saved.

1.2 Important Phenomena in Unsteady Fluid Dynamics

The history of the research work on insect flight was briefly reviewed in previous sections. Here, we want to highlight some important phenomena and flow structures in unsteady aerodynamics, many of which are observed in biological flight and would need to be embodied in a model of these mechanics.

1.2.1 Wagner Effect

In 1925, Wagner [123] first revealed that an inclined wing does not acquire its steady state circulation immediately for impulsive starting from rest. Instead, the circulation rises to the steady-steady asymptote. This is also confirmed by experiments done by Walker. This phenomenon is often referred to as the Wagner effect. According to Sane [99], this effect can be attributed to two factors. First, it takes time to satisfy the Kutta condition at the stagnation point due to inherent

latency in viscous action. Second, the formation of the starting vortex, which is rolled up from the vortex sheet shedding from the trailing edge, needs time. Consequently, the wing attains its maximum steady circulation only after the starting vortex is sufficiently far from the trailing edge. The schematic diagrams of the Wagner effect is shown in Fig. 1.1. This phenomenon causes forces in real flow below levels predicted by quasi-steady models. However, little evidence is achieved in experiments both in 2D [27] and 3D [28]. Basic simulations of an accelerating plate have been performed by Pullin and Wang [91] and Chen et al. [15] through both high fidelity simulation and Pullin's asymptotic model for a spiraling vortex sheet. The results partially confirm the growth of circulation but the trend does not follow Wagner's prediction exactly. Recently, researchers focusing on flapping wing tend to neglect this early stage effect in their models.

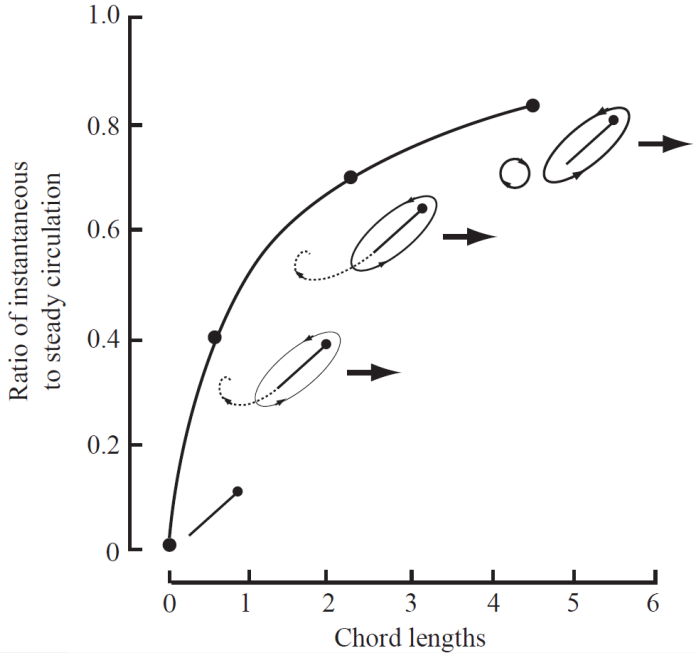

Figure 1.1: Wagner effect graph from Sane [99]. The ratio of instantaneous to steady circulation (y-axis) grows as the trailing edge vortex moves away from the airfoil(insect), and its influence on the circulation around the airfoil diminishes with distance (x-axis). Dotted lines show the vorticity shedding from the trailing edge, eventually rolling up into a starting vortex. As this vorticity is shed into the wake, bound circulation builds up around the wing section, shown by the increasing thickness of the line drawn around the wing section.

1.2.2 Delayed Stall

From conventional aerodynamics, we know that stall occurs when an airfoil exceeds its critical angle of attack, which in turn causes a great reduction in lift and increase in drag. However, in the study of wings at the Reynolds number appropriate to insects, stall does happen immediately when the large angle of attack is reached. Instead, the lift is enhanced by the presence of a vortex shed from the leading edge for a short period before it finally decreases into stall status. This phenomenon is called 'delayed stall'. Maxworthy [78] first visualized the leading-edge vortex in an experiment with model wings. In order to explain the unsteady aerodynamics causing this phenomenon, we will use a two dimensional translation motion as an example. When the wing starts translating at a high angle of attack, the leading-edge vortex grows in size until the flow reattachment is not possible any more. At this point, the leading-edge vortex is pinched off and shed into the wake. The lift benefit from the suction of this vortex is therefore lost, then the wing is said to have stalled. For conventional aerodynamics, the high Reynolds number at the order of $O(10^8)$ makes this process too fast to be noticed. On the contrary, at a lower Reynolds number applicable to insects, the process persists for for several chord lengths of movement. As a result, insects are able to achieve significantly enhanced lift from 'delayed stall' due to the new leading-edge vortices shed every half stroke for the flapping motion.

1.2.3 Added Mass

Added mass effect is a force relating to object acceleration. When an object accelerates in fluid, the fluid surrounding it must also be accelerated. According to Newton's second and third law, an extra fluid force is exerted on the object which has the same strength as the one needed to accelerate mass of fluid. In the derivation, this force can be decomposed to a mass term multiplied by an

acceleration term, where the mass is referred to as 'added mass'. In aerodynamics literature, it is also known as 'added mass inertia', 'acceleration reaction' or 'virtual mass'. This force is regarded as non-circulatory force as it has no direct relation with the circulation generated in the fluid. However, as the circulatory and non-circulatory force generally occur together, it is hard to isolate them in experimental measurements or direct numerical simulation analysis.

However, in the low-order models, there are several ways to calculate the added mass force according to different models. In the irrotational flow model, it is not hard to obtain the added mass effect for simple objects, such as a plate, cylinder, ball etc. The added mass coefficients have already been derived and can be found in the literature. In rotational flow, flow around objects may be mapped from that of a simpler shape – in which ambient vortices are accounted for by images – or computed directly with a bound vortex sheet. The magnitude of the bound vortex is related to the vortex in the wake according to Kelvin's circulation theorem as well as the object motion. The added mass force and moment can be calculated through the time derivative of the first and second moment of the bound vortex sheet associated with the object motion. However, it is not a easy job to obtain such vortex component responsible to added mass, which is almost impossible in high fidelity simulation. In the early model developed by von Karman and Sears [122], the wake and thus the bound vortex are represented in a very simple analytical way, and the contribution of added mass (called apparent mass in the paper) is calculated directly. In some other works, the direct calculation is not trivial, as the integral can be complicated. The added mass contribution has been central to several investigations of unsteady aerodynamic (or hydrodynamic) flows, including Wagner [123], Pullin and Wang [91] for plate, and Nair and Kanso [86], Eldredge [33] for a more general system including multi objects.

1.2.4 Span-wise Flow and Stability of Leading Edge Vortex

In the study of three-dimensional flapping wing, the flow structure becomes even more complicated with the variation in the span-wise direction. Span-wise flow and tip vortices are are important contributors to the force generation of a flapping wing and have been the target of several investigations attracting a lot of attention. Through the experiment conducted by Maxworthy [78] on three-dimensional fling, span-wise flow was observed and believed to be the reason causing variation of the leading edge vortex along its axis. Furthermore, this axial flow also feeds vorticity from the separation vortex into the tip vortex. Ellington, van den Berg and their co-workers [36, 120, 130] performed experiments on a hawkmoth and first visualized the flow field with smoke. A clear leading edge vortex with a large axial velocity component was observed in experiments, which partially revealed the three-dimensional flow structure. Consequently, many researchers have concluded that the span-wise flow in the separation vortex carries momentum from it and feeds the tip vortex, which limits the growth of leading edge vortex and prevents it from detachment, all illustrated in Fig. 1.2. (A smaller separation vortex allows the fluid to reattach more easily and the wing can sustain this reattachment for a longer time.) Later, Dickinson and co-workers [8, 69] built a robotic wing to study leading edge vortex and its attachment and stability. In [8], they followed the hypothesis given by previous researchers that span-wise flow is key to limit the growth of leading edge vortex and conducted several systematical test. By limiting the span-wise flow by fences and baffles, no detachment of the leading edge vortex was observed. As a result, they provided an alternative hypothesis on the robustness of the leading edge vortex – that down ward flow induced by tip vortices limits the growth of the leading edge vortex. In [69], scaling of parameters was investigated and Rossby number was revealed as an important parameter to determine the robustness of the leading edge vortex.

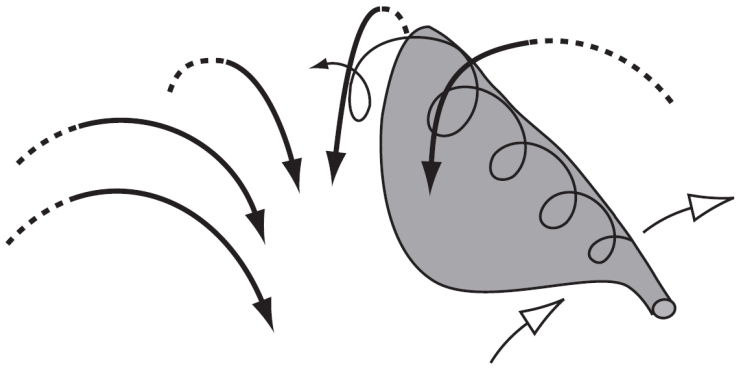

Figure 1.2: One hypothesis on stable attachment of the leading edge vortex. As the flapping wing translates, a span-wise velocity gradient interacts with the leading edge vortex, causing the axial flow to spiral towards the tip. The axial flow transports momentum out of the vortex, keeping it stably attached and also feeding the tip vortex. The vortex detaches at about three-quarters of the distance to the wing tip and is shed into the wake. Thick black arrows indicate downwash due to the vortex system generated by the wing in its surrounding fluid. Figure adapted from Sane [99]

1.3 Control Strategy

The purpose of low-order model development is, at least in part, to form an accurate and efficient characterization of the plant for application of control strategies. Vainchtein and Mezić [119] and Protas [90] have provided reviews in the control algorithms for vortex-based flow. Vainchtein and Mezić presented a short summary of control of vortex dynamics and their methods for control of vortex elements. Protas did a more thorough job in reviewing point vortex systems in both properties, like dynamics and equilibria, and construction of the actual control method. For the former aspect, basic knowledge and governing equations are introduced briefly at first. Then the 'Föppl system' is chosen as a simple example for the demonstration of existence of vortex equilibrium. Further, this question is discussed in flow with fixed separation points, such as corners or cusps, so that the well known Kutta condition is included. The paper brings problem of vortex equilibrium in 'Kasper wing', which has a cornice-shaped cavity on the top

surface of an airfoil to capture a vortex. The stability of the vortex equilibrium in 'Föppl system' was presented, using small perturbation analysis. The control of the vortex is the next subject that was discussed in the paper. Examples of controlling vortices interacting with plates have been pursued by Cortelezzi and co-workers [24, 21, 22], Anderson et al. [2] and Zannetti and Iollo [133]. All these results reveal a promising future to develop a point vortex model that is compatible to control strategy.

CHAPTER 2

Low-Order Modeling

2.1 Introduction

Bio-inspired locomotion, like flapping, has drawn increasing attention from engineers during the past decades. People are amazed and inspired by the flapping wing made of flight for its elegance and breadth of maneuverability, which are shown by a large number of flying creatures. In the development of micro air vehicle(MAV), such an inspiration has become a promising approach. Compared with the traditional flight vehicles, MAV shows its advantages in a lot of aspects, because of its small size.[105, 104] There are almost no storage and take-off requirements for MAVs. They can be stored anywhere they fit, like a small box, rather than a large hangar. No airport is needed as taxiing is no longer essential for taking off. Also, their insect-like size makes them extremely portable and easy to camouflage. This paves the way to their use as reconnaissance devices for military personnel and rescue teams. The small size also allows MAVs to fly in some small regions, such as indoor spaces, for searching. The low energy consumption should be a plus as well [105].

Although flapping-wing MAVs are believed to be a useful tool, we need to overcome some challenges for their practical construction. First of all, a comprehensive and simple aerodynamics theory is still missing in this low Reynolds number regime. As the classical aerodynamic theory is no longer applied, a good model of flapping flight should be established and tested to ensure a better understanding of

lift generation mechanisms and follow-up control strategy construction. Secondly and relatively, the flapping wing system is widely regarded as a nonlinear system, whose control strategy is not easy to achieve. Thirdly, power supply is also a problem. Among them, the biggest challenge lies on the aerodynamic model. If we can obtain an accurate but simple model to describe the aerodynamics and fluid-structure interaction, we would be better able to construct an efficient and robust control method based on model characteristics, and thereby improve agility with low power expenditure.

Low-order modeling is an approach which tries to simulate the flow with fewer degrees of freedom but still capture important flow features. It was widely used before the availability of computing resources [123, 122, 9, 98]. Researchers characterized flow with the phenomena they were interested in and tried to find a simplified model to mimic them. In this way, people achieved many important results and established some classical ways to attack fluid problems. With fewer degrees of freedom, low-order models save the computational time and allow a faster adjustment in control system.

2.2 Low-Order Modeling

Low-order models play key roles in this work. Flow features are mainly represented by several point vortices. With different simplifications, different arguments are drawn to derive different governing equations. The models based on Brown-Michael equation and impulse matching argument are presented here.

2.2.1 Brown-Michael Model

In the study of delta wing at high Reynolds number, Brown and Michael [9] used potential flow solutions to model the unsteady free vortex separated from leading edges. In Chapter 1, we provide a general explanation on the idea of

Brown-Michael equation. Here, we use complex potential theory and give a more specific explanation on it. When point vortex approximation is made in complex potential solution, a complex log term $\frac{\Gamma}{2\pi i}\ln(z-z_o)$ is introduced to represent a point vortex at $z=z_o$ in complex potential. In the calculation of the pressure on the plate, unsteady Bernoulli equation is used and time derivative of complex potential is therefore essential. The differential of complex vortex term leads us to a expression $\frac{\Gamma}{2\pi i}\frac{1}{z-z_o}\frac{dz_o}{dt}+\frac{1}{2\pi i}\ln(z-z_o)\frac{d\Gamma}{dt}$, which is multi-value for time-dependent circulation. Then, if we draw a branch cut connecting the edge and unsteady vortex, the different pressure values are achieved across it. This discontinuity in pressure leads to the unbalanced force and moment in the flow, which are believed to influence the flow characteristics significantly [9, 53]. To remove the unbalanced force, the governing equation of vortex position with unsteady circulation is modified accordingly, from

$$\frac{dz}{dt}=\overline{\tilde{w}} \tag{2.1}$$

to

$$\frac{dz}{dt}+\frac{(z-z_o)}{\Gamma}\frac{d\Gamma}{dt}=\overline{\tilde{w}} \tag{2.2}$$

where z and Γ are the position and strength of vortex, z_o is the edge where the vortex is shed and $\tilde{w}$ is the desingularized complex velocity of the fluid at the position of the vortex. equation(2.2) is refered to as Brown-Michael equation.

Cortelezzi and Leonard [23] implemented the equation to simulate the flow around semi-infinite plate. Michelin and Llewelyn Smith [79, 80] used the same equation for falling cards and flapping flags. We start our research in a similar way.

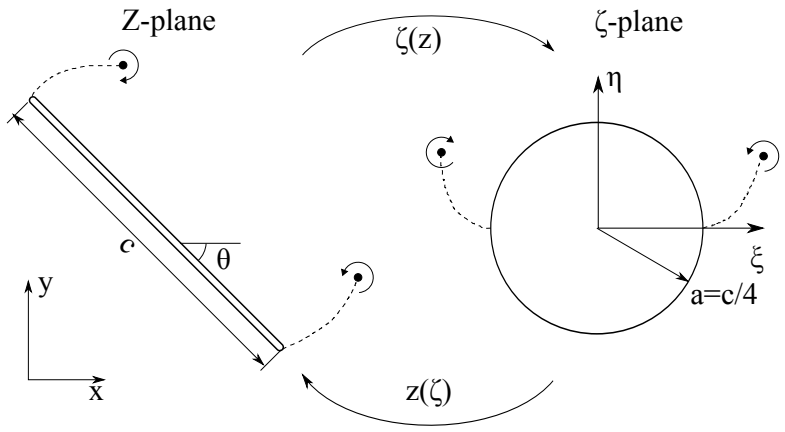

Figure 2.1: Sketch of the transform

2.2.1.1 Geometry & Plate Motion

The geometry studied here in the physical space is a thin flat plate, whose length is c. It can be mapped from the circle of radius a centered at the origin in the mapped plane through the transformation

$$z = z_c + e^{i\theta} g(\zeta) \tag{2.3}$$

where $g(\zeta) = \zeta + \frac{a^2}{\zeta}$ and radius of circle in mapped plane $a = c/4$, θ is the angle between trailing edge and x-axis, illustrated also in Fig. 2.1.

$$\dot{z}_c = -U_\infty + i\omega l e^{i\theta} \tag{2.4}$$

$$\theta = -\alpha(t) \tag{2.5}$$

$$\omega = \dot{\theta} \tag{2.6}$$

where U_∞ is the free stream velocity and is always positive, l is the distance between the axis location and center point, and $\alpha(t)$ is the angle of attack. In pitching/perching cases studied in this work, $\alpha(t)$ is defined in Chapter 2.

2.2.1.2 Complex Potential

The complex potential in mapped plane can be easily achieved:

$$F(\zeta) = -\frac{2ia^2\Im(U)}{\zeta} - \frac{i\omega a^4}{\zeta^2} + \sum_{n=1}^{N}\frac{\Gamma_n}{2\pi i}\left[\ln(\zeta-\zeta_n) - \ln(\zeta - \frac{a^2}{\bar{\zeta}_n})\right] \quad (2.7)$$

where $U = -\dot{\bar{z}}_c e^{i\theta} = U_\infty e^{i\theta} + i\omega l$. In this way the complex potential is derived in the inertial frame, which set fluid at infinity to be rest.

In order to use the Brown-Michael equation, we need to get the complex velocity in physical plane:

$$w(z(\zeta)) = \frac{\zeta^2 e^{-i\theta}}{\zeta^2 - a^2}\left[U - \frac{a^2}{\zeta^2}\bar{U} + \frac{2i\omega a^4}{\zeta^3} + \sum_{n=1}^{N}\frac{\Gamma_n}{2\pi i}\left(\frac{1}{\zeta-\zeta_n} - \frac{\bar{\zeta}_n}{\zeta\bar{\zeta}_n - a^2}\right)\right] + \dot{\bar{z}}_c \quad (2.8)$$

One thing need to be mentioned here is that we use the independent variables in mapped plane to represent the complex velocity in physical plane for the sake of computational convenience.

2.2.1.3 Kutta Conditions and Brown-Michael Equation for Implementation

Now, for the system we are dealing with now, we have four unknown variables, positions and strengths of two unsteady vortices shed form two edges. To close the system for calculation, we need four equations. Two of them are given by the Kutta condition at two edges, which are $\zeta = -a$ and $\zeta = a$ in mapped plane, as:

$$\pm\Im(U) + \omega a + \sum_{n=1}^{N}\frac{\Gamma_n}{4\pi a}\left[1 \pm 2\Re\left(\frac{a}{\zeta_n \mp a}\right)\right] = 0 \quad (2.9)$$

Another two constraints lie in the Brown-Michael equation. Here, the Brown-Michael equation is derived in physical space, equation 2.2, while arguments are chosen as ζ_n, the vortices positions in mapped plane, for convenience.

$$\left(1-\frac{a^2}{\zeta_n^2}\right)\dot{\zeta}_n+\left(\zeta_n+\frac{a^2}{\zeta_n}-\zeta_{n,0}-\frac{a^2}{\zeta_{n,0}}\right)\frac{\dot{\Gamma}_n}{\Gamma_n}=-i\omega\left(\zeta_n+\frac{a^2}{\zeta_n}\right)$$
$$+\frac{\bar{\zeta}_n^2}{\bar{\zeta}_n^2-a^2}\left[\bar{U}-\frac{a^2}{\bar{\zeta}_n^2}U-\frac{2i\omega a^4}{\bar{\zeta}_n^3}-\sum_{j\neq n}\frac{\Gamma_j}{2\pi i}\left(\frac{1}{\bar{\zeta}_n-\bar{\zeta}_j}-\frac{\zeta_j}{\zeta_j\bar{\zeta}_n-a^2}\right)\right.$$
$$\left.+\frac{\Gamma_n}{2\pi i}\left(\frac{\zeta_n}{\zeta_n\bar{\zeta}_n-a^2}+\frac{a^2}{\bar{\zeta}_n(\bar{\zeta}_n^2-a^2)}\right)\right] \tag{2.10}$$

where $j=1,...,N$ represents all vortices in flow, $n=1,2$ representing two unsteady vortices shed from two edges. The last term in square bracket in equation(2.10) is called Routh correction [16], which is an essential extra term during the velocity transform. Therefore, we obtain a system of equations for unsteady vortices.

2.2.1.4 Early Time Behavior

In order to start solving the system, initial conditions are needed. A non-arbitrary way is to use an asymptotic approximation for small time interval at beginning, which is usually 10^3 times smaller than marching time step. The idea first comes from Cortelezzi and Leonard [23, 20]. Jones [57], Michelin and Llewellyn Smith [79] followed the same idea for early time behavior in the development of vortex sheet method and unsteady point vortex method, respectively.

Defining the reduced variable η_p such that $\zeta_p=\zeta_{p,0}(1+\eta_p)$ and $\zeta_{p,0}$ is the

position of edge, we obtain for $p = 1, 2$ from equation(2.9) and equation(2.10)

$$2\Im(U\zeta_{p,0}) + \omega a^2 + \frac{\Gamma_p}{\pi}\Re(\frac{1}{\eta_p}) = 0 \tag{2.11}$$

$$\frac{2}{\zeta_{p,0}}\eta_p\dot{\eta}_p + \frac{\eta_p^2}{\zeta_{p,0}}\frac{\dot{\Gamma}_p}{\Gamma_p} = \frac{\overline{\zeta}_{p,0}}{2a^4\overline{\eta}_p}\left[-2i\Im(U\zeta_{p,0}) - i\omega a^2 - \frac{i\Gamma_p}{2\pi}\left(\frac{1}{\eta_p + \overline{\eta_p}} + \frac{1}{2\overline{\eta}_p}\right)\right] \tag{2.12}$$

while the contribution of vortices at far edge are negligible. Further, we can define a real quantity $F_p(t) = 2\Im(U\zeta_{p,0}) + 2\omega a^2 \sim F_{p0}t^\mu$, we can simplify the equations to

$$\Gamma_p = -\frac{2\pi\eta_p\overline{\eta}_p}{\eta_p + \overline{\eta}_p}F_p(t) \tag{2.13}$$

$$\eta_p\dot{\eta}_p + \frac{\eta_p^2}{2}\frac{\dot{\Gamma}_p}{\Gamma_p} = -\frac{iF_p(t)}{4a^2\overline{\eta}_p}\left(1 - \frac{\eta_p(3\overline{\eta}_p + \eta_p)}{2(\eta_p + \overline{\eta}_p)^2}\right) \tag{2.14}$$

Solving the equations equation(2.13) and equation(2.14), we obtain initially

$$\eta_p = e^{-i\frac{\pi}{4}sgn(F_{p0})}\left[\frac{|F_{p0}|}{4a^2(2\mu+1)\sqrt{2}}\right]^{1/3} t^{(\mu+1)/3} \tag{2.15}$$

$$\Gamma_p = -sgn(F_{p,0})\pi\left[\frac{F_{p0}^4}{2(2\mu+1)a^2}\right]^{1/3} t^{(4\mu+1)/3} \tag{2.16}$$

where μ indicates how fast the plate accelerates. Less μ means faster acceleration, where $\mu = 0$ means that the plate reaches its final velocity instantaneously.

2.2.1.5 Shedding of Subsequent Vortices

The subsequent shedding follows same idea as initial shedding described in previous section. The only difference is free vortices with constant circulation are included in system, therefore equations should be changed a little bit.

As before, we define η so that $\zeta_p = \zeta_{p,0}(1 + \eta)$ and from analytical integration,

we obtain

$$\eta^2 = C\tau \tag{2.17}$$

$$C = \frac{4}{7a^4\left|\frac{2a^2}{\zeta_{p,0}^3}\right|^2}\left[2\Re(U\zeta_{p,0}) + i\omega\left[\frac{4a^4}{\bar{\zeta}_{p,0}^2} - \left(\zeta_{p,0} + \frac{a^2}{\zeta_{p,0}}\right)\frac{2a^2}{\bar{\zeta}_{p,0}}\right] - \sum_{n\neq p}\frac{\Gamma_n}{\pi}\Im\left(\frac{\zeta_{p,0}\zeta_n}{(\zeta_n-\zeta_{p,0})^2}\right)\right] \tag{2.18}$$

where $\tau = t - t_s$ and t_s is the time of shedding. Then, we can solve the intensity of the subsequent vortex through the simplified Kutta equation below

$$2\Im(U\zeta_{p,0}) + \omega\frac{2a^4}{\zeta_{p,0}^2} + \frac{\Gamma_p}{\pi}\Re\left(\frac{1}{\eta}\right) + \sum_{n\neq p}\frac{\Gamma_n}{2\pi}\left[1 + 2\Re\left(\frac{\zeta_{p,0}}{\zeta_n - \zeta_{p,0}}\right)\right] = 0 \tag{2.19}$$

where $p = 1, 2$, $\zeta_{1,0} = -a$ and $\zeta_{2,0} = a$.

2.2.1.6 Force on the Plate

The force on the plate can be obtained via several ways, like the integral of pressure, and rate of impulse change. Here, we choose the linear impulse way, in which force can be written as

$$F_x + iF_y = -\rho\frac{dP}{dt}, \tag{2.20}$$

where P is the linear impulse, which can be obtained from general vector formula [33]

$$P = \int x \times \omega dA + \oint x \times \gamma_\omega ds + \oint x \times (\gamma_b + n \times u_b)ds \tag{2.21}$$

where ω is the ambient vorticity in fluid, u_b is the local surface velocity of the body, n is the outward normal vector at surface, and γ_ω and γ_b are the strengths of the vortex sheets on the surface in response to ambient vorticity and body

motion, respectively. By Kelvin's circulation theorem,

$$\int \omega dA + \oint \gamma_\omega ds + \oint (\gamma_b + n \times u_b) ds = 0, \tag{2.22}$$

To make it compatible to the equation derived in complex form, we need to transform the impulse expression into complex notation. With some manipulation, the impulse components have the form

$$P = P_x + iP_y = -e^{i\alpha} \left[i\Gamma_v z_v + \oint iz(\eta) \Re \left(\frac{\partial F}{\partial \zeta} d\zeta \right) \right] \tag{2.23}$$

Further, considering that the imaginary part of $(\partial F/\partial \zeta)d\zeta$ contributes nothing to a flat plate of infinitesimal thickness, we can use residue theory to evaluate the integrals and arrive

$$\rho P = ie^{i\alpha} \left[M_{yy} V - \frac{1}{2} \rho a \Gamma_v (\zeta_v - \zeta_v^{(i)}) \right] \tag{2.24}$$

where $\zeta_v^{(i)}$ is the image vortex of ζ_v and $M_{yy} = \rho \pi a^2$ is the sole added-mass coefficient in the body-fixed frame. The first term shows the added mass effect in response to linear accelerations and coupled rotations-translations of the plate.

2.2.2 Impulse Matching Model

In Brown-Michael equation, unbalanced force around a brunch cut connecting point vortex and edge is canceled by moving point vortex in a modified velocity other than Kirchhoff velocity. However, it is still not clear whether the unbalanced force affects the force generation exerted on the wing. Meanwhile, this equation constrains that subsequent shedding vortex should only be released at the time the previous vortex reaches its local maximum to avoid the discontinuity in force calculation. This argument is fine in mathematics but cannot capture the well-known Karman vortex street behind a inclined plate. In order to allow shedding

at any time based on other criteria, such as vortex formation number [96, 15], an impulse matching model is used, which is introduced in [112]. The basic idea is to match the fluid impulse before and after the circulation of unsteady vortex is frozen to ensure the force on the body is continuous. The governing equation similar to Brown-Michael one can be derived as follow:

Let us label the position and strength of the constant-strength vortex as z_v^{CS} (or ζ_v^{CS} in the circle plane) and Γ_v^{CS}, respectively. According to the assumption, we have

$$\frac{dz_v^{CS}}{dt} = w_{-v}^*(z_v^{CS}), \frac{d\Gamma_v^{CS}}{dt} = 0 \tag{2.25}$$

and at some instant t_0, $z_v^{CS}(t_0) = z_v(t_0)$ (and $\zeta_v^{CS}(t_0) = \zeta_v(t_0)$) and $\Gamma_v^{CS}(t_0) = \Gamma_v(t_0)$. Then, we can express the basic idea of the impulse matching model as

$$\frac{dP}{dt} = \frac{dP^{CS}}{dt} \tag{2.26}$$

By imposing the definition of impulse, equation(2.24), we get

$$\frac{d}{dt}(\zeta_v - \zeta_v^{(i)}) + \frac{(\zeta_v - \zeta_v^{(i)})}{\Gamma_v}\frac{d\Gamma_v}{dt} = \frac{d}{dt}(\zeta_v^{CS} - \zeta_v^{CS(i)}) \tag{2.27}$$

The added-mass term is canceled out in both sides, as the body motions are identical for vortex and its constant-strength counterpart. To achieve an equation similar to Brown-Michael one, we need to transform this equation into the physical domain. The results is shown to be

$$\frac{dz_v}{dt} + \frac{G(z_v - z_{10}, z_v - z_{20})}{\Gamma_v}\frac{d\Gamma_v}{dt} = w_{-v}^*(z_v) \tag{2.28}$$

where

$$G(v, w) = \frac{|v|w + |w|v}{|v| + |w|} \tag{2.29}$$

The remaining derivations of the whole system are identical with those for the Brown-Michael model. More details about the derivation can be found in Wang and Eldredge's paper [124].

CHAPTER 3

Problems & Results

3.1 Problem Statement

In this section, two simple plate maneuvers, translating and pitching, are chosen as example motion to exam the flow structures. The wing shape chosen here is a flat plate whose thick-chord ration is only 0.0023, so that it can be regarded as a thin plate in complex plane and be easily transform to a circle plane through Joukowsky transform. The kinematics is described in the following section.

3.1.1 Translation

Translation of the wing at a fixed angle of attack has been studied by various researchers from early 20th century. Here, we used the same dynamics as Pullin and Wang studied in their paper [91], which has also been studied by Chen et al. [15]. The sketch is shown in Fig. 3.1. α is the angle of attack which is fixed in this motion. The translation velocity $U(t)$ has the form:

$$U(t) = Bt^{\mu} \tag{3.1}$$

where $\mu \leq 0$ is a power exponent and B is a constant with dimensions $L \times T^{-(1+m)}$. This kinematic can be regarded as a single stroke motion to study the unsteady vortex dynamics of separation at the plate edges.

For the sake of comparison between results, we normalized equation(3.1) by

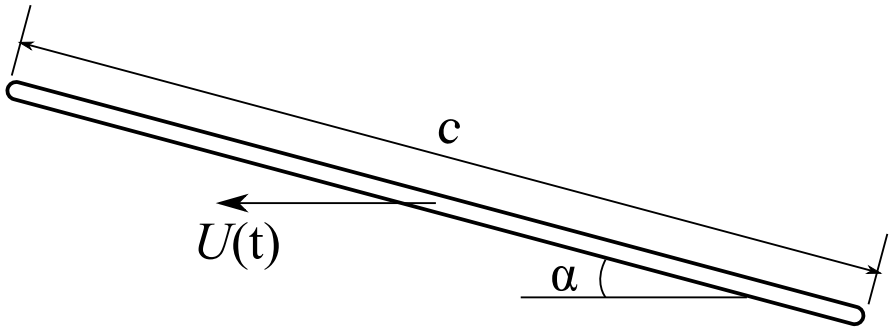

Figure 3.1: Schematic drawing of translation plate

the chord length c and velocity scale U_{ref} and $B = U_{ref}^{1+\mu}/c^{\mu}$. Then

$$U(t) = \frac{U_{ref}^{1+\mu}}{c^{\mu}} t^{\mu}, \tag{3.2}$$

$$\frac{U}{U_{ref}} = \left(\frac{tU_{ref}}{c}\right)^{\mu}, \tag{3.3}$$

or alternatively,

$$\hat{U} = \hat{t}^{\mu}. \tag{3.4}$$

In this way, all parameters have been nondimensionalized. However, Chen et al. [15] argued that $\hat{t} \equiv tU_{ref}/c$ is based on the reference velocity and therefore sensitive to the instantaneous velocity of the airfoil. They provided another nondimensional time scale $\tilde{t}$, which has the form

$$\tilde{t} = \frac{1}{c} \int_0^t U(\tau) d\tau. \tag{3.5}$$

This time scale is proved to be insensitive to instantaneous velocity, and can be related to former time scale through integral evaluation $\tilde{t} = \hat{t}^{1+\mu}/(1+\mu)$.

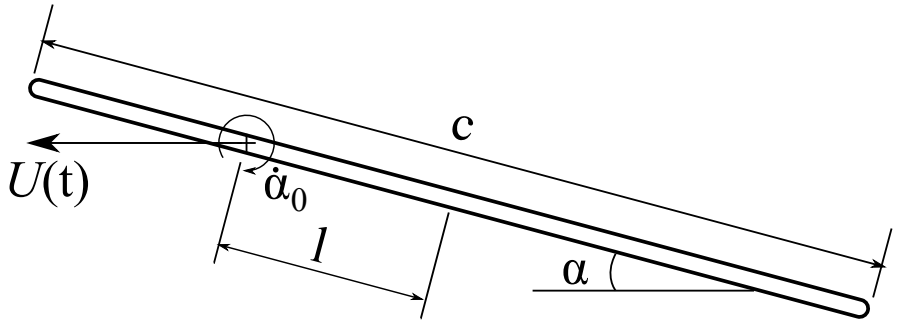

Figure 3.2: Sketch of pitching wing

3.1.2 Pitching/Perching

Pitching and perching are probably the simplest and most canonical motions which mimic the fly of small birds and insects. The simplicity of these motions allow us to investigate the unsteady aerodynamics throughly. The pitching wing is drawn schematically in Fig. 3.2. Here, the pitch-up maneuver is introduced according to the AIAA paper by Eldredge and Wang [35]. The wing's chord length is c with thick $0.023c$. The pitching axis is placed at a distance l from the center of plate, where positive l means the axis is at leading half of the plate. Pitching and perching motions are considered here, which share same angular motion but have different free stream velocity. For pitching motion, the wing translates in a constant speed, $U(t) = U_0$, while for perching, the wing starts at speed U_0, and decelerates linearly to rest at the end of the pitch-up interval. The angle of attack $\alpha(t)$ is prescribed over time in a form

$$\alpha(t) = \alpha_0 \frac{G(t)}{\max G}, \tag{3.6}$$

where α_0 is the maximum angle, which equals to $\pi/2$ in this work and G describes a complete pitch-up/pitch-down maneuver,

$$G(t) = \ln\left[\frac{\cosh(a_s U_0(t-t_1)/c)}{\cosh(a_s U_0(t-t_2)/c)}\right] - a_s U_0(t_1 - t_2)/c. \tag{3.7}$$

The parameter a_s controls the speed of the transitions between kinematic intervals, with larger value producing sharper transitions. The time t_1 and t_2 are the start time and stop time of pitch-up motion, respectively. When $t < t_1$, the wing translates at zero incidence. This period is required for high fidelity simulation for allowing the boundary layer to develop on the plate, which is usually set to be c/U_0. In inviscid model, there is no such requirement so we should be able to set t_1 to be zero. However, considering the transition from rest to pitch-up, we usually set it 0.3 to ensure the model covers the pitch from horizontal position. During time $t_1 < t < t_2$, the wing rotates at a fixed angular velocity, where t_2 is calculated as $t_2 = t_1 + \alpha_0/\dot{\alpha}_0$. Another important parameter is the reduced frequency $K = \dot{\alpha}_0 c/(2U_0)$, which is a normalized parameter from pitch rate $\dot{\alpha}_0$. As for the choice of all these parameters, they are specified in the Chapter 4 with the discussion of the results.

3.2 Translation Motion

Translating at a fixed angle of attack is probably the simplest motion for a wing. Wagner [123] first attempted a theoretical analysis on flow around such a wing and gained some interesting results. Pullin and Wang [91] used vortex sheet method to model this problem, where sheet is governed by Birkhoff-Rott equation. Here, we choose the same kinematic from Pullin and Wang's paper and compare the force between their model and our low-order ones for $\mu = 0.5, 1, 2$ at $\alpha = 30°, 60°$.

3.2.1 Force On the Plate

According to Wagner [123], the lift force on a 2D airfoil at small t and α is given as a form

$$F_{y'} = \frac{1}{2}\pi\rho c U^2(t)\sin\alpha + \frac{d}{dt}[m'_{21}U(t)] \tag{3.8}$$

where m'_{21} is the element of added mass tensor and $'$ indicates the variables in inertial frame. Added mass tensor $\mathbf{m}'$ can be arrived by added mass tensor $\mathbf{m}$ in body fixed frame and the rotation matrix $\mathbf{R}$ through easy transform $\mathbf{m}' = \mathbf{RmR^{-1}}$, where

$$\mathbf{m} = \begin{bmatrix} -\pi\rho b^2 & 0 \\ 0 & -\pi\rho a^2 \end{bmatrix}, \mathbf{R} = \begin{bmatrix} \cos\alpha & -\sin\alpha \\ \sin\alpha & \cos\alpha \end{bmatrix}. \tag{3.9}$$

The parameters a and b represent the semimajor and semiminor axis, respectively. For the problem we tackles with now, the geometry parameters are set to be $a = c/2, b = 0$ for thin flat plate.

Then, we can get a simpler expression of lift coefficient

$$\begin{aligned} C_L &= \frac{F_{y'}}{\rho U^2(t)c/2} \\ &= \pi\sin\alpha + \frac{1}{4}\pi\sin 2\alpha\frac{\mu}{(\mu+1)\tilde{t}} \end{aligned} \tag{3.10}$$

With our current notation, the lift coefficient give by Pullin and Wang can be written as

$$\begin{aligned} C_L &= \frac{4(5\mu+2)}{3}\left(\frac{3}{4(\mu+1)}\right)^{\frac{2}{3}} J_0\sin^{\frac{5}{3}}\alpha\cos\alpha\Re\left[\int_0^1 \omega_0^{1/2}(\lambda)d\lambda\right]\hat{t}^{\frac{-(\mu+1)}{3}} \\ &\quad + \frac{\pi\mu}{2}\hat{t}^{-\mu-1}\cos\alpha\sin\alpha. \end{aligned} \tag{3.11}$$

With the value 2.2 and 0.32 set to the parameter J_0 and the real part of the

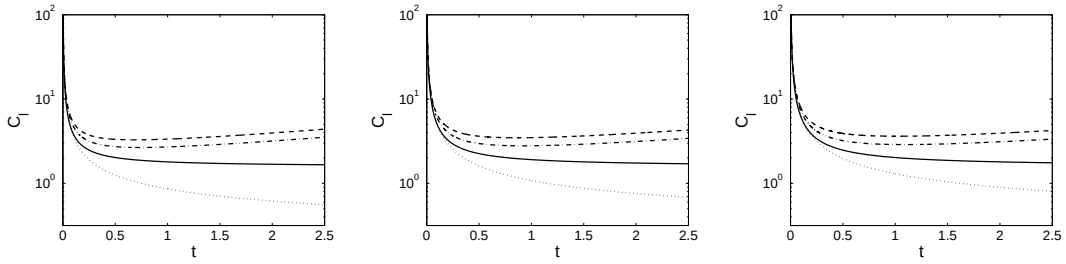

(a) $\mu = 0.5$ (b) $\mu = 1$ (c) $\mu = 2$

Figure 3.3: Comparison of lift coefficient at $\alpha = 30°$ for different μ. Brown-Michael model (- -), Impulse matching model (-··-), Wagner's (—), Pullin and Wang ($\cdots$).

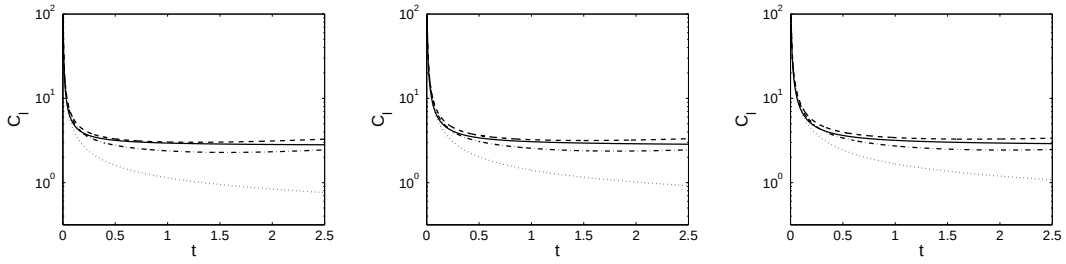

(a) $\mu = 0.5$ (b) $\mu = 1$ (c) $\mu = 2$

Figure 3.4: Comparison of lift coefficient at $\alpha = 30°$ for different μ. Brown-Michael model (- -), Impulse matching model (-··-), Wagner's (—), Pullin and Wang ($\cdots$).

complex shape function integral [91], the expression can be simplified as

$$C_L = 0.7749 \times \sin^{5/3}\alpha \cos\alpha \frac{5\mu + 2}{(\mu + 1)\tilde{t}^{1/3}} + \frac{1}{4}\pi \sin 2\alpha \frac{\mu}{(\mu + 1)\tilde{t}} \tag{3.12}$$

3.2.2 Comparison

Fig. 3.3 and Fig. 3.4 indicate the force comparison among low-order models and Wagner's prediction at different acceleration rate μ and angle of attack α. All results show the same qualitative trend. C_l decreases a lot at the very early stage, when $\tilde{t} < 0.2$; then, the coefficient tends to reach a steady value. Further, by looking at equation(3.10) and equation(3.12), we know μ affects the coefficient only when $\tilde{t}$ is very small, so the plots of different μ are almost identical to each other for the same angle of attack. From Fig. 3.3, our low-order models predict

the force larger than Wagner's theory. The higher lift can be partially explained by the contribution of leading-edge vortex included in our models which is missed in Wagner's theory. Also, impulse matching model provides a smaller force prediction than Brown-Michael one, which agrees with the argument given in Tchieu's paper [111] that the conservation of impulse criteria is able to correctly capture the initial response compared with Brown-Michael equation. As for Fig. 3.4, the values of Wagner's theory are just presented for completion, as the theory is not suitable for the plate at high angle of attack. Impulse matching model still provides a smaller force prediction than Brown-Michael one.

As for the flow condition after $\tilde{t} = 2.5$, it cannot be modeled correctly by our low-order models. Although we include mechanism of subsequent shedding to release new vortex into flow field, it is not able to well capture the sustained vortex shedding, like Karman vortex street, in this problem. We are still seeking an alternative way to introduce the newly shedding vortex into our models.

3.3 Pitching and Perching Motion

Low-order models, both Brown-Michael model and impulse matching one, are used to simulate the pitching and perching motion in free stream. Results are compared with high fidelity simulation as well as experimental results.

3.3.1 Pitching Motion

The kinematics of the pitching motion is described in Chapter 2. The pitching axis investigated here is located at leading edge. The cases with reduced frequency (or pitching rate) $K = 0.2, 0.7$ are presented.

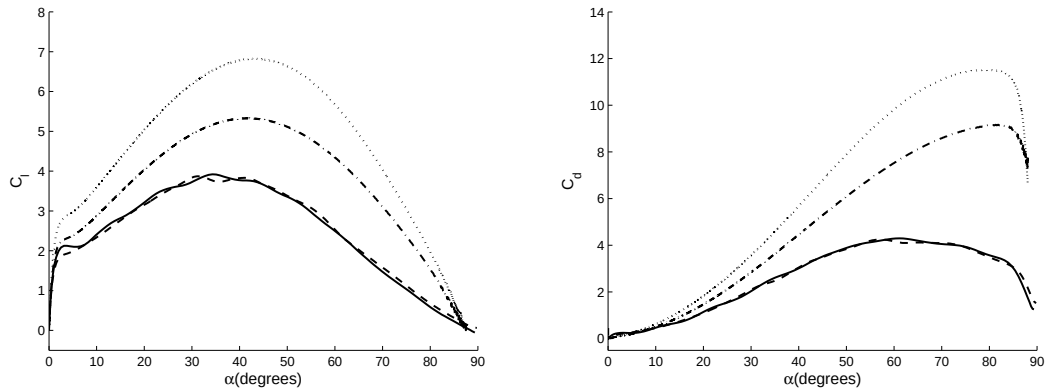

Figure 3.5: Lift (left) and drag (right) coefficients for pitching motion at $K = 0.2$. Impulse matching model (-·-); Brown-Michael model ($\cdots$); VVPM simulation (- -); Experiment (Granlund et al.[47]) (—).

3.3.1.1 Pitching rate $K = 0.2$

Fig. 3.5 shows the lift and drag comparison among experiments (carried out at Reynolds number 20000), high fidelity simulations (at Reynolds number 1000) and low-order models. The result from high fidelity simulation agrees well with the experiment, which indicates that Reynolds number does not have a big effect on the force generation. As for the low-order models (i.e. Brown-Michael model and impulse conservative model), they both predict the force trend quite well, with much fewer degrees of freedom, typically less than 10; in contract, the high fidelity simulation requires number of particles on the order of 10^5, each with three degrees of freedom. The lift from all methods exhibits a rapid initial rise due to inertial reaction, reaches a maximum at around 40 degrees and then drops steadily toward zero as the final position of plate is vertical. The drag goes up steadily with the angle of attack, as one would expect, but drops quickly at the end of the interval because of the deceleration of the pitching. As for quantity, both low-order models over-predict the force. Nevertheless, the impulse conservative model performs better than the Brown-Michael model, as the force prediction from the former one is closer to the experimental result.

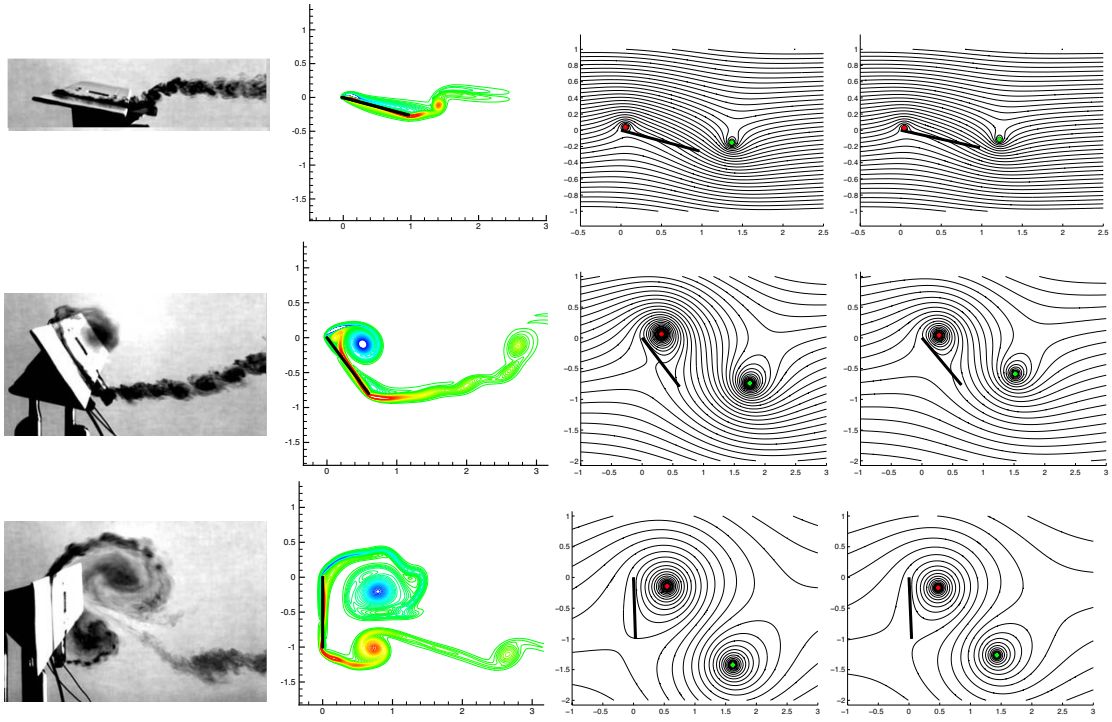

Figure 3.6: Flow field of pitching motion for $K = 0.2$ at $\alpha = 15°$, $53°$ and $90°$. First column: dye visualization from experiments (Granlund et al.[47]); second column: vorticity field of VVPM simulation; third and fourth columns: streamlines from Brown–Michael and impulse matching models, respectively, with point vortex locations denoted with colored circles.

Fig. 3.6 illustrates the flow field at $\alpha = 15°, 53°, 90°$ for the pitching motion. By looking at the left two columns, one can clearly see that the flow fields from experiment and high fidelity simulation are very similar to each other, despite of different Reynolds numbers. The little evidence of high Reynolds number in experiment can be observed from the shear instability of leading and trailing edge vortex. The flow field of two reduced models are presented at right two columns. The difference between them is too small to tell by looking at them directly, so for the simplification only the flow field from Brown-Michael model will be shown in the upcoming discussion. As for the comparison between the low-order models and high fidelity simulation, we can find something interesting. At $\alpha = 15°$, both leading and trailing edge vortex positions can be well predicted by reduced model, as at this time the flow structure in real flow are somehow like point vortex. At

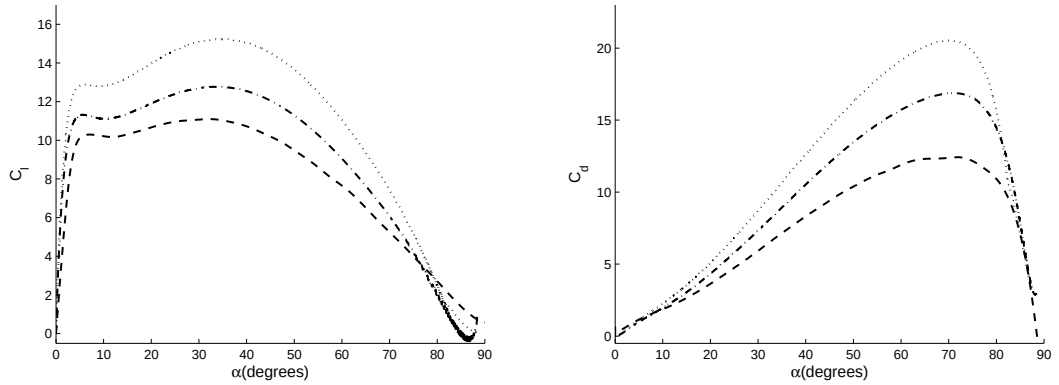

Figure 3.7: Lift (left) and drag (right) coefficients between models for pitching motion at $K = 0.7$. Impulse matching model (-·-); Brown-Michael model ($\cdots$); VVPM simulation (- -).

$\alpha = 53°$, the position of leading-edge vortex (LEV) can still be well predicted by the low-order models, as it looks like a point vortex. On the contrary, the prediction of the position of trailing edge vortex (TEV) by reduced model is not reliable anymore. It's because the vortices shed from trailing edge become a vortex sheet, which can no longer be presented by a single point vortex, in real flow. At $\alpha = 90°$, the shape of the LEV is not smooth because of some kinds of instability in high fidelity simulation, but its position can still be well predicted by the low-order models. As for the trailing edge vortex sheet, the low-order models represent those only approximately.

3.3.1.2 Pitching rate $K = 0.7$

Fig. 3.7 is the lift and drag comparison at a pitch rate of $K = 0.7$ among the low-order models and high fidelity simulation. Due to the high pitch rate, the experimental result is not available. We can obtain similar conclusion with $K = 0.2$ case. From the plots, the force prediction of the low-order models is qualitatively matched the high fidelity simulation, which can be verified by the initial inertia effect due to accelerating rotation and lift peak at around 30-40

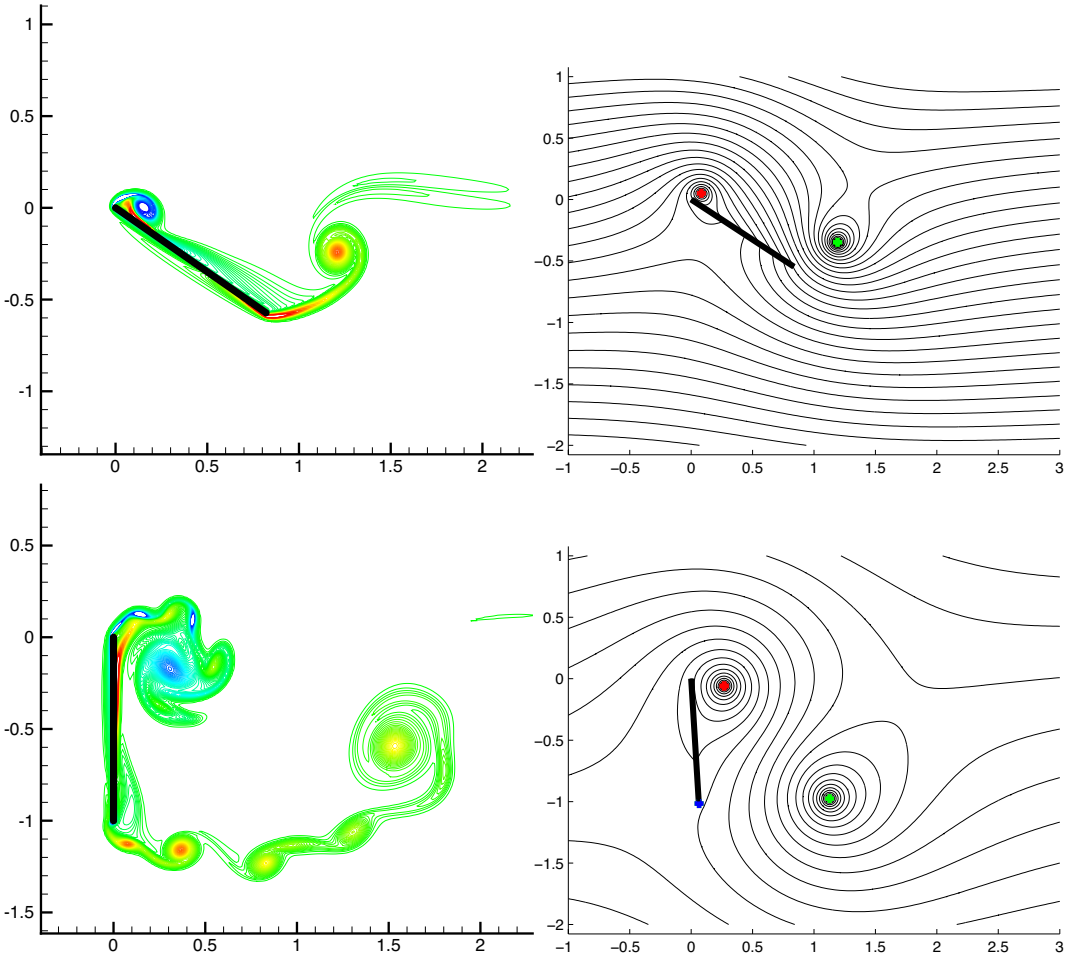

Figure 3.8: Flow field of pitching motion for $K = 0.7$ at $\alpha = 33°$ and $90°$. First column: vorticity field of VVPM simulation; second column: streamlines from Brown–Michael model, with point vortex locations denoted with colored circles.

degrees. At for the quantitative part, both low-order models give a larger force prediction, while impulse matching model does a slightly better job.

The flow field depicted in Fig. 3.8 at $\alpha = 33, 90°$. As the increase of rotation speed, the vortices generated in real flow are more coherent and keep a point-like shape for longer time, which can be better represented by a point vortex in the low-order models. A reminder is that only Brown-Michael results are shown here, as the results from impulse matching model are very similar. The shear instabilities developed near the edge of the maneuver observed in VVPM simulation cannot be captured by low-order models, but these have little influence on the force exerted

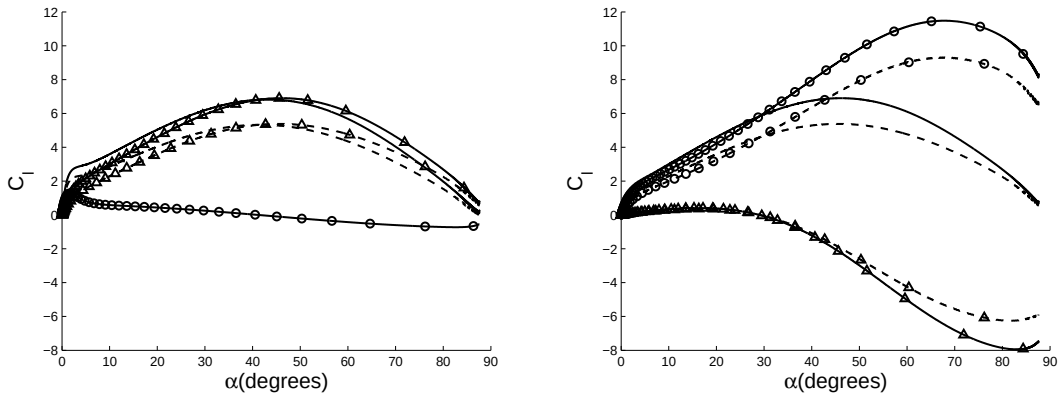

Figure 3.9: (Left) Decomposition of lift from reduced models at $K = 0.2$ pitching motion. Circulatory component ($-\triangle-$); inertial reaction component ($-\circ-$); total lift (—). (Right) Decomposition of circulatory component of lift into contributions from impulse of each vortex. leading edge vortex ($-\triangle-$); trailing-edge vortex ($-\circ-$); total circulatory component from model (—). In both panels, Brown–Michael model shown with solid lines, and impulse matching model with dashed lines.

on the plate.

3.3.1.3 Decomposition of Lift

In order to have a better understanding of the role of inertial reaction and circulatory components in the lift generation, we decompose the lift obtained from the low-order models in the left column of Fig. 3.9 and Fig. 3.10 for two rotation rates $K = 0.2$ and $K = 0.7$. The inertial reaction is represented by the first term in equation(2.24) decided only by the kinematics of plate, so it is same for both models. The initial peak of the inertial reaction is the response to the acceleration of angular velocity at that time. After that, this component decreases as the angle of attack grows. When the angle of plate is close to 90 degrees, the reaction increases again to go back to zero when the plate tends to settle down. On the other hand, the circulatory component exhibits a relatively simple dependence on the angle of attack, nearly symmetric about 45 degrees. Compared with inertial reaction, the circulatory part plays a more important role

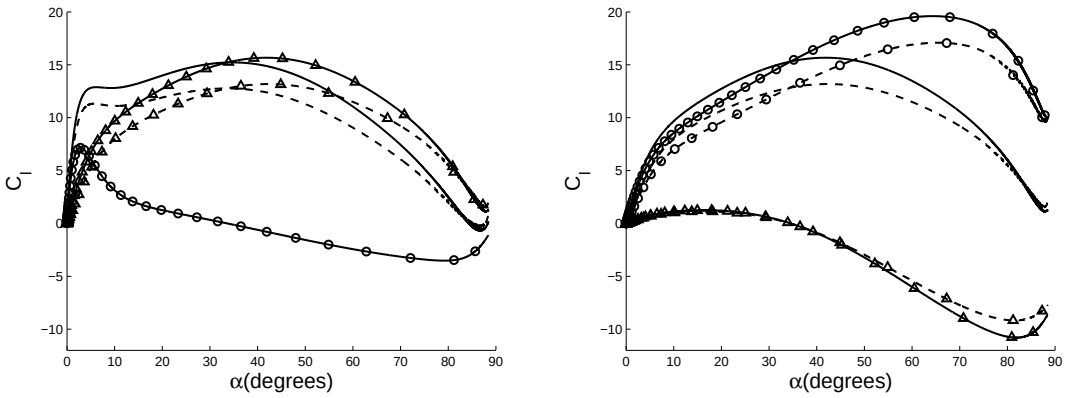

Figure 3.10: (Left) Decomposition of lift from reduced models at $K = 0.7$ pitching motion. Circulatory component ($-\triangle-$); inertial reaction component ($-\circ-$); total lift (—). (Right) Decomposition of circulatory component of lift into contributions from impulse of each vortex. leading edge vortex ($-\triangle-$); trailing-edge vortex ($-\circ-$); total circulatory component from model (—). In both panels, Brown–Michael model shown with solid lines, and impulse matching model with dashed lines.

in the lift generation, one can clearly see the potion of circulatory force is higher than the inertial one.

To demonstrate the circulatory component of lift in a more clear way, we refer to the right panels of Fig. 3.9 and Fig. 3.10, which show the contributions of the separate vortices at rotation rate $K = 0.2$ and $K = 0.7$ as well as the total contribution. From the plots, one can find that the trailing edge vortex contributes more to the lift than the leading edge one, which gives an explanation why traditional unsteady aerodynamics can still do a fairly good job even neglecting the leading edge vortex. At small angle of attack, the contribution of leading edge vortex is almost same for two different low-order models and quite small compared with the trailing edge one. At large angle of attack (i.e. larger than 45 degrees), small discrepancy occurs between two low-order models and leading edge vortex leads to a negative effect on the lift generation. This behavior can be understood by noting that the leading edge vortex has an important indirect effect on the impulse through its influence on the motion of the trailing edge vortex.

3.3.2 Perching Motion

As described in the problem statement, the only difference between pitching and perching is the free-stream velocity, which is inspired by the landing of birds. Here, we investigated the cases with linear velocity decrease, which goes to zero when the pitching angle reaches 90°. In order to avoid the zero divider in defining the force coefficient, we normalize the force by the initial free stream velocity rather than the instant one(i.e. $C_F = 2F/(\rho_f U_0^2)$).

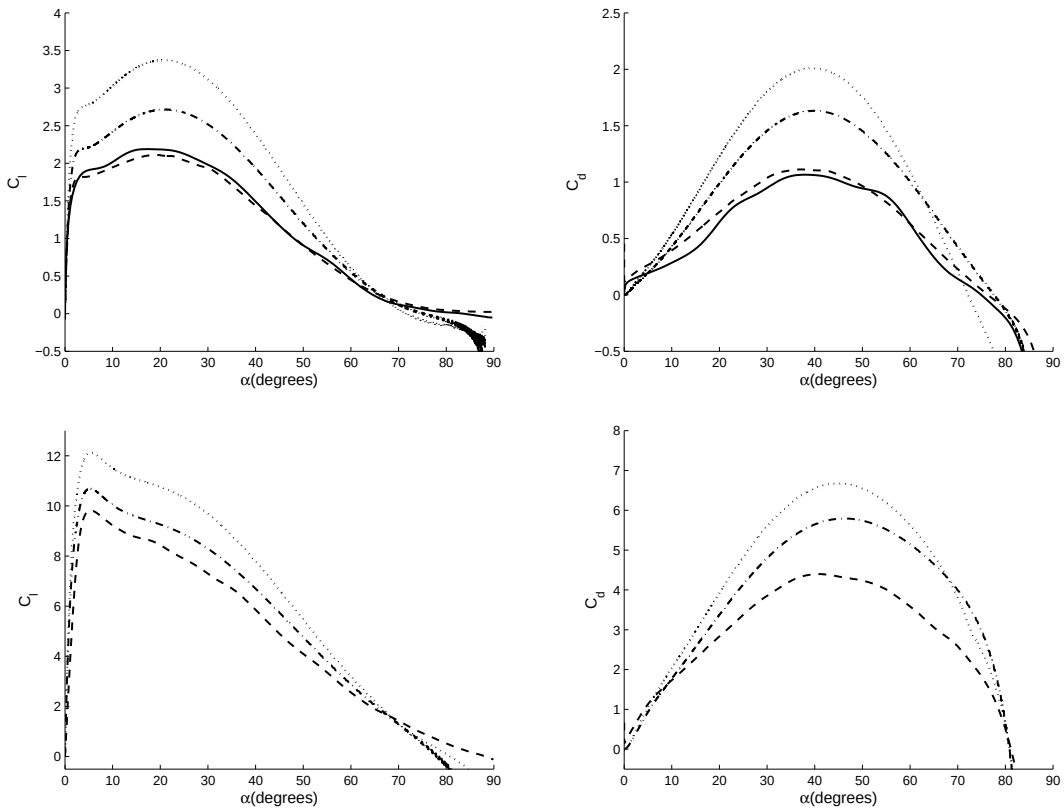

Figure 3.11: Lift (left) and drag (right) coefficients for perching motion at $K = 0.2$ (top) and $K = 0.7$ (bottom). Impulse matching model (-·-); Brown-Michael model ($\cdots$); VVPM simulation (- -); Experiment (Granlund et al.[47]) (—).

The force comparison are depicted in Fig. 3.11 among experiment and simulations at $K = 0.2$ and $K = 0.7$. Just like the results obtained from the pitching cases, the high fidelity simulation agrees well with experiments for $K = 0.2$ case.

As for the low order models, the force trend is well captured, including the peak and long subsequent decay of lift, and the gradual increase and decrease of drag. Both models over-predict the forces, but significantly less so than in the pitching case.

Fig. 3.12 is the flow field at $\alpha = 15°, 53°, 90°$. With the decreasing free-stream velocity, the size of leading edge vortex is smaller than that in the pitching case and no shear instability is triggered, compared with the pitching case in Fig. 3.6. As the attack angle reaching 90°, a vortex with negative strength is shed from the trailing edge, which is resulted from the flow induced by leading edge vortex and small free-stream velocity at that time and not be observed in the pitching cases. What is encouraging is that our low order models successfully capture this negative vortex. The flow field of $K = 0.7$ case is shown in Fig. 3.13.

Fig. 3.14 and Fig. 3.15 show the lift decomposition for rotation rates $K = 0.2$ and $K = 0.7$ for completeness. Compared with the pitching motion, the behavior of inertial reaction and circulatory components are slightly different in the late stage of the maneuver, due to the deceleration of the plate. Other than that, conclusions achieved here are very similar to the pitching cases.

3.4 Summary

In this part of the work, the low-order models have been shown to predict forces trend on translation and pitching/perching motion of the flat plate well with corresponding experiments and high-fidelity simulations, especially at the early time when there is no complex flow structures. Considering that the degrees of freedom are fewer than 10 in low-order models, the agreement is particularly notable, as $10^5 - 10^6$ is a typical range of degrees of freedom in a well-resolved high fidelity simulation. However, there are still some aspects need further attentions.

As we conclude, the low-order models are able to capture the force trend at

early time. With the developing of the flow, more and more flow structures, like vortex detachment, Karman vortex street, appear in the flow. Due to the absence of detail vortex description, it is a big challenge to fully simulate the physical phenomena with low-order models. Our focus will be set onto how to get correct force estimation and important physical phenomena like periodic vortex shedding. Understanding these will allow us to explore almost any motion of the flapping plate.

In two dimensional study, we also want to find and develop some easy control strategies to maintain a good aerodynamic performance, like a stable and high lift on the flat plate. The difficulty of this work lies on the nonlinearity of the low-order models. The construction of nonlinear control strategy is not easy and still a hot field for researchers in system and control direction.

In three dimensions, the phenomena absent in 2D flow need to be revealed and investigated. Of particular importance is the axial flow driven down the wing span. Axial flow has long been believed to be the main mechanism to stabilize the leading edge vortex and prevent the detachment, as it removes momentum from the separation vortex core to restrain its growth [78, 36, 120, 130]. One way to capture this flow feature is the high fidelity simulation. By extending the current viscous vortex particle method to three dimensions, we may be able to develop an efficient and reliable computational tool for moving objects in flow. The is one of our research direction.

As for the low-order modeling, it is hard to extend our current models to three dimensions, which are based on the simple complex potential and Joukowsky transform approach. However, there are many different types of simplified models in three dimensions, among which the simplest is probably the lifting line method, also known as Prandtl's theory. In this method, the finite span wing is represented by a lifting line, meanwhile the trailing edge vortex is assumed at far wake and has no direct influence on the force exerted to the wing. We wish to start from

this classical and simple method and develop a low-order model which allows the effect of leading and trailing edge vortex, as well as tip vortices, but still keeps a small number of degrees of freedom.

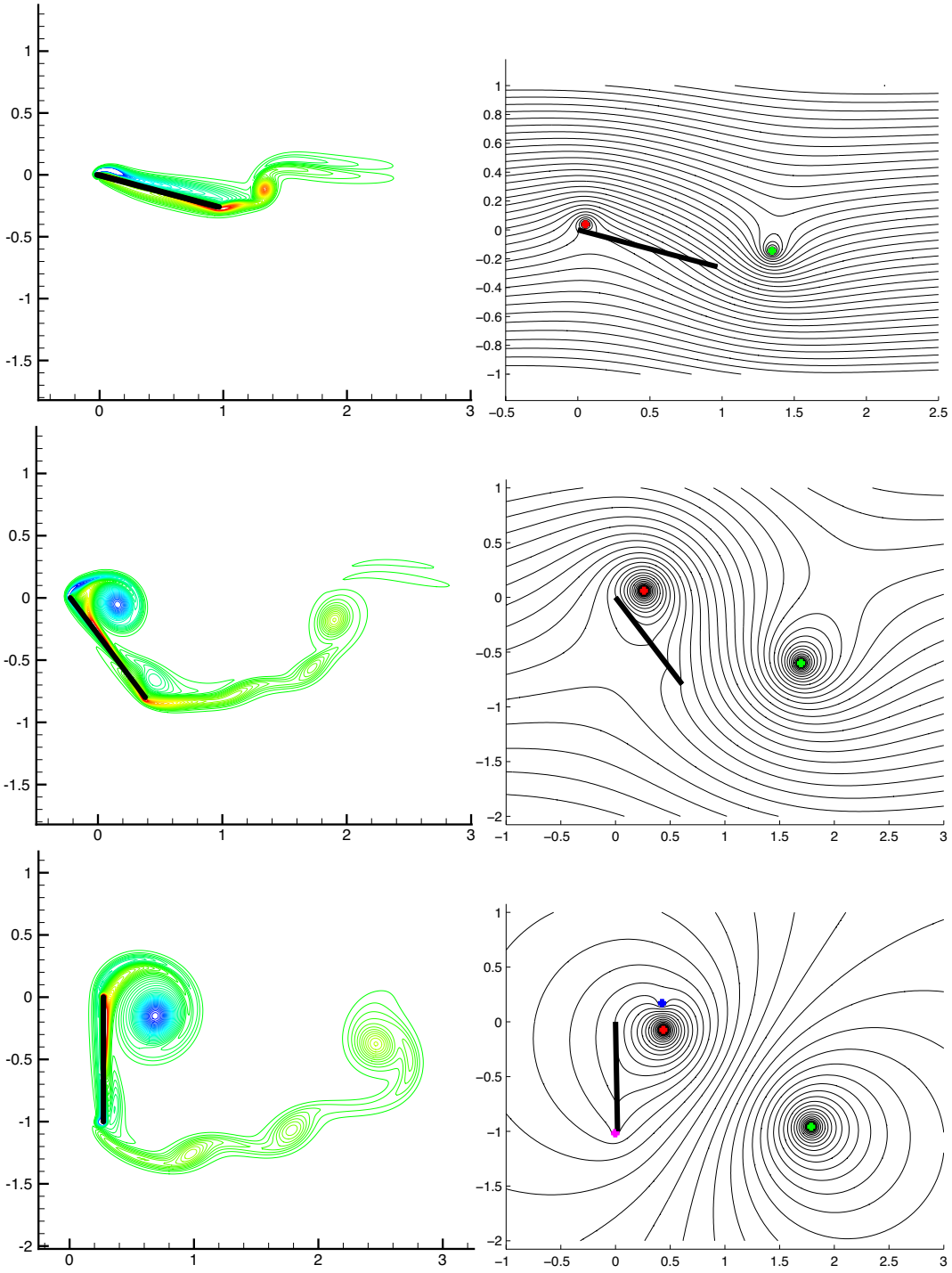

Figure 3.12: Flow field of perching motion for $K = 0.2$ at $\alpha = 15°$, $53°$ and $90°$. First column: vorticity field of VVPM simulation; second column: streamlines from Brown-Michael model, with point vortex locations denoted with colored circles.

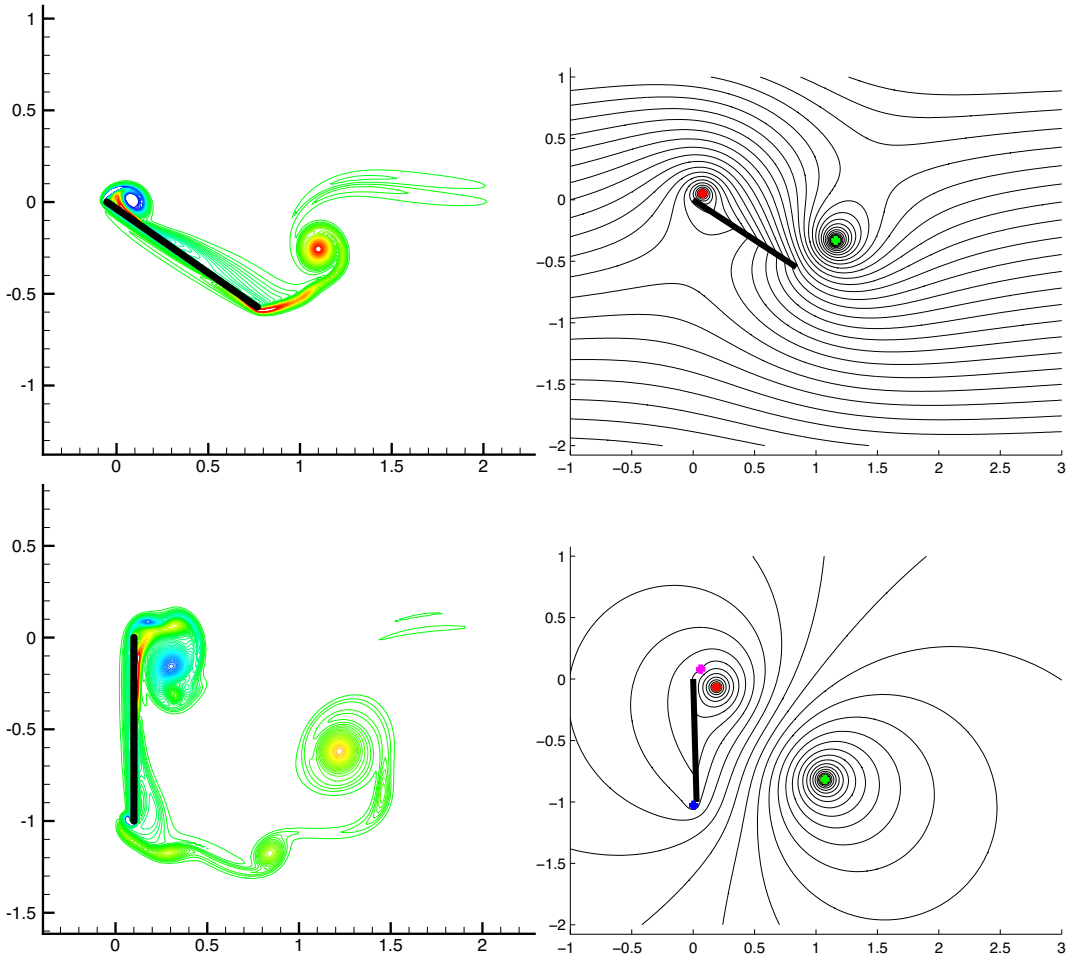

Figure 3.13: Flow field of perching motion for $K = 0.7$ at $\alpha = 33°$ and $90°$. First column: vorticity field of VVPM simulation; second column: streamlines from Brown–Michael model, with point vortex locations denoted with colored circles.

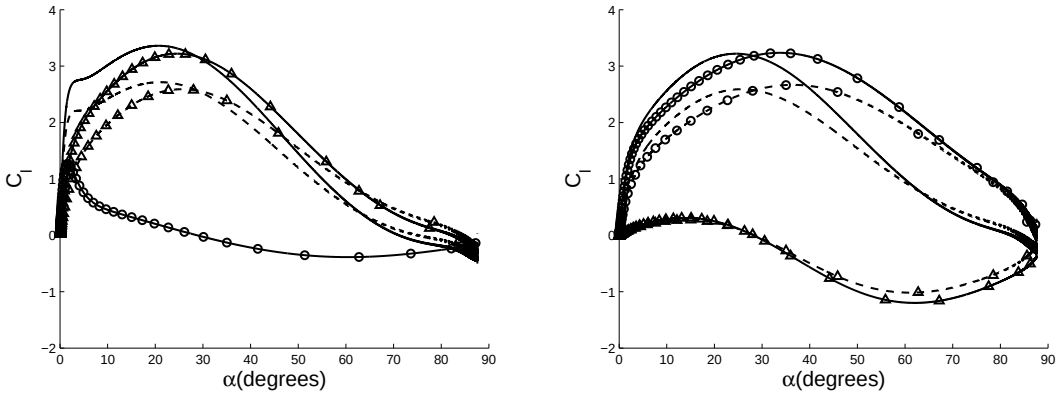

Figure 3.14: (Left) Decomposition of lift from reduced models at $K = 0.2$ perching motion. Circulatory component ($-\triangle-$); inertial reaction component ($-\circ-$); total lift (—). (Right) Decomposition of circulatory component of lift into contributions from impulse of each vortex. leading edge vortex ($-\triangle-$); trailing-edge vortex ($-\circ-$); total circulatory component from model (—). In both panels, Brown–Michael model shown with solid lines, and impulse matching model with dashed lines.

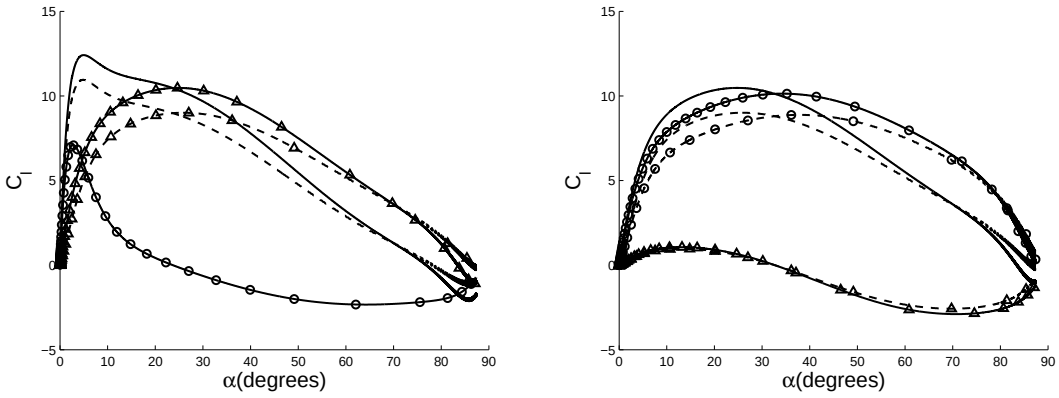

Figure 3.15: (Left) Decomposition of lift from reduced models at $K = 0.7$ perching motion. Circulatory component ($-\triangle-$); inertial reaction component ($-\circ-$); total lift (—). (Right) Decomposition of circulatory component of lift into contributions from impulse of each vortex. leading edge vortex ($-\triangle-$); trailing-edge vortex ($-\circ-$); total circulatory component from model (—). In both panels, Brown–Michael model shown with solid lines, and impulse matching model with dashed lines.

CHAPTER 4

High-Fidelity Simulation

4.1 Introduction

Fluid-structure interaction (FSI) problems arise frequently in many scientific and engineering disciplines. These problems can be broadly defined as those in which a fluid interacts dynamically with a solid structure, in contrast to interactions in which the structure's kinematics are prescribed. In this work, we are primarily interested in FSI problems in which objects or structures undergo large scale motion or deformation in response to fluid forcing at moderate Reynolds numbers. Examples of such interactions arise in a variety of contexts: in biological locomotion, particularly exemplified by swimming of aquatic organisms or flight with flexible wings; in biomedical flows, such as those in the cardiovascular or pulmonary systems; and in transport of passive (or active) particles, as in suspensions or sedimentary flows. A general feature of such interactions is that the governing equations of the fluid and the structure are coupled in a highly non-linear manner. In this paper, we focus on structures composed of one or more rigid bodies, possibly linked into extended structures, that interact with incompressible flows. Though this narrower focus restricts the class of FSI problems amenable to the methodology outlined in this paper, a rich set of problems remains nonetheless.

Numerical simulations are widely employed to investigate such FSI problems. General discussions of computational FSI are provided in some recent reviews,

e.g. [52, 25]. The general task of a FSI methodology is to ensure that the kinematic and dynamic properties match at the interface between the fluid and the structure. When the constituent fluid and structure solvers are based on conforming mesh methods, in which the computational mesh of each material is aligned with the interface, then these properties are generally matched explicitly. Arbitrary Lagrangian Eulerian (ALE) methods are typically used to locally update the fluid mesh in response to advances in the structure configuration. (See, for example, the ALE-based coupling procedure developed by Farhat et al. [37] for treating aero-elasticity problems).

Alternatively, one could view the task at the interface in the sense of variational mechanics, that FSI requires enforcement of the kinematic constraint (no-slip, no-penetration) at the interface, and that the associated interfacial force is the Lagrange multiplier that enforces this constraint. This latter perspective is particularly attractive as it unifies the interpretation of interfacial constraints with that of other constraints in the problem: the volume-preserving constraint in the incompressible fluid, for which the pressure acts as the Lagrange multiplier; and linkage constraints in the rigid-body systems, in which constraint forces serve the role of Lagrange multipliers. (Strictly speaking, one could also enforce the rigidity of the bodies themselves with Lagrange multipliers, but such a constraint is more naturally enforced directly by solving the rigid-body equations of motion.) This perspective is valuable when the interface conditions cannot easily be enforced directly, as when the fluid equations are solved with non-conforming mesh methods (sometimes referred to as immersed boundary, Cartesian grid or embedded boundary methods) [85]. For example, this is the underlying principle of the fictitious domain method developed by Glowinski and co-workers [46, 45], in which Lagrange multipliers are distributed throughout the body interiors within a finite element formulation on a fixed mesh, thereby forcing the (fictitious) fluid in these interiors to move as rigid bodies.

The present work adopts the same perspective, but with notable differences in implementation compared with the fictitious domain methods. The framework presented here is based on the immersed boundary projection method, developed by Colonius and Taira [110, 18] for flows around bodies with prescribed kinematics. In their finite volume (or staggered finite difference) method—inspired in part by the original immersed boundary method of Peskin [87, 88]—Lagrange multipliers are distributed only on the fluid-structure interface and interpolated to a uniform Cartesian grid with discrete delta functions. The discrete system of equations takes the form of a saddle-point problem [7], in which the off-diagonal blocks are associated with the interface and incompressibility constraints. Here, we replace the prescribed body motions with the dynamical equations for the rigid-body system. The role of the Lagrange multipliers on the interface is unchanged, but now their effect is accounted for in both the fluid and the structure equations. The system of equations is now differential-algebraic, with the general symmetric form

$$\begin{bmatrix} A & 0 & -D^T & -\mathsf{E}^T & 0 \\ 0 & -\Delta t\mathbb{H}' & 0 & \Delta t\mathcal{B} & \Delta tK^T \\ D & 0 & 0 & 0 & 0 \\ \mathsf{E} & -\Delta t\mathcal{B}^T & 0 & 0 & 0 \\ 0 & \Delta tK & 0 & 0 & 0 \end{bmatrix} \begin{bmatrix} u^{n+1} \\ \ddot{\mathbb{q}}^{n+1} \\ p \\ \mathsf{f_b} \\ \lambda \end{bmatrix} = R^n. \tag{4.1}$$

where u^{n+1} and $\ddot{\mathbb{q}}^{n+1}$ represent, respectively, the fluid velocity field and 6-degree-of-freedom body accelerations at the end of the time step of size Δt, p is the fluid pressure, $\mathsf{f_b}$ are the Lagrange multipliers distributed discretely on the interface, and λ are the Lagrange multipliers that enforce rigid-body linkage constraints. Detailed definitions of these quantities and the associated operators are postponed to later in the paper, though it is noted here that $\mathbb{H}'$ represents the difference between the intrinsic inertia of the bodies and that of displaced fluid. Note that the fluid equations have been discretized in time, while the rigid-body equations

remain in continuous form.

The equations (4.1) are still of a saddle-point form, and, in principle, one could use any of several techniques—such as block Gauss elimination—to solve for u^{n+1} and $\ddot{\mathfrak{q}}^{n+1}$ (and then numerically integrate to advance the body configuration). However, in order to provide more freedom and avoid the poor conditioning of heterogeneous matrix blocks, the system is partitioned into separate fluid and structure blocks, each of which is solved by a null-space projection approach [18, 38] to enforce the respective constraints of incompressibility and rigid-body linkages; in the fluid, this is equivalent to a vorticity-based treatment [18]. It is worth mentioning that the derivations of each null-space method do not necessarily start from the equations (4.1). Instead, both of them are based on the continuous forms of the fluid and rigid-body equations and can be found later in the paper.

The coupling of the two solvers is of particular importance in the algorithm design, and partitioned numerical methods for FSI can be classified into two categories in this respect: weakly coupled and strongly coupled. In a weakly coupled algorithm, the kinematic and dynamic conditions are not enforced simultaneously. Rather, the solvers are advanced sequentially, wherein one solver—usually the structure solver—provides the other with kinematic conditions at the interface, and this solver is advanced in turn to compute interfacial tractions. This approach provides the advantages of simplicity—particularly in cases in which the partitioned solvers have been developed separately—and fixed computational load, since no iteration is pursued. However, the stability of these methods is not guaranteed and is often difficult to achieve for incompressible flows with highly flexible structures [14, 43]. Therefore, weakly-coupled algorithms are widely employed in aero-elasticity problems, in which structural deformations are modest, but has also been used with some success in biomedical applications (e.g. [75]).

In a strongly-coupled partitioned scheme, as we pursue here, the kinematic

and dynamic conditions are enforced simultaneously at the fluid–structure interface. The stability of this kind of scheme is greatly improved compared with a weak one, especially with structures undergoing large deformation. As a trade-off, the computational load becomes higher as iterations are generally required in every time step. A variety of iterative techniques have been introduced and employed in different types of fluid–structure systems [25]. Among these is the block Newton–Raphson approach, which generally converges rapidly but requires the computationally-expensive calculation of the Jacobian [77, 76, 26]. Alternatively, one may use a block Gauss–Seidel method (also known as fixed-point iteration), in which each solver is provided with the updated data from the other in every iteration, and the system is iterated to convergence within some tolerance. In its naive form, this method often converges slowly, particularly when the densities of the fluid and structure are quite disparate. However, this convergence can be improved with some degree of relaxation, as in [66] and the recent immersed-boundary FSI of Tian et al. [113], or by including some information about the virtual inertia (i.e. added mass) of the fluid in the structural solver [14, 32].

We propose here a block Gauss-Seidel method that makes use of both of these improvements. The resultant fluid force on each body is relaxed first before it is used by the structure solver; convergence is determined from the difference of this force from one iteration to the next. In a stability analysis of the coupled equations, it is shown that any change of motion resulting from the iterate of force applied on the body is countered by inertial reaction from the fluid. A simple expression for the relaxation parameter is derived to optimize convergence based on an estimate of this virtual fluid inertia.

4.2 Methodology

In this section, we will first review the numerical methods targeting the fluid and rigid-body dynamics. Then, the strong coupling algorithm will be described and discussed. Our focus is to address the relationship between the fluid solver, the rigid body solver and the enforcement of the interface condition.

4.2.1 Fluid solver

The incompressible flow solver is based on the null-space form of the immersed boundary projection method introduced by Colonius & Taira [18]. Here, we summarize the details of this method to the extent necessary for introducing our coupling scheme.

4.2.1.1 Governing equations

This method makes use of the mimetic discrete operators that naturally arise on a staggered grid discretization of the computational domain $\mathscr{D}$. In particular, the discrete curl $C : \mathscr{D} \mapsto \mathscr{D}$ is defined from the null space of the discrete divergence operator $D : \mathscr{D} \mapsto \mathscr{D}$, so that $DC \equiv 0$ in analogy with the continuous identity $\nabla \cdot \nabla \times \equiv 0$. The discrete gradient is simply the negative transpose of divergence, $-D^T$, so that the analog of $\nabla \times \nabla \equiv 0$—that is, $C^T D^T \equiv 0$—automatically follows; the operator C^T is generally called the discrete rot operator. Using these operators, a discretely volume-preserving velocity field u can be obtained from a discrete streamfunction, s, by $u = Cs$, and a discrete vorticity (or, more precisely, circulation) is defined by $\gamma = C^T u$. One can always add a potential flow to the velocity obtained from the streamfunction, usually a uniform free stream U_∞.

In the presence of one or more moving bodies, additional operators are needed to interpolate data from the fluid domain $\mathscr{D}$ to the fluid–body interface $\partial\mathscr{B}$—

represented by M discrete points $\mathsf{x_b}$ immersed in the fluid grid, with associated rigid-body velocity $\mathsf{u_b}$—and to regularize the interface data onto the grid. These tasks are achieved by the interpolation operator $\mathsf{E} : \mathscr{D} \mapsto \partial\mathscr{B}$ and its transpose, the regularization operator, $\mathsf{E}^T : \partial\mathscr{B} \mapsto \mathscr{D}$, respectively. These operators are formed from the discrete Delta function [110]. Colonius & Taira enforce the no-slip constraint, $\mathsf{E}u = \mathsf{u_b}$, at interface points through a Lagrange multiplier force $\mathsf{f_b} \in \partial\mathscr{B}$, regularized to the grid in the momentum equations.

Following the derivation in [18] on a staggered Cartesian grid of uniform spacing, the semi-discrete form of the Navier–Stokes equations can be expressed, after application of the rot operator, as

$$\frac{\mathrm{d}\gamma}{\mathrm{d}t} = \frac{1}{Re} L\gamma + C^T\mathcal{N}(\gamma, u) + C^T\mathsf{E}^T\mathsf{f_b}, \tag{4.2}$$

$$u = Cs + U_\infty, \tag{4.3}$$

$$Ls = -\gamma, \tag{4.4}$$

$$\mathsf{E}C(-L^{-1})\gamma = \mathsf{u_b} - \mathsf{U}_\infty, \tag{4.5}$$

where Re is the Reynolds number, $\mathcal{N}(\gamma, u)$ denotes the non-linear convective and stretching terms, and $L = -C^TC$ is the discrete Laplacian. Also, note that in (4.5), the free stream velocity has been evaluated directly at the interface points (denoted as U_∞) and subtracted from the body velocity, rather than interpolated from the grid.

Applying a time marching scheme with the projection (fractional-step) algo-

rithm suggested in [18], the fully discretized system has the form

$$A\gamma^* = r^n(\gamma^n, u^n) \tag{4.6}$$

$$\mathsf{E}C(-L^{-1})A^{-1}C^T\mathsf{E}^T f_b = \mathsf{u_b} - \mathsf{U}_\infty - \mathsf{E}C(-L^{-1})\gamma^* \tag{4.7}$$

$$\gamma^{n+1} = \gamma^* + A^{-1}C^T\mathsf{E}^T f_b \tag{4.8}$$

$$u^{n+1} = C(-L^{-1})\gamma^{n+1} + U_\infty. \tag{4.9}$$

The matrix A is defined as $\Delta t^{-1}I - \frac{1}{2}Re^{-1}L$, where I is the identity and the trapezoidal method has been used for the viscous terms. The second-order Adams-Bashforth scheme is applied to the convective terms. The right-hand side vector is therefore $r^n = (\Delta t^{-1}I + \frac{1}{2}Re^{-1}L)\gamma^n + \frac{3}{2}\mathcal{N}(\gamma^n, u^n) - \frac{1}{2}\mathcal{N}(\gamma^{n-1}, u^{n-1})$. It is important to mention that A is a sparse symmetric positive-definite matrix whose size is determined by the computational domain $\mathscr{D}$.

The first substep (4.6) of the projection method provides an intermediate vorticity field by advancing the flow convective and diffusive processes in the absence of any body; this substep inevitably leads to a violation of the no-slip condition. Therefore, the second substep, equation (4.7), is meant to find the Lagrange boundary forces $\mathsf{f_b}$ that correct the spurious slip velocity at the interface. The left-hand-side operator $\mathsf{E}C(-L^{-1})A^{-1}C^T\mathsf{E}^T$ is a dense symmetric and positive-definite matrix, with size corresponding to the number of Lagrange forcing points on the interface $\partial\mathscr{B}$ (multiplied by the spatial dimension of the problem). In the third substep, equation (4.8), the vorticity field at t^{n+1} is calculated by amending the intermediate field with the correction produced by the Lagrange forces. The final velocity field is obtained from the curl of the streamfunction solution of the discrete Poisson equation (4.9). It is noted in passing that this projection procedure is effectively an implementation of the so-called Lighthill vorticity creation mechanism [70], also utilized in several forms of the viscous vortex particle method, for example, [64, 31].

To accelerate the computation and save memory, a multi-domain approach for far-field boundary conditions is also employed. The details of this technique can be found in [18]. The basic idea is to use a hierarchy of nested domains with different sizes and grid resolutions to cover the area of interest. In this manner, Dirichlet boundary values of one domain can be interpolated from the interior values of a larger enclosing domain of coarser grid resolution. In the largest domain, it is assumed that the boundary is far from the region of interest, and thus homogenous boundary conditions are appropriate.

4.2.1.2 Lagrange-to-body forces and motions

The fluid forces and moments on rigid bodies are of particular importance to the present coupling algorithm, and here we discuss their calculation from the Lagrange forces. First, it is useful to introduce notation that will serve the discussion here as well as for the rigid-body equations of motion below. Let us denote by $\mathscr{B}$ the space of 6-dimensional motion or force vectors associated with a single rigid body; motion vectors contain both translational and rotational components, and force vectors contain both force and moment. (Technically, motion and force vectors are in separate dual spaces, but we describe these as a single space for the sake of simpler notation.)

Define $\mathbb{f} \in \mathscr{B}$ as the generalized vector of force and moment applied by the fluid on the body, with the moment taken about the body's center of volume. Also, let $\mathbb{q}$ denote the 6-dimensional generalized coordinates of the rigid body, comprised of the three coordinates of its center of volume and three angles about some inertial axes that pass through the center. The 6-dimensional velocity and acceleration vectors of the body are denoted by $\dot{\mathbb{q}}, \ddot{\mathbb{q}} \in \mathscr{B}$. The use of such 6-dimensional vectors—called Plücker coordinates—reduces the number of operations compared to separate treatment of linear and angular motion [38]. They are interpreted as column vectors in all matrix-vector operations.

The distributed interface points, $\mathsf{x_b}$, are rigidly attached to their respective rigid body. Since these points are most usefully described in the inertial coordinate system attached to the fluid domain, then it is important to have a transformation that maps their coordinates from a reference system attached to the body to this inertial system. For a single rigid body, this can be succinctly written as

$$\mathsf{x_b} = \mathcal{X}(\mathbb{q}_t) + \mathcal{R}(\mathbb{q}_r)\mathsf{x_b^0}, \tag{4.10}$$

where $\mathbb{q}$ has been split into its three position coordinates $\mathbb{q}_t$ and angles $\mathbb{q}_r$, $\mathcal{X}$ is a length-$3M$ column vector consisting of $\mathbb{q}_t$ in each of the M block entries, and $\mathcal{R}$ denotes a $3M \times 3M$ block-diagonal matrix in which each 3×3 block consists of an operator that rotates the axes of the body-attached system parallel to the inertial axes according to $\mathbb{q}_t$. The time-invariant coordinates in this body reference frame have been denoted by $\mathsf{x_b^0}$. The time derivative of (4.10) results in a rigid-body distribution operator, $\mathcal{B} : \mathscr{B} \mapsto \partial\mathscr{B}$, which maps a motion vector of the body, such as velocity, to the distributed interface points, i.e.,

$$\mathsf{u_b} = \mathcal{B}\dot{\mathbb{q}}. \tag{4.11}$$

Its transpose, called the resultant operator, $\mathcal{B}^T : \partial\mathscr{B} \mapsto \mathscr{B}$, collects the distributed forces on the interface to compute the force and moment on the body. It is clear that $\mathcal{B}$ depends on the positions of Lagrange points $\mathsf{x_b}$ relative to the body's center of volume, or equivalently, on the body orientation $\mathbb{q}_r$ and the reference coordinates $\mathsf{x_b^0}$; its detailed form for an example can be found in the following part.

In the immersed boundary projection method, bodies are entirely immersed in the fluid grid, and discrete Lagrange forces at interface points are regularized to the grid on both sides of the interface without preference. This treatment gives rise to motion in fictitious fluid regions in the interiors of bodies. Furthermore,

it implies that the Lagrange forces $\mathsf{f_b}$ are discrete approximations to the traction applied to the fluid on either side of the interface. Thus, the resultant $\mathcal{B}^T\mathsf{f_b}$ of these Lagrange forces represents the negative of the total force and moment exerted on the interface by the real and fictitious fluids. The contribution of the real fluid to this total force is simply $\mathbb{f}$. Furthermore, from an overall conservation of momentum in the interior fluid, this fictitious portion's contribution to the total is $-\mathbb{M}_f\ddot{\mathbb{q}}$, where $\mathbb{M}_f$ is the mass of the fluid displaced by the body and $\ddot{\mathbb{q}}$ is the generalized acceleration of the body's center of volume relative to inertial axes. Thus, the generalized force applied by the fluid on the body can be written in terms of the Lagrange forces as

$$\mathbb{f} = -\mathcal{B}^T\mathsf{f_b} + \mathbb{M}_f\ddot{\mathbb{q}}. \tag{4.12}$$

Remarks

- There is a useful observation regarding the form of (4.12). In problems involving a single body in translational acceleration, it is generally desirable to change the frame of reference to a non-inertial frame fixed to the body. This ensures that the body remains centered in the fluid grid and, provided the body is not rotating, obviates the need for reconstructing the interface interpolation and regularization operators and those derived from them. To within numerical error, the Lagrangian forces $\mathsf{f_b}$ (and therefore the first term in (4.12)) are invariant to the change of reference frame, since these forces only depend on the relative velocity between interface and fluid, as should be clear from (4.7). It is well known that, for a purely translational change of reference frame, the equations of motion are unchanged, but, in order to reconcile the computed force with the expected one in the actual (inertial) reference frame, one must add to the former the associated 'buoyancy' force, equal to the product of the displaced mass and the acceleration of the ref-

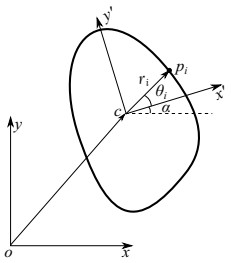

Figure 4.1: Sketch of xy frame and $x'y'$ frame

erence frame. However, this is precisely the final term in (4.12). That is, regardless of the reference frame in which the problem is solved, both terms in the force calculation are unchanged, enabling a somewhat simpler treatment. This invariance to translational changes of reference frame is due to the presence of the enclosed fictitious fluid in the immersed boundary projection method, whose inertial reaction must be countered regardless of the reference frame. A similar effect arises in a change to a rotating frame of reference, but in this case, one must also account for additional pseudo-forces in the equations of motion.

- It is, of course, not a coincidence that the operators that respectively relate velocities and forces are transposes of one another. These two quantities are duals of each other with respect to the rate of energy transfer: the rate of work done by the fluid on the rigid body is given by $\dot{\mathbb{q}}^T \mathbb{f}$. Based on (4.11) and (4.12), this can be written as $-\dot{\mathbb{q}}^T \mathcal{B} \mathsf{f}_\mathsf{b} + \dot{\mathbb{q}}^T \mathbb{M}_f \ddot{\mathbb{q}} = -\mathsf{u}_\mathsf{b}{}^T \mathsf{f}_\mathsf{b} + \dot{\mathbb{q}}^T \mathbb{M}_f \ddot{\mathbb{q}}$. Thus, the transpose property allows the work to be expressed identically in terms of work done on the interface. Because the interface forces act on the fluid on both sides, the second term removes the rate of change of the kinetic energy associated with the motion effected in the fictitious fluid by these forces.

The construction of the body distribution operator $\mathcal{B}$.

As discussed in Section 4.2, the algorithm presented in this paper makes ex-

tensive use of a rigid-body distribution operator, $\mathcal{B} : \mathscr{B} \mapsto \partial\mathscr{B}$, which maps body data to the distributed points on the interface, and its transpose, the resultant operator, $\mathcal{B}^T : \partial\mathscr{B} \mapsto \mathscr{B}$, which collects distributed interface data to compute body quantities. In this section, we give an example of this $\mathcal{B}$ operator for a single two-dimensional rigid body, depicted schematically in Fig. 4.1; however, the procedure for constructing the operator in general multi-body problems in two or three dimensions follows naturally. The inertial coordinate system is denoted by (x, y) and the body-attached system by (x', y'). A polar coordinate system associated with this latter frame is also depicted. The centroid of the body is denoted by c and located instantaneously at $\mathbf{X}_c = (X_c, Y_c)$ relative to the inertial system, and the angle of the body-attached system relative to the inertial system is described by α.

For a rigid body rotating with angular velocity $\mathbf{\Omega}$ and translating with velocity $\mathbf{U}$, the velocity $\mathbf{u}_i$ of one of the M distributed points attached rigidly to the interface—a point p_i located at $\mathbf{x}_i$—is described in the inertial frame by

$$\mathbf{u}_i = \mathbf{U} + \mathbf{\Omega} \times (\mathbf{x}_i - \mathbf{X}_c). \tag{4.13}$$

The resultant force, $\mathbf{F}$, and moment about the centroid, $\mathbf{M}_c$, on the body due to forces $\mathbf{f}_i$, $i = 1, \ldots, M$ acting at the interface points are

$$\mathbf{F} = \sum_{i=1}^{M} \mathbf{f}_i, \qquad \mathbf{M} = \sum_{i=1}^{M} (\mathbf{x}_i - \mathbf{X}_c) \times \mathbf{f}_i. \tag{4.14}$$

These relationships—interface velocities from rigid-body velocities, body forces from interface forces—can be collectively written in matrix form: equation (4.11) for the velocities and—after accounting for the sign and the influence of displaced inertia—equation (4.12) for the force. Importantly, the operators that provide these two relationships are transposes of one another. The velocities in $\mathsf{u_b}$ and

forces in $\mathsf{f_b}$ are arranged in blocks of components, first the M values of the x component, followed by the M values of the y component. The expression for $\mathcal{B}$ is easily obtained from (4.13) or (4.14); here, we write it compactly in its transpose form:

$$\mathcal{B}^T = \begin{bmatrix} 1 & \cdots & 1 & 0 & \cdots & 0 \\ 0 & \cdots & 0 & 1 & \cdots & 1 \\ -(y_1 - Y_c) & \cdots & -(y_M - Y_c) & (x_1 - X_c) & \cdots & (x_M - X_c) \end{bmatrix}. \quad (4.15)$$

This operator can also be expressed in terms of the body-fixed coordinate system and rigid-body configuration by noting that $x_i - X_c = r_i \cos(\theta_i + \alpha)$ and $y_i - Y_c = r_i \sin(\theta_i + \alpha)$.

4.2.2 Rigid body solver

The main task of the rigid body solver is to compute the configurations and velocities of rigid bodies based on the fluid forces exerted on them. For this purpose, we apply the method of Featherstone [38] to formulate the equations of motion for a rigid body system that possibly has internal constraints. It is to be stressed that the fundamental contribution of this paper—the coupling algorithm—is independent of the details of the rigid-body solver, and we offer the following section simply as a brief overview with a simple example, and omit details for complex three-dimensional systems. For such details, we direct the reader to several excellent books on the subject, including [38].

Before discussing the rigid body solver, we first extend the notation introduced in section 4.2.1.2 to allow for multiple bodies. Suppose there are N_b bodies in the system. Let $\mathscr{B}_i$ denote the space of 6-dimensional force and motion vectors associated with the ith body in the system, and $\mathscr{B} = \bigcup_{i=1}^{N_b} \mathscr{B}_i$ the $6N_b$-dimensional space of all such vectors. A motion element of this space would be, for example, the $6N_b$-dimensional column vector $\mathfrak{q} = [\mathfrak{q}_1^T \ \mathfrak{q}_2^T \cdots \mathfrak{q}_{N_b}^T]^T$, and a force element would

be constructed analogously from the individual bodies' forces. It is important to note that the moment and translational velocity in each sub-vector are still defined with respect to the corresponding body's center of volume. Also, it should be noted that the velocity, $\dot{\mathbb{q}}$, and acceleration, $\ddot{\mathbb{q}}$, are taken with respect to a single inertial frame of reference for all bodies.

4.2.2.1 Governing equations

For a rigid body system with no internal constraints, the equations of motion can be expressed compactly as

$$\mathbb{H}\ddot{\mathbb{q}} = \tau, \tag{4.16}$$

where $\mathbb{H}$ is a $6N_b \times 6N_b$ generalized inertia matrix that includes information of both the masses and moments of inertia of the constituent bodies. This matrix is symmetric and positive definite. The vector $\tau \in \mathscr{B}$ consists of the forces and moments exerted by various sources—fluid, internal springs and dampers, gravity, Coriolis, centrifugal, etc—on each body in the system. Each of these equations is expressed relative to a common inertial reference frame.

A rigid body system with internal constraints on its motion—e.g., joints—can be expressed in the form

$$\begin{bmatrix} \mathbb{H} & K^T \\ K & 0 \end{bmatrix} \begin{bmatrix} \ddot{\mathbb{q}} \\ -\lambda \end{bmatrix} = \begin{bmatrix} \tau \\ c \end{bmatrix}. \tag{4.17}$$

The motion constraints, which comprise the second set of equations, have been expressed here as the second time derivative of the implicit—but possibly time-varying—positional constraints,

$$\phi(\mathbb{q}, t) = 0. \tag{4.18}$$

The dependence on time allows for prescribed motions. Thus, the coefficients K and c are simply

$$K = \frac{\partial \phi}{\partial \mathbb{q}}, \quad c = -\frac{\partial^2 \phi}{\partial t^2} - \dot{K}\dot{\mathbb{q}}. \tag{4.19}$$

The variable λ is a vector of Lagrange multipliers, which can be interpreted physically as the set of internal forces and moments on the joints that enforce the constraints.

The constrained system (4.17) has the form of an index-1 differential-algebraic equation (DAE). Führer and Leimkuhler [44] reviewed DAEs for constrained mechanical motion. Some related numerical methods can be found in [49, 50]. A procedure for simplifying the system into a reduced set of ordinary differential equations is detailed in the following section. This procedure relies on a null-space basis for the constraint operator in which to express the system acceleration. When the equations are projected onto the null space, the Lagrange multiplier terms are removed, and a smaller-dimensional system emerges. Note that this procedure is exactly analogous to the approach taken in the fluid, in which the null-space basis forms the discrete curl operator and allows the removal of the pressure (the Lagrange multiplier) in the momentum equations. The reduced rigid-body system is advanced in time with the widely used Runge-Kutta-Fehlberg method (also known as RK45 in many numerical libraries).

4.2.2.2 Reduction of index-1 symmetric differential-algebraic system

Consider a differential-algebraic system of equations of the form arising in mechanical systems,

$$\begin{bmatrix} \mathbb{H} & K^T \\ K & 0 \end{bmatrix} \begin{bmatrix} \ddot{\mathbb{q}} \\ -\lambda \end{bmatrix} = \begin{bmatrix} R_1 \\ R_2 \end{bmatrix}, \tag{4.20}$$

where the inertia matrix $\mathbb{H}$ is $N \times N$ and symmetric; the constraint matrix K is $S \times N$, where $S < N$, and has full row rank (i.e. all constraints are linearly independent); and the acceleration vector $\ddot{\mathrm{q}}$ is $N \times 1$ and the Lagrange multiplier vector λ is $S \times 1$.

Because K has full row rank, one can construct a right permutation matrix, P, of size $N \times N$ so that

$$KP = \begin{bmatrix} K_1 & K_2 \end{bmatrix}, \tag{4.21}$$

where K_1 is an invertible $S \times S$ matrix and K_2 is of size $S \times (N-S)$. For example, this permutation can be determined (non-uniquely) from the LU-decomposition, $KP = L[U_1\ U_2]$, in which the S columns with non-zero pivots in the $S \times N$ upper-triangular matrix U are collected into U_1 (so that $K_1 = LU_1$ and $K_2 = LU_2$). This permutation matrix leads to natural decompositions of $\mathbb{H}$, $\ddot{\mathrm{q}}$ and R_1 into S- and $(N-S)$-sized matrices and vectors:

$$P^T \mathbb{H} P = \begin{bmatrix} \mathbb{H}_1 & 0 \\ 0 & \mathbb{H}_2 \end{bmatrix}, \qquad P^T \ddot{\mathrm{q}} = \begin{bmatrix} \ddot{\mathrm{q}}_1 \\ \ddot{\mathrm{q}}_2 \end{bmatrix}, \qquad P^T R_1 = \begin{bmatrix} R_{11} \\ R_{12} \end{bmatrix}. \tag{4.22}$$

Since P is simply a re-arrangement of the columns of the identity, $\mathbb{1}_N$, it is obvious that $P^{-1} = P^T$.

From the decomposition of K, it is easy to construct a $N \times (N-S)$ matrix Z whose columns span the null space of KP,

$$Z = \begin{bmatrix} -K_1^{-1} K_2 \\ \mathbb{1}_{N-S} \end{bmatrix} \tag{4.23}$$

(where $\mathbb{1}_{N-S}$ is the identity matrix of size $N-S$). That is, $KPZ \equiv 0$, as can be verified. This implies that the homogeneous constraints can be satisfied if we set $\ddot{\mathrm{q}}_1 = -K_1^{-1} K_2 \ddot{\mathrm{q}}_2$. A particular solution of the constraint equations can also be

constructed from the decomposition of K,

$$\ddot{\mathbb{q}}_p = P \begin{bmatrix} K_1^{-1} R_2 \\ 0 \end{bmatrix}. \tag{4.24}$$

Thus, a general (but non-unique) form of the acceleration vector that satisfies the constraint system is

$$\ddot{\mathbb{q}} = \ddot{\mathbb{q}}_p + PZ\ddot{\mathbb{q}}_2. \tag{4.25}$$

The problem therefore reduces to finding the remaining $N - S$ accelerations in $\ddot{\mathbb{q}}_2$ from the equations of motion. Insert this general form into those equations,

$$\mathbb{H}\left(\ddot{\mathbb{q}}_p + PZ\ddot{\mathbb{q}}_2\right) - K^T\lambda = R_1. \tag{4.26}$$

Now, by left-multiplying the system by $Z^T P^T$, we project the equations onto the null space of the constraints in order to eliminate the Lagrange multipliers, so that we get

$$Z^T P^T \mathbb{H} PZ\ddot{\mathbb{q}}_2 = Z^T P^T R_1 - Z^T P^T \mathbb{H}\ddot{\mathbb{q}}_p. \tag{4.27}$$

By virtue of the decompositions of $\mathbb{H}$ and R_1 described above, the reduced $(N-S)$ system of equations can be written as

$$\tilde{\mathbb{H}}_2 \ddot{\mathbb{q}}_2 = \tilde{R}_2 \tag{4.28}$$

where

$$\tilde{\mathbb{H}}_2 \equiv \mathbb{H}_2 + K_2^T (K_1^{-1})^T \mathbb{H}_1 K_1^{-1} K_2, \qquad \tilde{R}_2 \equiv R_{12} - K_2^T (K_1^{-1})^T R_{11} + K_2^T (K_1^{-1})^T \mathbb{H}_1 K_1^{-1} R_2. \tag{4.29}$$

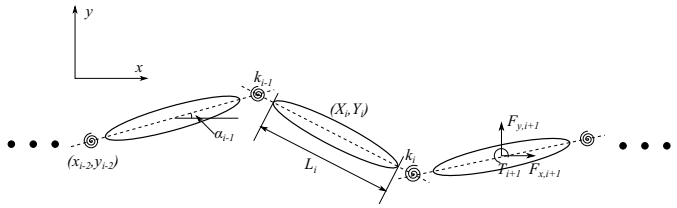

Figure 4.2: Diagram of the linked planar rigid body system.

It is important to note that $\tilde{\mathbb{H}}_2$ is symmetric and positive definite. From the solution of this system, the full acceleration vector can be assembled from (4.25). If one later desires the Lagrange multipliers, they can be recovered by left-multiplying (4.26) by P^T and using the first S equations of the resulting system to solve for λ:

$$\lambda = -(K_1^{-1})^T \left(R_{11} - \mathbb{H}_1 \ddot{\mathrm{q}}_1\right). \tag{4.30}$$

4.2.2.3 An example: System of linked planar rigid bodies

Here, we present an example of how to construct these equations for a real problem. Later in this paper, an articulated system of several linked bodies will be extensively investigated, regarded as a simplified model of a flexible wing or a flapping flag. In general, this kind of system can be sketched as in Fig. 4.2. Suppose there are N_b bodies in the system, numbered consecutively from 1 to N_b, and an equal number of joints numbered from 0 to $N_b - 1$, and that the motion of joint 0—whose coordinates are described by (x_0, y_0)—is prescribed. If the joints permit only rotation, then they pose constraints on the x and y coordinates but not on the angular orientations of the bodies. Thus, the $2N_b$ implicit motion constraints in positional form are

$$x_0(t) + \frac{L_1}{2}\cos\alpha_1 - X_1 = 0, \tag{4.31}$$

$$y_0(t) + \frac{L_1}{2}\sin\alpha_1 - Y_1 = 0, \tag{4.32}$$

$$X_i + \frac{L_i}{2}\cos\alpha_i + \frac{L_{i+1}}{2}\cos\alpha_{i+1} - X_{i+1} = 0, \quad i = 1, ..., N_b - 1, \tag{4.33}$$

$$Y_i + \frac{L_i}{2}\sin\alpha_i + \frac{L_{i+1}}{2}\sin\alpha_{i+1} - Y_{i+1} = 0, \quad i = 1, ..., N_b - 1. \tag{4.34}$$

Now, we write these in the acceleration form. Instead of using the full 6-dimensional vector for each body, we shrink the vector to hold only the $3N_b$ operable degrees of freedom in this planar problem, and rearrange them in the form

$$\mathbb{q} = [X_1, Y_1, X_2, Y_2, \cdots, X_{N_b}, Y_{N_b}, \alpha_1, \alpha_2, \cdots, \alpha_{N_b}].^T \tag{4.35}$$

This latter rearrangement implies the permutation matrix P discussed in the Appendix. Then, the $2N_b \times 3N_b$ constraint matrix K has the form

$$K = \begin{bmatrix} -\mathbb{1}_2 & & & & & & Q_0 & & & & \\ \mathbb{1}_2 & -\mathbb{1}_2 & & & & & Q_0 & Q_1 & & & \\ & \mathbb{1}_2 & -\mathbb{1}_2 & & & & & Q_1 & Q_2 & & \\ & & \ddots & \ddots & & & & & \ddots & \ddots & \\ & & & \mathbb{1}_2 & -\mathbb{1}_2 & & & & & Q_{N_b-2} & Q_{N_b-1} \end{bmatrix} \tag{4.36}$$

where $\mathbb{1}_2$ is the 2×2 identity matrix and $Q_i = \frac{1}{2}L_{i+1}[-\sin\alpha_{i+1}, \cos\alpha_{i+1}]^T$. Because the permutation matrix is already implicit in the organization of $\mathbb{q}$, this form of K is already split into K_1 (the block of identity matrices) and K_2 (the Q_i block).

The inverse of K_1 is readily found to be a lower triangular matrix

$$K_1^{-1} = -\begin{bmatrix} \mathbb{1}_2 & & & & \\ \mathbb{1}_2 & \mathbb{1}_2 & & & \\ \mathbb{1}_2 & \mathbb{1}_2 & \mathbb{1}_2 & & \\ \vdots & & \ddots & \ddots & \\ \mathbb{1}_2 & \dots & & \mathbb{1}_2 & \mathbb{1}_2 \end{bmatrix}. \tag{4.37}$$

Furthermore, the right-hand side of the constraints is $c = [c_0, c_1, ..., c_{N_b-1}]^T$, where

$$c_i = \begin{cases} -[\ddot{x}_0(t), \ddot{y}_0(t)] + \frac{1}{2}\left[L_{i+1}\dot{\alpha}_{i+1}^2 \cos\alpha_{i+1}, L_{i+1}\dot{\alpha}_{i+1}^2 \sin\alpha_{i+1}\right] & i = 0 \\ \frac{1}{2}\left[L_i\dot{\alpha}_i^2 \cos\alpha_i + L_{i+1}\dot{\alpha}_{i+1}^2 \cos\alpha_{i+1}, L_i\dot{\alpha}_i^2 \sin\alpha_i + L_{i+1}\dot{\alpha}_{i+1}^2 \sin\alpha_{i+1}\right] & i = 1, ..., N_b - 1 \end{cases} \tag{4.38}$$

The generalized inertia matrix $\mathbb{H}$ is

$$\mathbb{H} = \begin{bmatrix} M & \\ & I_C \end{bmatrix} \tag{4.39}$$

where

$$M = \begin{bmatrix} M_1 & & & & & & \\ & M_1 & & & & & \\ & & M_2 & & & & \\ & & & M_2 & & & \\ & & & & \ddots & & \\ & & & & & M_{N_b} & \\ & & & & & & M_{N_b} \end{bmatrix}, \quad I_C = \begin{bmatrix} I_{C,1} & & & \\ & I_{C,2} & & \\ & & \ddots & \\ & & & I_{C,N_b} \end{bmatrix}, \tag{4.40}$$

and where M_i is the mass of body i and $I_{C,i}$ is its scalar moment of inertia about

the centroid.

The forces and moments exerted on each plate can be collected into the $3N_b$-dimensional vector

$$\tau = \mathbb{f} + \mathbb{f}_b - \mathbb{K}\mathbb{q} - \mathbb{R}\dot{\mathbb{q}}, \tag{4.41}$$

where $\mathbb{f}$ are the fluid forces and moments exerted on each body, $\mathbb{f}_b$ contains the moments due to body forces such as gravity. Note that, as described above, the moments are taken about each corresponding body's centroid; since we assume in this work that the bodies have uniform density, the moments due to gravity are therefore zero. In the final two terms, $\mathbb{K}$ and $\mathbb{R}$ are $3N_b \times 3N_b$ matrices of the torsion stiffnesses and dampers of the joints, $k_0, \ldots, k_{N_b-1}$ and $r_0, \ldots, r_{N_b-1}$, respectively. These matrices have the form

$$\mathbb{K} = \begin{bmatrix} 0 & 0 \\ 0 & \mathbb{K}_2 \end{bmatrix}, \qquad \mathbb{R} = \begin{bmatrix} 0 & 0 \\ 0 & \mathbb{R}_2 \end{bmatrix}, \tag{4.42}$$

where the upper left zero block in each is of size $2N_b \times 2N_b$, since the joints apply only moments in response to bending and bending rate of change. The lower right block is of size $N_b \times N_b$ and tridiagonal; for example,

$$\mathbb{K}_2 = \begin{bmatrix} k_0 + k_1 & -k_1 & 0 & & \\ -k_1 & k_1 + k_2 & -k_2 & & \\ & \ddots & \ddots & \ddots & \\ & & -k_{N_b-2} & k_{N_b-2} + k_{N_b-1} & -k_{N_b-1} \\ & & 0 & -k_{N_b-1} & k_{N_b-1} \end{bmatrix}, \tag{4.43}$$

and analogously for $\mathbb{R}_2$. Now, we have specified every piece of the dynamical equations.

4.2.3 Coupling algorithm

In this section, a partitioned method is introduced to couple the fluid and the rigid body solvers described above. Treating both solvers as black boxes, their notation can be simplified with inputs and outputs as

$$\mathbb{f} = FS(\mathsf{x_b}, \mathsf{u_b}) \tag{4.44}$$

$$(\mathsf{x_b}, \mathsf{u_b}) = RBS(\mathbb{f}) \tag{4.45}$$

where *FS* and *RBS* stand for the Fluid Solver and the Rigid Body Solver, respectively. An important feature of these two solvers is that they can form a loop in which the outputs of one solver can be used as the inputs of the other one and vice versa. Considering that strong (or dynamical) coupling requires that the full set of variables $(\mathbb{f}, \mathsf{x_b}, \mathsf{u_b})$ satisfies both solvers at the end of each time step, this loop structure is naturally conducive to an iterative approach. Here, an iterative algorithm is proposed and depicted schematically in Fig. 4.3.

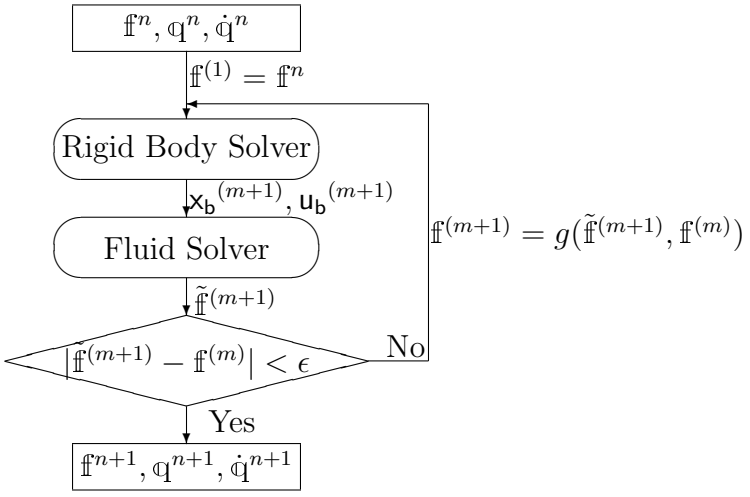

Figure 4.3: Flowchart of the strongly coupled algorithm

The basic idea of the algorithm is to use the force $\mathbb{f}$ as the primary iterative variable. At time t^n, the body configuration $\mathbb{q}^n$, velocity $\dot{\mathbb{q}}^n$ and fluid force $\mathbb{f}^n$ are assumed known. In every iteration of the ensuing step to t^{n+1}, a force $\mathbb{f}^{(m)}$

is proposed based on either the result from the previous time step (for the first iteration) or some combination of the previous iteration results. This force iterate is used by the rigid body solver to update the interface positions $\tilde{\mathsf{x}}_\mathsf{b}$ and velocities $\tilde{\mathsf{u}}_\mathsf{b}$. These are, in turn, passed into the fluid solver, from which a correction of the resultant force $\tilde{\mathbb{f}}^{(m+1)}$ is computed. The proposed and corrected forces, $\mathbb{f}^{(m)}$ and $\tilde{\mathbb{f}}^{(m+1)}$, are compared at the end of the iteration; if they are sufficiently close, the step is considered converged; otherwise another iteration is initiated, from a new proposed force $\mathbb{f}^{(m+1)}$ based on some combination of $\mathbb{f}^{(m)}$ and $\tilde{\mathbb{f}}^{(m+1)}$.

In this work, the proposed force is calculated from a relaxation scheme, which has the form

$$\mathbb{f}^{(m+1)} = (1-\omega)\mathbb{f}^{(m)} + \omega\tilde{\mathbb{f}}^{(m+1)}, \tag{4.46}$$

where ω is the relaxation parameter. The choice of this parameter will be discussed in the following section. This kind of iterative scheme is sometimes referred to as block Gauss-Seidel process in the literature [76, 60].

It is important to note that only equation (4.7) of the fluid solver needs to be computed in every iteration. The first equation (4.6) advances the vorticity field in the absence of bodies to obtain the intermediate vorticity field. Considering that no body information is needed, it only needs to be calculated once in every time step. The second equation, (4.7), governs the Lagrange forces that correct for the spurious slip velocity on the body interfaces. In the coupling algorithm, this equation is computed repeatedly as both the left- and right-hand sides are updated in every iteration; only these Lagrange forces are needed to provide the correction force $\tilde{\mathbb{f}}^{(m+1)}$. The third and fourth equations, (4.8) and (4.9), provide only the corrected vorticity and velocity, and need only be computed once at the end of the time step. In other words, in each iteration, we only seek the constraint force that ensures compatibility of the fluid and body velocities; the associated

fluid velocity field is immaterial to this calculation. This observation results in substantial computational savings over other immersed boundary methods that must calculate the interface force from the fluid velocity field or conforming-grid methods that require an update of the mesh itself in each iteration.

The procedure of advancing the fluid and body state by the proposed coupling algorithm from time t^n to $t^{n+1} = t^n + \Delta t$ is summarized here:

Substep 1. *Intermediate field*

The intermediate vorticity field γ^* is solved by equation (4.6).

Substep 2. *Correction force calculation*

The body configuration $\mathbb{q}$, body velocity $\dot{\mathbb{q}}$ and fluid force $\mathbb{f}$ are calculated in this step. For the first iteration $m = 1$, $\mathbb{f}^{(1)}$, $\mathbb{q}^{(1)}$ and $\dot{\mathbb{q}}^{(1)}$ are set to the solution from the last time step, $\mathbb{f}^n$, $\mathbb{q}^n$ and $\dot{\mathbb{q}}^n$.

2 (a): *Body evolution*

Compute the next iterates $\mathbb{q}^{(m+1)}$ and $\dot{\mathbb{q}}^{(m+1)}$ by advancing the rigid-body system equation (4.17) by one time step, based on $\mathbb{f}^{(m)}$.

2 (b): *Fluid equation preparation*

Calculate the updated interface positions $\mathsf{x_b}^{(m+1)}$ and velocities $\mathsf{u_b}^{(m+1)}$ from equation (4.10) and (4.11), respectively. Update the interpolation operator E with the new interface position.

2 (c): *Interface forces*

Solve for the updated interface forces, $\mathsf{f_b}^{(m+1)}$, via equation (4.7).

2 (d): *Convert interface force*

Update the resultant force on the bodies $\tilde{\mathbb{f}}^{(m+1)}$ from the interface forces $\mathsf{f_b}^{(m+1)}$ via equation (4.12).

2 (e): *Convergence check*

The convergence is checked from the force error, defined as

$$\epsilon^{(m+1)} = \max \left| \tilde{\mathbb{f}}^{(m+1)} - \mathbb{f}^{(m)} \right|. \tag{4.47}$$

This error is compared with a pre-determined tolerance for convergence. If not yet converged, the algorithm returns to 2(a) with an updated $\mathbb{f}^{(m+1)}$ via equation (4.46). If converged, then set $\mathbb{q}^{n+1} = \mathbb{q}^{(m+1)}$, $\dot{\mathbb{q}}^{n+1} = \dot{\mathbb{q}}^{(m+1)}$, and $\mathbb{f}^{n+1} = \tilde{\mathbb{f}}^{(m+1)}$ and stop.

Substep 3. *Final state vectors*

The final vorticity field γ^{n+1} is computed from equation (4.8), and the fluid velocity u^{n+1} from equation (4.9).

4.2.3.1 Stability

The stability of the iterative algorithm is inspected in this section. To simplify the analysis, we consider the example of a single rigid body without constraint and apply basic forward Euler time marching to this rigid body, but the essence of the result holds for constrained systems and more advanced time marching schemes, as well. Let us consider the set of equations that must be solved in one iteration of substep 2 of the algorithm presented above:

$$\begin{aligned}
&\mathbb{H}\ddot{\mathbb{q}}^{(m+1)} = \mathbb{f}^{(m)} + \mathbb{f}_b \\
&\dot{\mathbb{q}}^{(m+1)} = \dot{\mathbb{q}}^{n} + \Delta t \ddot{\mathbb{q}}^{(m+1)} \\
&\tilde{\mathsf{A}}^{(m+1)} \mathsf{f_b}^{(m+1)} = \mathcal{B}^{(m+1)} \dot{\mathbb{q}}^{(m+1)} - \mathsf{U}_\infty^{n+1} - \mathsf{E}^{(m+1)} u^* \\
&\mathbb{f}^{(m+1)} = (1-\omega)\mathbb{f}^{(m)} + \omega \left[- \left(\mathcal{B}^{(m+1)} \right)^T \mathsf{f_b}^{(m+1)} + \mathbb{M}_f \ddot{\mathbb{q}}^{(m+1)}. \right]
\end{aligned} \tag{4.48}$$

Here, we have defined $\tilde{\mathsf{A}} \equiv \mathsf{E}C(-L)^{-1}A^{-1}C^T\mathsf{E}^T$, the left-hand-side interface operator in (4.7); this changes with each iteration as the body moves relative to the grid, thereby affecting the interpolation and regularization operators. Also,

$u^* \equiv C(-L)^{-1}\gamma^*$ is the intermediate velocity field due to flow convection and diffusion, without regard for the body; this is computed only once before the iterations start. We also allow for an unsteady free stream velocity.

Let us define the 6×6 matrix operators $\Phi_1 \equiv -\Delta t \mathcal{B}^T \tilde{\mathsf{A}}^{-1} \mathcal{B} \mathbb{H}^{-1}$ and $\Phi_2 \equiv \mathbb{M}_f \mathbb{H}^{-1}$, and denote their sum as Φ. This operator Φ, when acting upon a force vector on the body, returns the force exerted by the fluid in reaction to the resulting change in the body's velocity; it is effectively the virtual inertia of the fluid, though it also accounts for the diffusion of newly-created vorticity. It is important to note that this operator (particularly Φ_1) changes with each iteration through changes in the body resultant operator $\mathcal{B}$ (due to incremental body rotation) and in the interface operator $\tilde{\mathsf{A}}^{-1}$ (due to motion relative to the grid). Let us also define

$$\mathbb{f}_r \equiv \mathcal{B}^T \tilde{\mathsf{A}}^{-1} \left[\mathsf{E} u^* + \mathsf{U}_\infty^{n+1} - \mathcal{B}(\dot{\mathbb{q}}^n + \Delta t \mathbb{H}^{-1} \mathbb{f}_b) \right] + \mathbb{M}_f \mathbb{H}^{-1} \mathbb{f}_b,$$

which is the residual force exerted by the fluid on the body due to motion effected only by body forces, such as gravity. This residual changes with each iteration due to the same influences as on Φ; that is, it is only affected by incremental rotation and motion relative to the grid. Combining the equations (4.48) results in the following update equation for the fluid force on the body,

$$\mathbb{f}^{(m+1)} = (1-\omega)\mathbb{f}^{(m)} + \omega \left(\Phi^{(m+1)} \mathbb{f}^{(m)} + \mathbb{f}_r^{(m+1)} \right). \tag{4.49}$$

In order to examine the stability, we must show that the difference in this force (the 'force error') decreases from one iteration to the next. Subtracting (4.49) for one iteration from the next, the corresponding update of the force error is

$$\Delta\mathbb{f}^{(m+1)} = \left[(1-\omega)\mathbb{1}_6 + \omega \Phi^{(m)} \right] \Delta\mathbb{f}^{(m)} + \omega \left(\Delta\mathbb{f}_r^{(m+1)} + \Delta\Phi^{(m+1)} \mathbb{f}^{(m)} \right), \tag{4.50}$$

where $\mathbb{1}_6$ denotes the 6×6 identity and $\Delta(\cdot)^{(m+1)} \equiv (\cdot)^{(m+1)} - (\cdot)^{(m)}$. From

the expression above, we can note that the force error comes from two parts. The first part is clearly associated with the propagation of the error from the previous iteration; the second, in contrast, is due to incremental rotation of the body and change of the alignment between the body and the Cartesian grid. This second term, which we refer to as the *alignment error*, is challenging to parse further for general cases. However, from our interpretation, a simple form of this error can be concluded as $\epsilon = C(\Delta\mathbb{q}^{(m+1)})(\mathbb{f}^{(m)} + \mathbb{f}_b)$, where $C(\Delta\mathbb{q}^{(m+1)})$ is a non-dimensional function. Several numerical tests have shown the trend that the function C approaches zero with the decrease of $\Delta\mathbb{q}$. An upper bound C_u can also be found for this function and is at the order of $\mathcal{O}(10^{-4})$. This suggests that we should choose the convergence criteria such that the threshold for force error is greater than this alignment error.

For stability analysis, we focus on the error propagation in (4.50). The form of Φ resists detailed analysis for general cases. However, based on our physical interpretation of Φ above, we can conclude that Φ is roughly equal to the ratio of the virtual to intrinsic inertia of the body. For example, if the body is a circular cylinder of radius R and density ρ_b, for which the translational virtual inertia is equal to $\rho_f \pi R^2$,

$$\Phi^{(m+1)} \Delta\mathbb{f}^{(m)} \sim -\frac{\rho_f}{\rho_b} \Delta\mathbb{f}^{(m)},$$

where the negative sign reflects the fact that this represents a reaction to acceleration. Thus, the update of force error on the body is given approximately by

$$\Delta\mathbb{f}^{(m+1)} = \left(1 - \omega - \omega\frac{\rho_f}{\rho_b}\right) \Delta\mathbb{f}^{(m)} + \omega\epsilon. \tag{4.51}$$

For convergence, the parenthetical factor must be bounded in $(-1, 1)$; ideally, we want to minimize it. Both can be achieved by tuning the relaxation parameter ω

to ensure that the parenthetical factor vanishes, leading to

$$\omega = \frac{\rho_b}{\rho_b + \rho_f}. \tag{4.52}$$

For a plate with infinitesimal thickness, with length L and mass per unit area ρ_b' (and arbitrary width), the relaxation parameter would be $\omega = 4\rho_b'/(\rho_f \pi L + 4\rho_b')$.

For general body shapes in two or three dimensions, then the stability bounds on the iterative scheme require that the relaxation factor lies in the range

$$0 < \omega < 2\omega^*, \tag{4.53}$$

where ω^* is strictly defined in terms of $\Phi^{(m)}$ and represents the choice of relaxation parameter that ensures the fastest convergence rate. Here, it is defined more loosely—without strict guarantee of convergence—in a manner inspired by the simple two-dimensional cases described above, based on the virtual inertia matrix of the body expressed in its own coordinate system, denoted by $\mathbb{M}_a$:

$$\omega^* \equiv ||(\mathbb{H} + \mathbb{M}_a)^{-1}\mathbb{H}||_2, \tag{4.54}$$

in which the spectral norm of the matrix has been used. For most body shapes, these inertia matrices are diagonal, so the relaxation parameter is simply the largest diagonal element of the matrix.

For systems of bodies, in which the virtual inertias of all bodies are coupled, we have found that it is sufficient to compute the stability range of each body in isolation and then choose a value of ω^* in the intersection of these ranges. There appears to be some flexibility in choosing ω to obtain good performance. For example, in a study of plates with non-rectangular planform (not reported here), we computed the relaxation parameter from the virtual inertia of a rectangular plate of equivalent area and still achieved good performance. In general, we have

found in a variety of example problems that the number of iterations required for each time step is usually between 2 and 4.

We note that this use of relaxation, in which the virtual inertia of the fluid is used to ensure rapid convergence, leads to an algorithm that is similar to that proposed by Eldredge [32]. In that work, the virtual inertia was explicitly identified in the fluid force expression and grouped with the intrinsic body inertia; this required the calculation of the full virtual inertia matrix in every iteration, but enabled simulation of bodies even with zero intrinsic mass. Here, we only use a single (constant) relaxation parameter based on the same principle. This enables simulation of bodies with very small—but not identically zero—ratios of intrinsic mass to virtual mass. We have been successful in obtained a convergent algorithm with bodies with as little as one percent of the density of the fluid.

4.3 Implementation

A numerical library, *whirl*, is developed to integrate various Navier-Stokes solvers, rigid-body system solvers and strong coupling algorithms for fluid-structure interaction problems. Some practical experience

4.3.1 Solving of the body force

By reviewing the whole solver procedure, equation 4.7 is repeatedly solved in the iterative scheme. Thus, its solving speed plays a big role in the overall performance of the whole solver.

4.3.1.1 Physical meaning

In order to construct an effective way to solve this equation, it is important to understand the physical meaning of every operator in the equation.

- Right Hand Side:

  Term $\mathsf{u_b} - \mathsf{U}_\infty - \mathsf{E}C(-L^{-1})\gamma^*$ indicates the velocity difference between the boundary velocity and the velocity value along the boundary interpolated from the neighboring cells. The size of this vector is $lm \times 1$, where m is the total number of points that describe the body and l represents the dimension of the problem, either 2 or 3.

- Left Hand Side:

  1. f_b: the boundary force on body at the boundary points.
  2. $\mathsf{E}^T f_b$: the forcing term on the Cartesian grid smeared from the singular boundary force by the regularization operator. Considering that the regularization is a local operator, the effect should be close to the body. In another word, the values in this Cartesian field should be zeros, except those near the body.
  3. $C^T\mathsf{E}^T f_b$: rotational part of the forcing (or the correction vorticity) near the body. The effect is still close to body as the curl operator is local.
  4. $A^{-1}C^T\mathsf{E}^T f_b$: the diffused correction vorticity. As Δt is small, the effect should be confined. Until this step, most points in this Cartesian field has zero value except those near the body.
  5. $(-L^{-1})A^{-1}C^T\mathsf{E}^T f_b$: the streamfunction computed by the diffused correction vorticity. As the Laplacian is a global operator, the resulting field spread out a lot. The decay rate of the field is $1/r$.
  6. $C(-L^{-1})A^{-1}C^T\mathsf{E}^T f_b$: the velocity calculated from the diffused correction vorticity.
  7. $\mathsf{E}C(-L^{-1})A^{-1}C^T\mathsf{E}^T f_b$: the velocity on the boundary point of the body. This velocity is interpolated from the fluid velocity in neighboring cells.

In general, the meaning of this equation is to find a proper force term that can cancel the difference between the intermediate velocity and the desired velocity at the body boundary.

4.3.1.2 The concept of "reference domain"

An in-house GMRES solver is used to solve Before we can solve the body force, the last obstacle is to construct the left-hand-side operator for equation 4.7, or more specifically, how to build A^{-1} and $(-L^{-1})$ operators. Instead of computing the inverse matrix directly, we choose to solve the corresponding equations. For example, the result of operation $A^{-1}b$ can be achieved by solving x in $Ax = b$. A set of Cartesian domains is therefore desired to solve this type of equations. We call these domains as "reference domain".

One of the biggest advantage of using the reference domains is the shrink of domain size. By reviewing the physical meaning of equation 4.7, it is found that all source terms are near the body boundary, like $C^T\mathsf{E}^T f_b$ in solving $A^{-1}C^T\mathsf{E}^T f_b$. As a result, the size of the reference domain is only related to the size of the body. This size is usually smaller that the size of fluid domains where equation 4.6 is solved. For the examples we have implemented, the reference domains are typically half the size of the fluid domains, which shrink the size of LHS matrix to 1/16(2D) or 1/64(3D) of those in fluid domains. This helps to accelerate the iterative procedure of the conjugate gradient method. Secondly, it is easy to group and manage these domains as they are only used in iterative methods for treating bodies. We can simply remove all of them if we are dealing with a fluid problem without any body.

4.3.2 Use of other packages

Multiple packages are integrated into *whirl* library for an easy implementation.

- Parallel Particle Mesh (PPM)

  The Parallel Particle Mesh library has been widely extended in our work. New data structures, like *set*, *level*, *domain*, etc and operators, i.e. curl, divergence on a staggered grid, have been added into it to build our *whirl* library.

- HYPRE

  HYPRE is a library for solving large, sparse linear systems of equations on massively parallel computers. It includes many common iterative methods, like multigrid method, conjugate gradient method, etc. All Poisson equations described in our methods are solved by HYPRE. From our experience, it is fast to use multigrid method to solve Poisson equations in two-dimensional problems, while for those in three-dimensional problems, the conjugate gradient method is a better choice.

- GUN Scientific Library (GSL)

  The ordinary differential equation solver in GSL is applied in our rigid-body solver. Considering that this library is written in C/C++, an general interface is also include in our *whirl* library.

CHAPTER 5

High Fidelity Simulation Results

5.1 Results

In this section, the proposed fluid/rigid-body coupling algorithm is applied to several problems, both in two and three dimensions. The first problem is the free-fall of a circular cylinder in a viscous fluid, which is used to evaluate the accuracy of our algorithm. The second problem involves a passive wing flapping in a viscous fluid and the results are compared with previous experiments and numerical simulations. Then, the passive flapping of several linked plates in a free stream—which approximates the dynamics of a flapping flag—is investigated. Finally, the physics of a three-dimensional pivoting plate are explored, with particular attention to the effect of the aspect ratio of the plate.

5.1.1 Falling circular cylinder

In this section, we perform a convergence study of our coupling algorithm by simulating a circular cylinder falling in viscous fluid under its own weight. The cylinder in this case has a diameter D and a density twice that of the fluid, $\rho_b = 2\rho_f$. It is released from rest in a fluid with kinematic viscosity ν under the influence of gravity, g. The Reynolds number is defined based on gravity, $g^{1/2}D^{3/2}/\nu$, and is set to 200. To efficiently but accurately capture the wake structure behind the falling cylinder, the simulations are conducted in a non-inertial frame fixed to the body, with the center of the cylinder fixed at $(0, 0)$. The free

Case	$\Delta t(g/D)^{1/2}$	$\Delta x/D$
1	0.01	0.04
2	0.005	0.02
3	0.0025	0.01
4	0.00125	0.005

Table 5.1: Verification test cases for falling cylinder.

Case	$\bar{v}_t/(gD)^{1/2}$	p	$St(= fD/\bar{v}_t)$	p
1	-1.0882	-	0.1795	-
2	-1.0992	-	0.1823	-
3	-1.1043	1.14	0.1835	1.222
4	-1.1066	1.15	0.1840	1.263

Table 5.2: The mean terminal velocity, Strouhal number, and extrapolated order of accuracy from each.

stream velocity is set equal to the negative of the instantaneous body translational velocity. The cylinder's rotational and transverse translational degrees of freedom are constrained.

Four grid levels are used in the multi-domain treatment. The largest and coarsest of these has physical dimensions $[-32, 32] \times [-16, 48]$ (scaled by D), and the three finer domains are nested inside with dimensions $[-16, 16] \times [-8, 24]$, $[-8, 8] \times [-4, 12]$ and $[-4, 4] \times [-2, 6]$, respectively, each with half the grid spacing of the next-coarser level. The time step size, Δt, is common to all domains. This time step size and the grid spacing in the finest domain (denoted simply as Δx) are reported in Table 5.1 for the four verification test cases. For all cases, the CFL number, $(gD)^{1/2}\Delta t/\Delta x$, is fixed at 0.25, and the relaxation parameter, ω, is set to 2/3. The spacing between interface points on the cylinder is uniform and of the same order as the finest grid resolution in each case. The convergence criterion for this problem is set to 10^{-4}.

The vorticity fields produced by the falling cylinder are plotted at five instants in Fig. 5.1. The growth of symmetric wake vortices is depicted at the early stage, followed by breakdown of the long wake and transition to periodic vortex shedding.

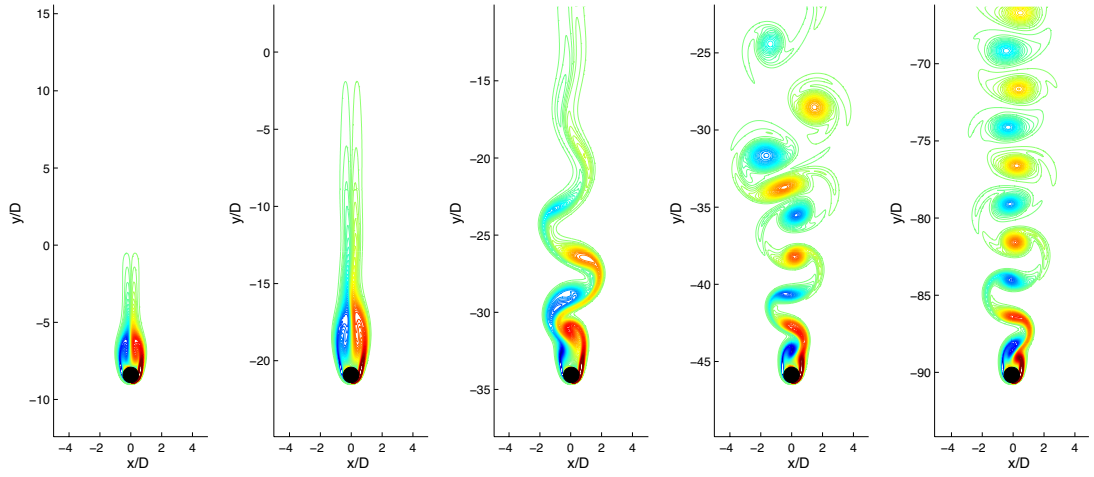

Figure 5.1: Vorticity field generated by falling cylinder with $g^{1/2}D^{3/2}/\nu = 200$, shown at five instants, left to right: $(g/D)^{1/2}t = 10, 20, 30, 40, 80$. Vorticity contours have values from -5 to 5 in 100 uniform increments

For the sake of comparison, the y axis corresponds to the real position of the cylinder in an inertial frame of reference with its origin at the initial location of the cylinder.

The time histories of velocity and acceleration are presented in Fig. 5.2. An acceleration process is observed in the early stage as the wake grows. As the long wake vortices become unstable and roll up into discrete vortices, the associated increase in drag results in a rapid deceleration (positive acceleration) indicated by the peak in the acceleration plot. Then, the falling cylinder wake system transforms itself into a periodic vortex shedding state. It is worth mentioning that the acceleration and velocity profiles at early stage have good agreements with the available results from Eldredge (2008) [32].

The order of accuracy of the overall fluid/rigid-body interaction solver depends on the numerical methods implemented in each solver. In the current study, a second-order semi-implicit method is used to solve the fluid equations and the Runge-Kutta-Fehlberg method, with 4th order accuracy, is applied to solve the rigid body dynamics; the immersed boundary projection method, as with most other immersed boundary methods, reduces the spatial accuracy to between first

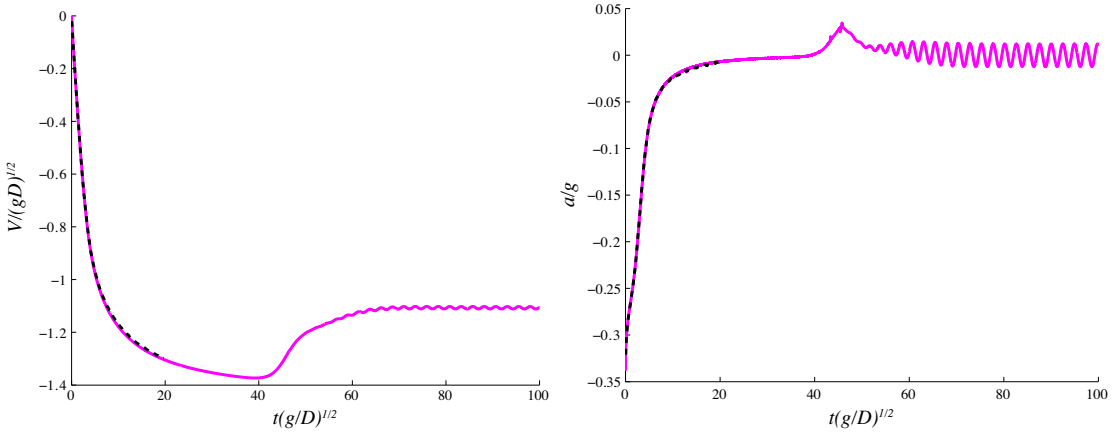

Figure 5.2: (a) Velocity and (b) acceleration of falling cylinder. Present results (verification case 4), magenta solid; Eldredge (2008) [32], black dashed.

and second order [18]. As a result, the overall order of accuracy for the coupling method should be no higher than the second order. The observed order of accuracy p can be calculated from Richardson extrapolation,

$$p = \log\left(\frac{|v_{4\Delta x} - v_{2\Delta x}|}{|v_{2\Delta x} - v_{\Delta x}|}\right) / \log(2), \tag{5.1}$$

where v is some variable evaluated from simulations on grids of different resolution (denoted by Δx, $2\Delta x$, $4\Delta x$). Here, the mean terminal velocity, $\bar{v}_t$, and the Strouhal number based on it are investigated; these, as well as the corresponding observed order of convergence, are reported in Table 5.2. The estimated order of convergence of both velocity and Strouhal number are between first and second order, which is consistent with the overall second-order coupling solver.

5.1.2 Flapping of a flexible wing

In this section, we compute the flapping of a two-dimensional wing with flexible hinge, introduced by Toomey & Eldredge [114]. That work consisted of a comparison between experimental and numerical results, and we make a comparison with both sets of results here. The model consists of two rigid bodies connected

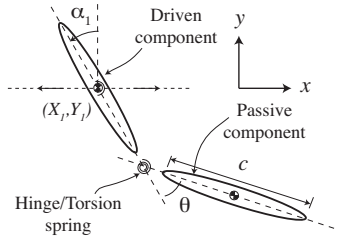

Figure 5.3: Sketch of the system with two elliptical sections connected by a torsion spring

Case No.	A_0/c	β	σ_t	σ_r	Φ	Re_t
1	1.4	$\pi/4$	0.628	0.628	0	100
2	1.4	$\pi/4$	3.770	3.770	0	100

Table 5.3: Kinematic parameters for flexible flapping wing study.

by a torsion spring, as shown in Fig. 5.3. One body–the 'driven body'—has its motion prescribed, while the other one responds passively to the aerodynamic and elastic/inertial forces. Each rigid body has 5:1 aspect ratio elliptical shape with major axis of length c; the bodies are separated by a gap of width $0.1c$, which makes the total length of the wing $2.1c$. The hinge joining the two sections consists of a torsion spring of stiffness $k/(\rho_f f^2 c^4) = 456$ and damping coefficient $r/(\rho_f f c^4) = 3.95$.

We apply the same kinematics reported in [114] to the driven body. The body oscillates rectilinearly along and rotationally about its centroid with a motion described mathematically by

$$X_1(t) = \frac{A_0}{2}\frac{G_t(ft)}{\max G_t}C(ft) \tag{5.2}$$

$$Y_1(t) = 0 \tag{5.3}$$

$$\alpha_1(t) = -\beta\frac{G_r(ft)}{\max G_r} \tag{5.4}$$

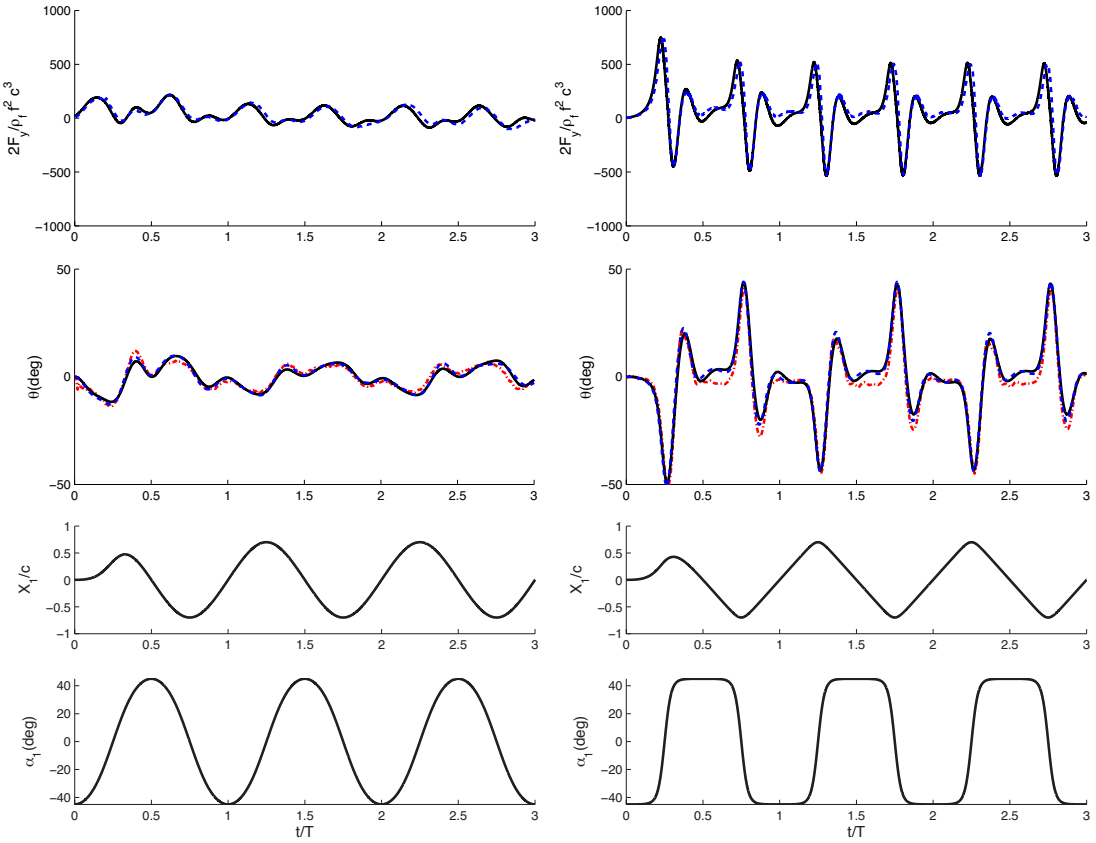

Figure 5.4: Lift (top row), deflection angle of hinge (second row), prescribed translational position (third row) and prescribed angle (last row) for flexible flapping wing. Case 1 (left) and case 4 (right). Current results (black solid), numerical results from [114] (blue dashed), experimental results from [114] (red dash-dot).

where f is the cyclic frequency, the translational shape function is

$$G_t(t) = \int_t \tanh[\sigma_t \cos(2\pi t')]\, \mathrm{d}t' \tag{5.5}$$

and the rotational shape function is

$$G_r(t) = \tanh[\sigma_r \cos(2\pi t + \Phi)], \tag{5.6}$$

where Φ is the phase lead of rotation. The impulsive motion is avoided with a

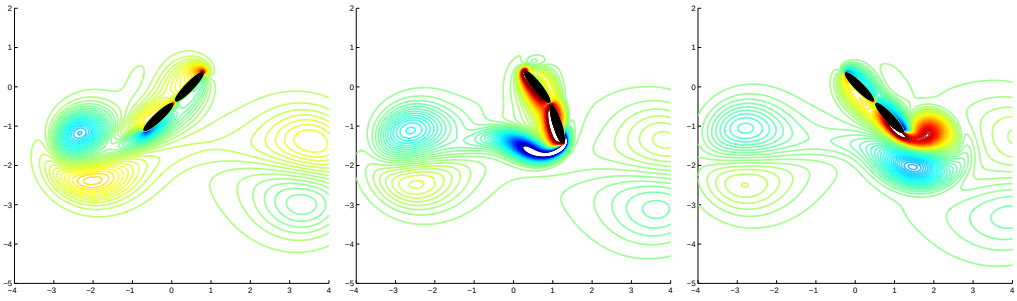

(a) $t/T = 1.14$ (b) $t/T = 1.30$ (c) $t/T = 1.47$

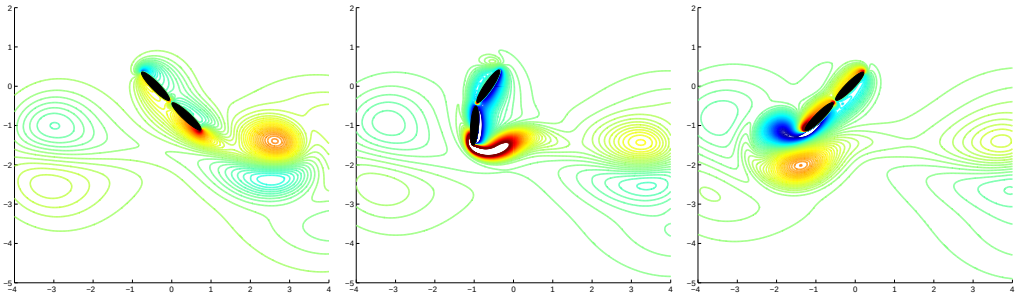

(d) $t/T = 1.63$ (e) $t/T = 1.80$ (f) $t/T = 1.96$

Figure 5.5: Case 2, snapshots of the vorticity field at different instants.

start-up conditioner given by

$$C(t) = \frac{\tanh(8t - 2) + \tanh 2}{1 + \tanh 2}. \tag{5.7}$$

The kinematic parameters for two test cases are presented in Table 5.3. The first case corresponds to approximately sinusoidal heaving and pitching of the wing, whereas the second consists of intervals of nearly steady translations at fixed angle of attack, joined by rapid pitches and changes of direction at the end of each half-stroke. These rapid motions lead to large deflections of the hinge, providing a useful target for evaluating the coupled dynamics solver.

Four grid levels are applied to this problem and their sizes are, from coarsest to finest, $[-16, 16] \times [-24, 8]$, $[-8, 8] \times [-12, 4]$, $[-4, 4] \times [-6, 2]$ and $[-2, 2] \times [-3, 1]$, all scaled by c. For both test cases, the finest grid resolution is $\Delta x = 0.01c$ and the time step is $\Delta t = 0.005T$, where $T = f^{-1}$ is the period of oscillation. These are similar to those applied in the numerical study of [114], in which a viscous

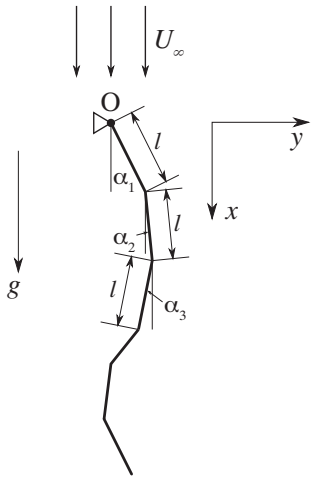

Figure 5.6: Sketch of the linked plates

vortex particle method was used.

The overall comparison of the lift and the hinge deflection angle with the results of Toomey & Eldredge [114] is depicted in Fig. 5.4. These plots show that the current results agree well with both the experimental and simulation results of the previous work. (Note that experimental results for lift are not available in [114].) In case 2, the current results differ significantly from the experimental results during the middle portion of alternating half-strokes, while the wing is driven at nearly constant speed and fixed angle. However, the current results agree well with the other numerical results for this case, suggesting some subtle differences between the experimental set-up and computational description of the problem. As shown in Fig. 5.5, which presents several snapshots of the vorticity field during one period from $t/T \in [1, 2]$, the passive section of the wing interacts strongly with shed vorticity during these intervals. The lack of symmetry from half-stroke to half-stroke is due to the persistent effect of the initial choice of heaving direction, which is encoded in the vorticity that lingers in the vicinity of the wing.

Case	$\rho_b'/(\rho_f L)$	Re	$\eta/(\rho_f U_\infty^2 L^3)$	gL/U_∞^2	N
1	1.5	200	0.01	0.5	10
2	1.5	200	0.01	0.5	50
3	1.5	1000	0.001	0.5	50
4	0.25	200	0	0	10
5	0.1	200	0	0	10

Table 5.4: Linked plates test cases

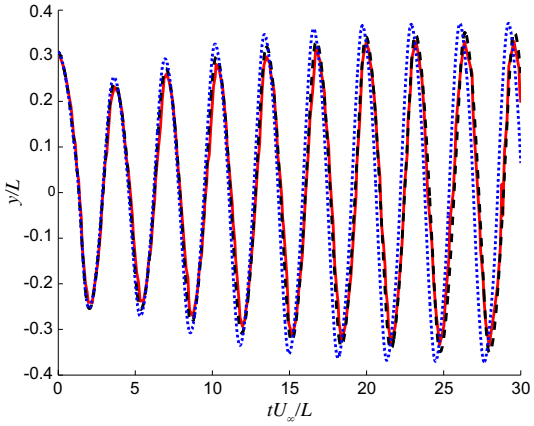

Figure 5.7: Free end position of a uniform flow past linked plates. Case 1, blue dotted; case 2, black dashed; Huang et al. (2007) [54], red solid.

5.1.3 Linked plates

This problem, like the previous one, consists of linked two-dimensional rigid bodies. However, in this case the bodies are flat plates of infinitesimal thickness with no gap between them, and the system is pinned at one end and placed in a uniform free stream U_∞ in order to simulate a self-excited flapping flag, as depicted in Fig. 5.6. In some cases, gravity acts in the direction of the free stream. A comparable study, based on a finite difference discretization of the continuously deformable structure, was carried out by Huang et al. [54]. Here, the distributed bending stiffness is represented by torsion springs in the hinges. It can be shown that the dynamical equation for linked rigid plates converges to the non-linear Euler–Bernoulli beam equation—the governing equation for the continuously deformable system—in the limit of vanishing plate length (but fixed overall length).

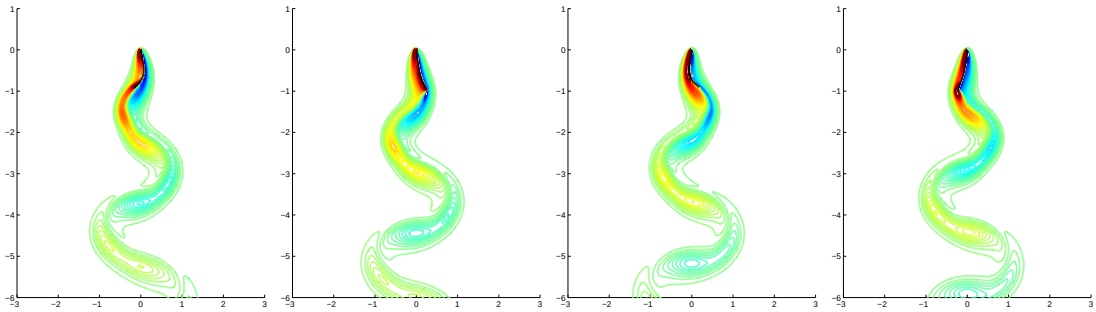

(a) $tU_\infty/L = 9.2$ (b) $tU_\infty/L = 10.0$ (c) $tU_\infty/L = 10.8$ (d) $tU_\infty/L = 11.6$

Figure 5.8: Instantaneous vorticity contours of a uniform flow past linked plates for case 2 at four instants.

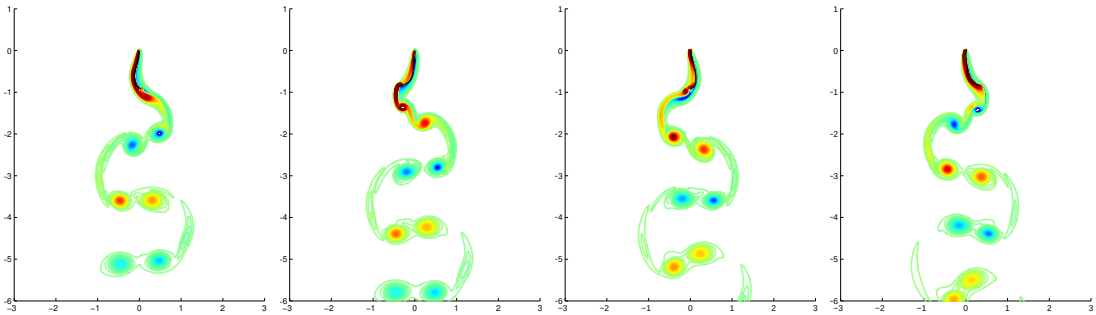

(a) $tU_\infty/L = 10.0$ (b) $tU_\infty/L = 10.75$ (c) $tU_\infty/L = 11.5$ (d) $tU_\infty/L = 12.25$

Figure 5.9: Instantaneous vorticity contours of a uniform flow past linked plates for case 3 at four instants.

A similar model has been used by other researchers, for example, in the leaflet heart valve model of Vierendeels et al. [121]. The inviscid continuously-deformable model has been studied by Alben & Shelley [1] and Michelin & Llewelyn Smith [80].

In the present study, the system is of fixed length L and composed of N plates of common length $l = L/N$. Each constituent plate has a mass per unit area denoted by ρ_b', and the plates are connected with torsion springs of uniform stiffness k. In order to reconcile the rigid-body system with the continuously-deformable analog, this spring stiffness is chosen to be

$$k = \frac{N}{L}\eta, \tag{5.8}$$

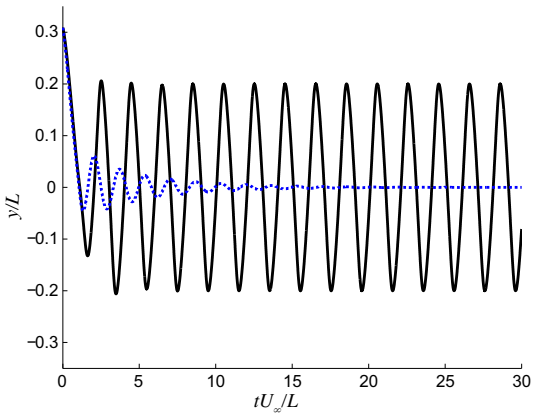

Figure 5.10: Free end position of a uniform flow past linked plates. Case 4, black solid; case 5, blue dotted.

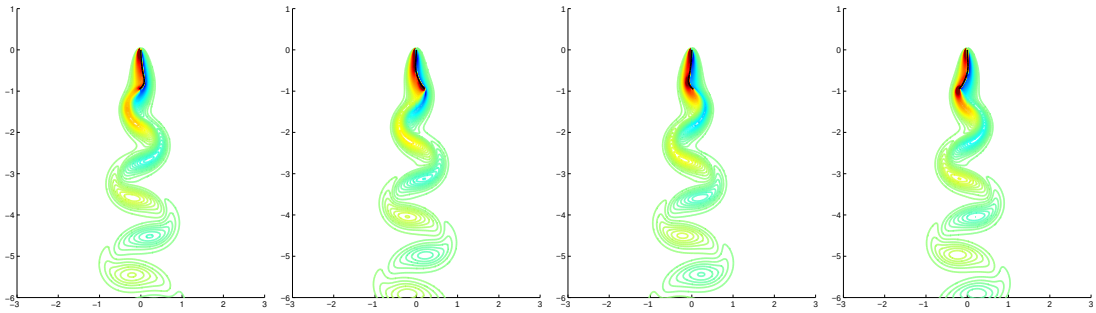

(a) $tU_\infty/L = 10.0$ (b) $tU_\infty/L = 10.5$ (c) $tU_\infty/L = 11.0$ (d) $tU_\infty/L = 11.5$

Figure 5.11: Instantaneous vorticity contours of a uniform flow past linked plates for case 4 at four instants.

where η is the uniform bending stiffness. The relative importance of gravity is given by gL/U_∞^2 (the inverse square of the Froude number). The physical parameters for each case are reported in Table 5.4. The parameters of cases 1–3 are chosen to compare with those reported by Huang et al. [54]: the first two cases assess the effect of the number of plates on a single set of physical conditions, and the third case consists of much smaller bending stiffness and larger Reynolds number. The remaining two cases, with fewer bodies, involve an exploration of the performance of lighter structures with negligible bending stiffness and gravity.

For all cases, the size of the four levels of computational domain, from coarsest to finest, are $[-6.4, 6.4] \times [-12.8, 3.2]$, $[-3.2, 3.2] \times [-6.4, 1.6]$, $[-1.6, 1.6] \times$

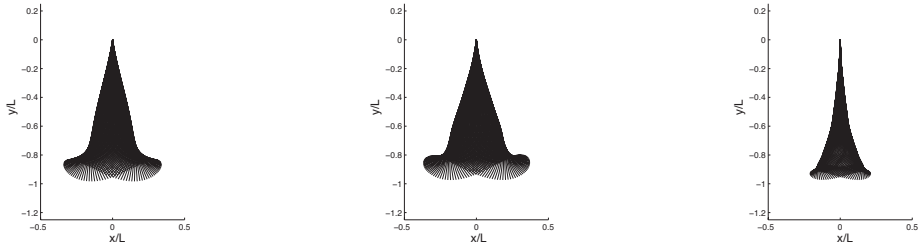

(a) case 2 (b) case 3 (c) case 4

Figure 5.12: The comparison of flapping modes for different cases

$[-3.2, 0.8]$ and $[-0.8, 0.8] \times [-1.6, 0.4]$, each scaled by L. For the $Re = 200$ cases, the finest grid spacing and time step size are chosen to be $\Delta x/L = 0.004$ and $\Delta t U_\infty/L = 0.0025$, respectively; for the $Re = 1000$ case, these parameters are set to $\Delta x/L = 0.002$ and $\Delta t U_\infty/L = 0.0005$.

Figure 5.7 presents a comparison with the numerical results from [54] of the lateral position of the free end resulting from the self-excited flapping of cases 1 and 2. As the number of plates increases from 10 to 50, the results from the simplified model become closer to the full model applied by Huang et al. The wake structures of the self-sustained flapping state are clearly depicted in four snapshots of vorticity contours in Fig. 5.8; these are similar to those reported in the previous work.

For the higher Reynolds number and lower stiffness case, i.e. case 3, Fig. 5.9 presents the vorticity contours in the wake at different instants. The vortex structures are more compact, as expected, and the number of vortices of one sign shed in each period is increased to two. Although the trend of the number of small vortices matches that reported in [54], the vorticity field and deformation of the structure visually differ from these previous results. The results of Huang et al. show larger deformation, with regions of high curvature that are largely absent from the current results; as a result of the more complex motion, more vortices are shed from the system in [54], with a wider range of strength and size. There are two possible reasons for these differences. The first one is associated

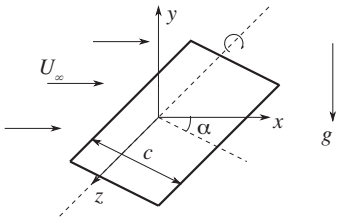

Figure 5.13: Sketch of the finite aspect ratio pivoting plate.

with the limited number of plates employed in the current study, which would tend to suppress the appearance of higher modes in the linked system. Another possible reason is that the fluid and structure are only weakly coupled in [54]; this treatment may cause the total energy in the system to increase nonphysically. As a result of the more energetic body motion, more flow structures are excited.

Two cases with lighter plates, cases 4 and 5, are also investigated. For these cases, the gravitational force is omitted and the bending stiffness is set to zero. Fig. 5.10 depicts the motion of the free end for these cases. For case 4, the flapping is self-sustained, as in the previous cases, and periodic vortex shedding is observed in Fig. 5.11. In contrast, the self-sustained flapping state cannot be preserved in the lighter structure in case 5. The flapping quickly decays in only a few oscillations and the linked plates finally settle down to equilibrium, aligned with the flow direction. This observation is consistent with the results reported by Zhu & Peskin [135] and Sawada & Hisada [102].

A comparison of the flapping pattern for different cases is presented in Fig. 5.12. The flapping magnitude increases with plate density and Reynolds number. The large bend in the envelope near the free end of the linked plates is observed for plates heavier than the fluid.

5.1.4 Passive pivoting of a plate of finite aspect ratio

In this section, we investigate a flat plate of finite aspect ratio allowed to freely rotate on an axis, subjected to gravity and a uniform free stream, as depicted in

Aspect Ratio	Domain size/c (largest)	$\Delta x/c$ (finest)	$\Delta t U_\infty/c$
0.5	$[-3.2, 12.8] \times [-9.6, 6.4] \times [-6.4, 6.4]$	0.025	0.005
1	$[-3.2, 12.8] \times [-9.6, 6.4] \times [-8, 8]$	0.025	0.005
2	$[-3.2, 12.8] \times [-9.6, 6.4] \times [-9.6, 9.6]$	0.025	0.005
4	$[-3.2, 12.8] \times [-9.6, 6.4] \times [-19.2, 19.2]$	0.025	0.005
∞ (2D)	$[-3.2, 12.8] \times [-9.6, 6.4]$	0.0125	0.0025

Table 5.5: Numerical parameters for different cases of passively pivoting plate.

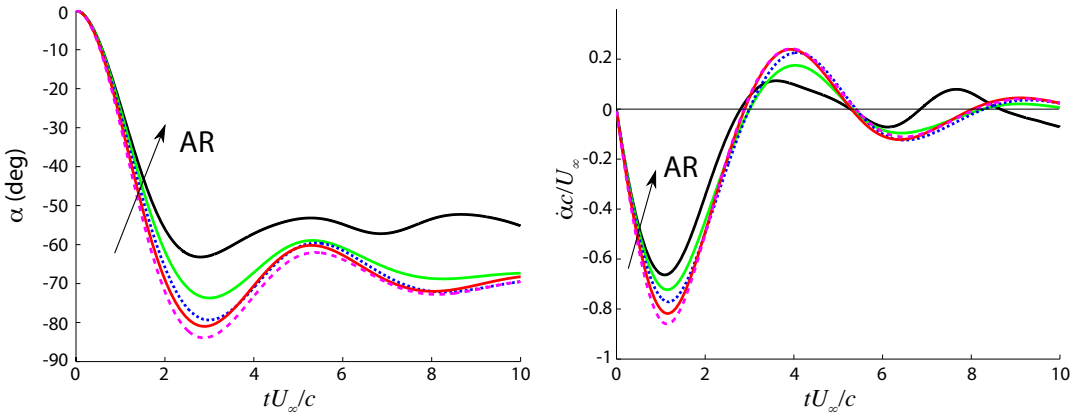

Figure 5.14: The angle (left) and angular velocity (right) of passively pivoting plates of different aspect ratio. $AR = 0.5$, magenta dashed; $AR = 1$, red solid; $AR = 2$, blue dotted; $AR = 4$, green solid; $AR = \infty$ (2D case), black solid.

Fig. 5.13. The infinitely-thin plate has mass per unit area ρ_b' and a rectangular planform with chord length c and span b; the aspect ratio, $AR = b/c$, will be varied in the study. The axis of rotation lies in the plane of the plate, parallel to the leading edge and passing through a point $0.1c$ aft of this edge. The directions of the free stream U_∞, gravitational force g, and the axis of rotation are mutually perpendicular. Initially, the plate is placed horizontally, parallel to the free stream, and gravity induces it to rotate about its axis.

Numerical simulations are performed for three-dimensional plates with different aspect ratio, $AR = 0.5, 1, 2, 4$. A two-dimensional case (nominally $AR = \infty$) is conducted for reference. For all simulations, the density ratio is $\rho_b'/(\rho_f c) = 2$, the Reynolds number based on free stream and chord length is fixed at $Re = 100$ and the gravitational parameter, gc/U_∞^2, is set to 1. The numerical parameters

(a) $tU_\infty/c = 2$ (b) $tU_\infty/c = 3$

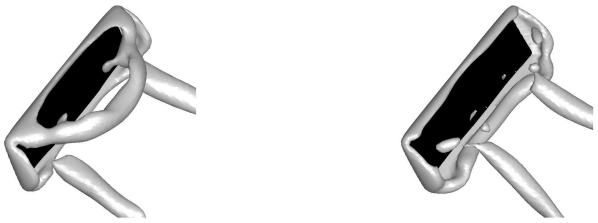

(c) $tU_\infty/c = 4$ (d) $tU_\infty/c = 5.5$

(e) $tU_\infty/c = 7$ (f) $tU_\infty/c = 8.5$

Figure 5.15: Top view of vortical structure behind a passively pivoting plate of $AR = 4$, represented by an isosurface $\lambda_2 = -4$ at different times.

for different cases are reported in Table 5.5. For all cases, four levels of computational domain are used in the simulation, of which the largest size is reported in the table. The extent of each subsequent domain is half that of the next-coarser domain in every dimension; for example, in 2D cases, the three finer domains have size $[-1.6, 6.4] \times [-4.8, 3.2]$, $[-0.8, 3.2] \times [-2.4, 1.6]$ and $[-0.4, 1.6] \times [-1.2, 0.8]$.

The resulting angles and angular velocities of the pivoting plates of different aspect ratio are shown in Fig. 5.14. Note that the angle, α, is positive for counterclockwise rotation about the z axis, as described in Fig. 5.13. For all cases,

the plate quickly pitches upward due to the dominant influence of gravity on the aft portion of the plate. With increasing aspect ratio, the rotation of the plate is more confined and the maximum angular excursion is smaller. All of the finite aspect ratio cases behave similarly, oscillating with decreasing amplitude about a fixed angle that is nearly identical for all aspect ratios. The two-dimensional case, in contrast, undergoes oscillations about a much shallower angle.

Snapshots of the vortex structures of the $AR = 4$ case are presented in Fig. 5.15, visualized with the λ_2 criterion [56]. When the plate starts rotating, vortices are generated at the leading edge and the tips. Then, as the plate adopts a large angle of attack to the free stream, the leading-edge vortex forms an arched structure that sheds from the plate. The tip vortices form two long parallel vortex tube in the wake and move inboard toward the central plane of the plate. At $tU_\infty/c = 5.5$, a clear view of the trailing edge vortex is obtained. Due to the effect of the tip vortices, the trailing edge vortex is compressed and deformed toward the central plane of the plate; this vortex, in turn, deforms the tip vortex structures. A new leading edge vortex begins to emerge at $tU_\infty/c = 7$, which subsequently grows and deforms, and is partly visualized at $tU_\infty/c = 8.5$. These snapshots elucidate the complex vortex shedding sequence that emerges from the finite aspect ratio plates. Clearly the three-dimensional structure of the wake follows a much different pattern, even at the relatively large aspect ratio of 4, compared with the two-dimensional case, which explains the significant difference in the plate dynamics.

5.2 Summary

In this work, a strong coupling algorithm has been presented for simulating interactions between incompressible fluids and rigid-body systems. The method employs Lagrange multipliers to unify the treatment of constraints in the prob-

lem, in the incompressibility of the fluid, the linkages in the structure, and the kinematic conditions at the interface. Null-space methods are used to project the fluid and system equations, so that the overall method represents an extension of the immersed boundary projection method of Colonius and Taira. The coupled equations are iteratively advanced to convergence. This convergence has been accelerated by relaxing the interface force, using a relaxation parameter computed from a simple estimate of the virtual fluid inertia in the fluid-body interaction. Several numerical examples, including a falling cylinder and flapping flexible wing, have been conducted to verify the coupling scheme. Good agreement has been achieved with the results from previous studies. The potential of a rigid-body system for capturing the dynamics of complex structures has shown in the self-excited oscillations of linked rigid plates. The three-dimensional capabilities of the numerical method have been demonstrated by the simulation of a passive pivoting of a finite aspect ratio plate in a uniform flow.

The relaxation scheme is a key element of the method presented here. The use of interface force, rather than the typical choice—kinematics—in the relaxation enables a natural identification (and exploitation) of the role of inertial reaction from the fluid. This leads to a rapidly convergent algorithm for a variety of mass ratios. It is stressed that, because of the partitioned treatment of the fluid and structure, the coupling method proposed here is independent of the choice of solvers for those components, and indeed, should be adaptable to interactions of fluids with fully elastic structures undergoing large deformation.

CHAPTER 6

Self-propelled motion of flexible flapping tail

6.1 Introduction

The flapping of a tail is a common mechanism for various swimming creatures, like dolphins and whales, to propel themselves. Some reviews on this topic have been conducted by Fish et al. [39, 42]. Two main aspects have been identified and studied for this mechanism. The first is the flapping pattern of the tail, for example the amplitude, frequency and angle of attack of the tail. Many researchers and engineers have put efforts to find the optimum combination of these parameters. Triantafyllou et al. [117, 115, 116] explored the parameters on the oscillating foils for the efficiency and thrust. The experiments conducted with real swimming animals are also presented by Fish et. al. [40, 41]. The second aspect relates to the properties of the tail, especially the tip area also known as fluke. Rather than actively controlled, the fluke responds passively to the incoming flow and bends accordingly. Few researches are conducted in this area due to the lack of the physical properties of the fluke and the difficulties in simulation of the dynamical interaction between the fluid and structure. Some efforts on determining the fluke properties have been conducted by Fish et al. [42], in which they measured the bending and camber change due to passive loads.

In this work, a numerical study of a flexible flapping tail is performed. Instead of fully simulating the tail motion of a real dolphin or whale at high Reynolds number, our focus is on the role of the flexibility of the tail at low Reynolds

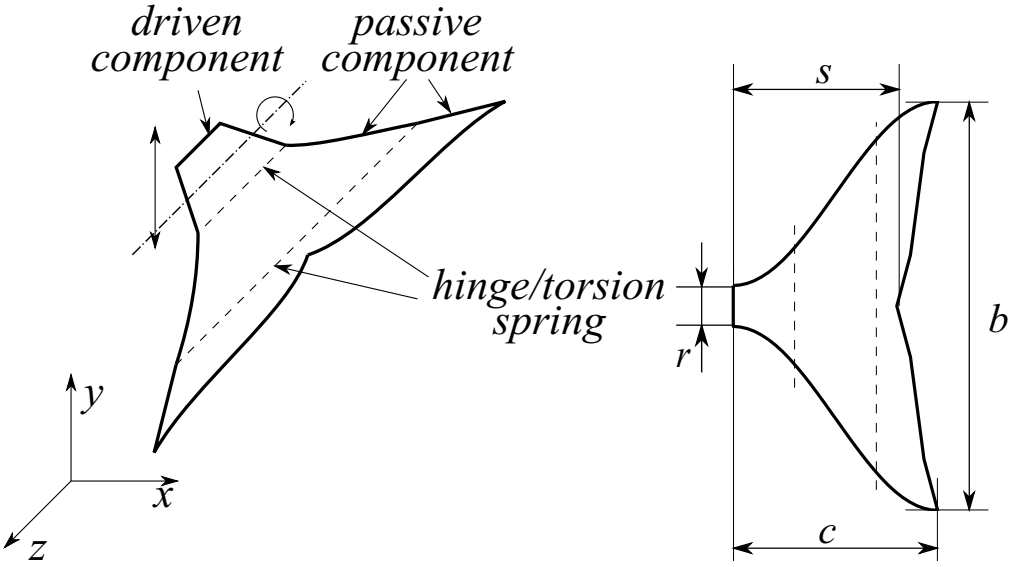

(a) Sketch of the flapping tail (b) Detailed shape of the tail

Figure 6.1: Sketch of the flexible tail.

number flow.

6.2 Problem Statement

The sketch of the model and the shape of the flexible tail are shown in Fig. 6.1. In this problem, we are looking at the self-propulsive speed and efficiency induced by the flapping of the tail. The flexible tail is formed by three components with one driven part and two passive parts. They are connected with torsion spring, whose stiffness is an important parameter in our research.

The shape of the tail is described by some simple primary functions. The upper part of the leading trailing edge can be described as

$$y_l = \frac{1}{2}r + \frac{1}{2}\left(b - \frac{r}{2}\right)\left[1 + \sin\left(\frac{\pi x}{c} - \frac{\pi}{2}\right)\right], x \in [0, c] \tag{6.1}$$

$$y_t = \frac{1}{2}b + \left[1 + \sin\left(\frac{x-s}{c-s}\pi - \frac{\pi}{2}\right)\right], x \in [s, c] \tag{6.2}$$

where all notations can be found in Fig. 6.1(b). The aspect ratio of the tail is

defined as $AR = b/c$. The root width is indicated as r and s is the chord length at the center. In this work, we focus on the tail with $AR = 2$, $r = 0.2c$ and $s = 0.8c$.

The hinges that connect the different parts are aligned in z direction. The chord length of driven component is $0.3c$; and the two passive component lengths are $0.4c$ for the center one and $0.3c$ for the other.

The driven component oscillates vertically and rotate around its centroid about z axis. Its kinematics can be described mathematically as follows, which is similar to those in the previous flapping wing case.

$$X_1(t) = 0 \tag{6.3}$$

$$Y_1(t) = \frac{A_0}{2}\frac{G_t(ft)}{\max G_t}C(ft) \tag{6.4}$$

$$\alpha_1(t) = -\beta\frac{G_r(ft)}{\max G_r}C(ft) \tag{6.5}$$

where A_0 is the translation amplitude, f is the cyclic frequency, the translational shape function is

$$G_t(t) = \int_t \tanh[\sigma_t \cos(2\pi t')]\,\mathrm{d}t' \tag{6.6}$$

and the rotational shape function is

$$G_r(t) = \tanh[\sigma_r \cos(2\pi t + \Phi)], \tag{6.7}$$

where Φ is the phase lead of rotation. The impulsive motion is avoided with a start-up conditioner given by

$$C(t) = \frac{\tanh(8t-2) + \tanh 2}{1 + \tanh 2}. \tag{6.8}$$

In the current study, the fixed kinematics parameters are list in Table 6.1

β	$\pi/6$
σ_t	0.628
σ_r	0.628
Φ	0
f	0.1

Table 6.1: Fixed kinematic parameters.

The dimensionless spring stiffness and damping coefficients are defined as $K = K^*/(\rho_f f^2 c^4)$ and $R = R^*/(\rho_f f c^4)$, respectively, where the $()^*$ denotes a dimensional value. In the current study, those values are arbitrarily chosen as we do not have comparable experimental data. For different cases, the spring stiffness varies and damping coefficient is fixed at $R = 1.0$

6.3 Methods

One important feature of our model is the ability to compute the propulsive velocity according the force generated from tail flapping and change the surrounding flow speed accordingly. To achieve this goal, a virtual bluff body is included to attach with the tail. To be virtual, this bluff body does *not* present in the flow simulation, which ignores the flow feature from flow past a bluff body and keeps the computation fairly simple. However, the mass and its drag are taken into account when propulsive velocity is calculated. In the current study, we treat the virtual body as an ellipsoid with three semi-principal axes to be $5c$,c and c and the longest axes aligned with x direction. M_body is denoted as the virtual body mass. The computation of the drag F_D follows the formula used in [39] as

$$F_D = \frac{1}{2}\rho_f C_D S_w U^2 \tag{6.9}$$

where ρ_f is the fluid density, S_w is the wetted surface area and U is the propulsive velocity. The drag coefficient C_D is expressed differently according to the flow

status.

$$C_D = 1.33Re^{-0.5}, (laminar) \tag{6.10}$$

$$C_D = 0.072Re^{-0.2}, (turbulence) \tag{6.11}$$

For all of our cases, the laminar flow coefficient is chosen.

The self-propulsive speed U can be calculated by following differential equation

$$(M_{body} + M_{add})\dot{U} = F_t + F_D \tag{6.12}$$

where F_t is the fluid force generated by the tail and M_{add} is the added mass of ellipsoid. It can be calculated as

$$M_{add} = K\frac{4}{3}\pi\rho_f ab^2 \tag{6.13}$$

For our cases, $K = 0.095$ and a,b are $5c$ and c, respectively.

Currently, $M_{body} + M_{add}$ is set to be 5.24, which is also somewhat arbitrary. However, it is worth mentioning that the mass value here does not affect the final averaged self-propulsive speed when $\dot{U}$ is zero.

There are multiple ways to define the Reynolds number in this study. To start the simulation, a flapping Reynolds number is considered as

$$Re_f = \frac{2A_0 fc}{\nu}. \tag{6.14}$$

Another important Reynolds number can be achieved when final averaged self-propulsive speed $\overline{U_e}$ is obtained. It is defined as

$$Re = \frac{\overline{U_e}L}{\nu} \tag{6.15}$$

where L is the total length of the virtual bluff body and tail chord. This Reynolds number definition is commonly seen in other literatures as well, and therefore can be compared with them directly.

As for the forces generated by the flapping tail, F_t, it is solved by the high-fidelity numerical methods described in the previous two chapters. For all simulation, the size of largest computational domain is $[-3.2, 12.8] \times [-8.0, 8.0] \times [-9.6, 9.6]$ and total four levels of computational domain are applied. The extent of each subsequent domain is half that of the next-coarser domain in every dimension. The finest grid resolution is $\Delta x = 0.025$ and time resolution is $\Delta t = 0.005$.

6.4 Results

The main parameter investigated here is the hinge stiffness, which directly defines the flexibility of the tail. Other parameters include the amplitude of the flapping and flapping Reynolds number. For the current study, they are listed in Table 6.2

Case No.	A_0/c	Re_f	K
1	1.0	20	25
2	1.0	20	50
3	1.0	20	75
4	1.0	20	100
5	1.0	20	200
6	1.0	20	800
7	1.0	10	∞

Table 6.2: Kinematic parameters for flexible flapping wing study.

The self-propulsive speeds are plotted in Fig. 6.2. It is noticed that no thrust is gained for Case 1, in which a very flexible wing is applied. With the increase of the torsion stiffness, the average propulsive speed increases. However, after reaching some critical torsion coefficient, the average velocity of self-propulsion stop increasing, which implies the existence of the optimal torsion stiffness. The

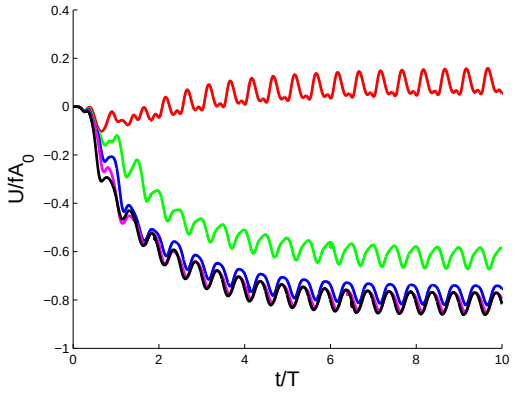

Figure 6.2: The self-propulsive speed generated by tails with different spring coefficients. Case 1: red, Case 2: green, Case 3: blue, Case 4: magenta, Case 5: black.

demonstration of the deflection angles at two hinges are presented in Fig. 6.3. The maximum amplitude of the deflection angles becomes smaller with the increase of the torsion stiffness. It is also noticed that the deflection angles less than 10° do not play a big role in the generation of self-propulsive speed.

Another important parameter we are investigating is the efficiency, which is defined as

$$\eta = \frac{TV}{E} \tag{6.16}$$

where T is the thrust and V is the propulsive velocity. Both of them are time averaged. E represents the average input power (lift force times heave velocity, plus pitching moment times pitch angular velocity; averaged over a period). Table 6.3 lists the efficiency of different cases, and the Reynolds number is also presented there. Overall, the value is very small due to the viscous effect at the low Reynolds number flow regime.

The flow structure behind the tail of Case. 2 is presented in Fig. 6.4, illustrated by the isosurface of the λ_2 criteria. It is clear that the flexible tail is bended due to the flapping motion. The wake structure dissipates very fast in this case because

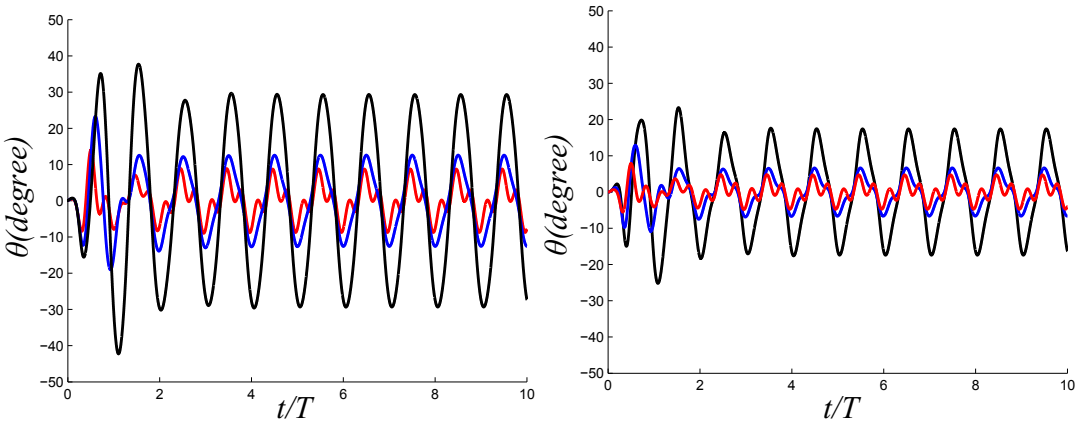

(a) Hinge 1 (b) Hinge 2

Figure 6.3: The defection angles at two hinges for different spring coefficients. K=50, black; K=100, blue; K=200 red.

Case No.	self-propulsive speed $\overline{U}/fA_0$	efficiency η	Reynolds number Re
1	-0.094	0.0158%	21
2	0.621	1.43%	137
3	0.773	2.66%	170
4	0.805	2.97%	177
5	0.813	3.00%	179
6	0.808	3.00%	178
7	0.698	1.22%	77

Table 6.3: The efficiency and flow Reynolds number for different cases

of the high viscosity.

6.5 Summary

In this chapter, the flapping mechanism of flexible tail section is investigated in the low Reynolds region, i.e. $Re \sim O(10^2)$. A self-propelled swimming model is applied to compute the swimming speed induced by the flapping. It is found that the swimming speed is related to the flexibility of the tail. With the growth of the stiffness, the average self-propulsive speed increases and reaches a maximum. The efficiency of the flapping mechanism is not high considering that the research is conducted in a low Reynolds number flow region. A optimal flexibility of the

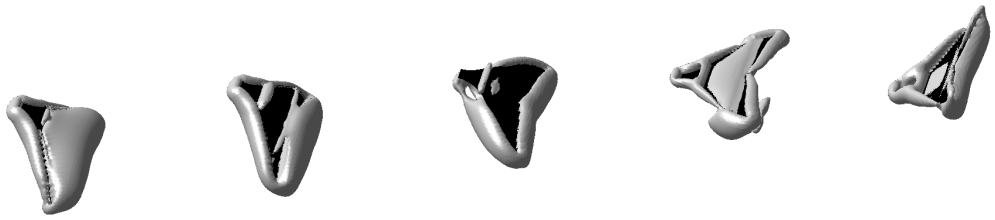

(a) $t/T = 9.0$ (b) $t/T = 9.1$ (c) $t/T = 9.2$ (d) $t/T = 9.3$ (e) $t/T = 9.4$

(f) $t/T = 9.5$ (g) $t/T = 9.6$ (h) $t/T = 9.7$ (i) $t/T = 9.8$ (j) $t/T = 9.9$

Figure 6.4: Top view of vortical structure behind a flexible tail of case 2, represented by an isosurface $\lambda_2 = -4$ at different times.

tail can be obtained by evaluating the flow efficiency.

CHAPTER 7

Conclusions and Future Extensions

7.1 Conclusions

In this work, various numerical methods are developed and investigated to explore the unsteady fluid dynamics at low to moderate Reynolds number.

In the first part, a low-order model has been developed by tracking only small number of discrete vortices with time-varying strength to account for the unsteady aerodynamics. Two sets of governing equations of the vortices motion are employed. One is the classical Brown-Michael equation, and the other one follows the impulse matching principle. The model is shown to predict forces on a two-dimensional pitching or perching plate in reasonably good agreement with corresponding experiments and high-fidelity simulations, particularly at high pitch rates. The agreement is notable, considering that fewer than 10^0 of freedom - compared to $10^5 - 10^6$ for a well-resolved high-fidelity simulation at Reynolds number 1,000 - are need to achieve it.

In the second part, a strong coupling algorithm has been presented for simulating interactions between incompressible fluids and rigid-body systems. The method employs Lagrange multipliers to unify the treatment of constraints in the problem, in the incompressibility of the fluid, the linkages in the structure, and the kinematic conditions at the interface. Null-space methods are used to project the fluid and system equations, so that the overall method represents an extension of the immersed boundary projection method of Colonius and Taira. The coupled

equations are iteratively advanced to convergence. This convergence has been accelerated by relaxing the interface force, using a relaxation parameter computed from a simple estimate of the virtual fluid inertia in the fluid-body interaction. Several numerical examples, including a falling cylinder and flapping flexible wing, have been conducted to verify the coupling scheme. Good agreement has been achieved with the results from previous studies. The potential of a rigid-body system for capturing the dynamics of complex structures has shown in the self-excited oscillations of linked rigid plates. The three-dimensional capabilities of the numerical method have been demonstrated by the simulation of a passive pivoting of a finite aspect ratio plate in a uniform flow. It is stressed that, because of the partitioned treatment of the fluid and structure, the coupling method proposed here is independent of the choice of solvers for those components, and indeed, should be adaptable to interactions of fluids with fully elastic structures undergoing large deformation.

7.2 Future Extensions of the Research

7.2.1 Low-order modeling

First, it is natural to consider how the model can be made more accurate. The model, as constructed, can be thought of as a combination of four basic components: (1) shed vorticity is represented as isolated point vortex singularities; (2) vortex strengths are determined by some constraint; (3) each vortex singularity moves according to an evolution equation; (4) a vortex is 'shed' (and a new vortex released) by a criterion on its strength. It is important to note that any of these four components can be altered with little change in the other three. For example, in this work we have modified the evolution equation of component (3), but left the other components unchanged. We have seen that this has improved the accuracy of the model.

The accuracy of the model might also be improved by reconsideration of components (1) and (2). For example, the Kutta condition has been used to determine the strengths of the developing point vortices. However, one might replace this condition by determining the strengths empirically, e.g. from high-fidelity computations or experiment. In this way, the model becomes a framework for *model reduction*, with an attractive phenomenological foundation. In ongoing work, we are exploring the use of techniques from optimal control and estimation theory in order to determine the vortex circulation (or its rate of change) that best matches the forces on the plate computed from high-fidelity simulations. One might also improve the accuracy of the model by augmenting component (1) with higher-order singularities. Each new singularity would require corresponding conditions to determine its strength; these conditions might be generated from the aforementioned empirical reduction, for example to determine the coefficients of a multipole expansion about the moving singular points.

In this work, we have only demonstrated the model on the development of the leading-edge vortex, and one generally desires capabilities for the model beyond improved accuracy of this start-up behavior. If, for example, we insist on comparable fidelity of the model when the wing is fixed at high angle of attack for longer duration, then we would expect the model to capture the bifurcation to sustained vortex shedding [15]. It is not yet clear whether the model, in its present form, can admit similar dynamical behavior; for example, the model was not able to predict the bifurcation from closed to open separation bubble in the case of fixed angle of 45 degrees. Undoubtedly, such behavior is highly dependent on the choice of shedding criterion (component (4) above). As mentioned earlier in this paper, one might instead use a criterion based on formation number [81], or adapt techniques from dynamical systems theory [65].

Other problems of interest for biologically-inspired MAVs require consideration of flapping-wing aerodynamics, and in particular, continuous encounters of a

wing with its previously-shed vorticity. As these encounters generally involve interactions between a vortex and the attached boundary layer of the wing [126, 34], they may not be well captured in a purely inviscid calculation [80]. It is also important to note that, for motions in which the flow remains attached at the leading edge, it is preferable to apply a suction pressure in lieu of a vortex released from that edge. In order to distinguish such cases, one might rely on the criterion recently proposed in [93], in which separation is deemed to occur when this suction pressure exceeds critical bounds that are determined empirically. Note that the Polhamus leading-edge suction analogy is essentially based on this principle [89].

Finally, and crucially, the model must be extended to finite aspect ratio wings for it to be of general use for MAV flight architectures. A natural approach to this extension is via a lifting-line theory, in which the local angle of attack of each wing section is modified by induced velocity from streamwise line vortices supposed to extend from the bound vorticity to the shed vortices. Models for unsteady aerodynamic response in this form have been developed by, for example, Jones [59], and built upon by Dore [30]. In this extension to three-dimensional flows, care must be taken to preserve the simplicity of the model.

7.2.2 High-fidelity simulation

The basic platform for the high-fidelity simulation of fluid-structure interaction has been constructed. The improvements can be performed in several following aspects.

Firstly, the Poisson solver can be further tuned up, especially in a massive parallelized environment. The speed of an incompressible Navier-Stokes solver is largely depends on the performance of the core Poisson solver. In the current work, the Poisson equations are solved by HYPRE library, which uses the multigrid methods and is suitable for large scale parallel computing. However, the

real performance of the solver in our application is largely downgraded when the number of processors exceeds 256. One possible solution is to covert our Poisson solver to a FFT-based one, like [29], which is naturally parallelized and do not require any iteration.

The relaxation scheme is a key element of the method presented here. The use of interface force, rather than the typical choice—kinematics—in the relaxation enables a natural identification (and exploitation) of the role of inertial reaction from the fluid. This leads to a rapidly convergent algorithm for a variety of mass ratios. This idea can be further explored and extended to the problems on the interactions between fluid and elastic materials.

References

[1] S. Alben and M. J. Shelley. Flapping states of a flag in an inviscid fluid: Bistability and the transition to chaos. *Phys. Rev. Lett.*, 100:074301, 2008.

[2] C. R. Anderson, Y. C. Chen, and J. S. Gibson. Control and identification of vortex wakes. *J. Dyn. Sys., Meas., Control*, 122:298–306, 2000.

[3] S. A. Ansari, R. Zbikowski, and K. Knowles. Non-linear unsteady aerodynamic model for insect-like flapping wings in the hover. part 1: methodology and analysis. *Proc. IMechE PartG: J. Aerospace Engineering*, 220:61–83, 2006.

[4] S. A. Ansari, R. Zbikowski, and K. Knowles. Non-linear unsteady aerodynamic model for insect-like flapping wings in the hover. part 2: implementation and validation. *Proc. IMechE PartG: J. Aerospace Engineering*, 220:169–186, 2006.

[5] E. Balaras. Modeling complex boundaries using an external force field on fixed cartesian grids in large-eddy simulations. *Computers & Fluids*, 33:375–404, 2004.

[6] L. Bennett. Clap and fling aerodynamics - an experimental evaluation. *J. Exp. Biol.*, 69:261–272, 1977.

[7] M. Benzi, G. H. Golub, and J. Liesen. Numerical solution of saddle point problems. *Acta Numerica*, 14:1–137, 2005.

[8] J. M. Brich and M. H. Dickinson. Spanwise flow and the attachment of the leading-edge vortex on insect wings. *Nature*, 412:729–733, 2001.

[9] C. E. Brown and W. H. Michael. Effect of leading-edge separation on the lift of a delta wing. *J. Aeronaut. Sci*, 21:690–694, 1954.

[10] S. L. Brunton and C. W. Rowley. Modeling the unsteady aerodynamic forces on small-scale wings. In *47th AIAA Aerospace Sciences Metting*, 2009-1127, 2009.

[11] S. L. Brunton and C. W. Rowley. Fast computation of finite-time lyapunov exponent fields for unsteady flows. *Chaos*, 20:017503, 2010.

[12] S. L. Brunton and C. W. Rowley. Unsteady aerodynamic models for algile flight at low reynolds numbers. In *48th AIAA Aerospace Sciences Meeting, Jan. 4-7, 2010*, 2010-552, 2010.

[13] B. M. Cardwell and K. Mohseni. Vortex shedding over a two-dimensional airfoil: where the particles come from. *AIAA J.*, 46:545–547, 2008.

[14] P. Causin, J. F. Gerbeau, and F. Nobile. Addapplications in the design of partitioned algorithms for fluid-structure problems. *Comput. Methods Appl. Mech. Engrg.*, 194:4506–4527, 2005.

[15] K. K. Chen, T. Colonius, and K. Taira. The leading-edge vortex and quasisteady vortex shedding on an accelerating plate. *Phys. Fluids*, 22:033601, 2010.

[16] R. R. Clements. An inviscid model of two-dimensional vortex shedding. *J. Fluid Mech.*, 57:321–336, 1973.

[17] M. Cloupeau, J. F. Devillers, and D. Devezeaux. Direct measurements of instantaneouslif in desert locust; comparison with jensen's experiments on detached wings. *J. Exp. Biol.*, 80:1–15, 1979.

[18] T. Colonius and K. Taira. A fast immersed boundary method using a nullspace approach and multi-domain far-field boundary conditions. *Comput. Methods Appl. Mech. Engrg.*, 197:2131–2146, 2008.

[19] R. J. Cooter and P. S. Baker. Weis-fogh clap and fling mechanism in *Lousta*. *Nature*, 269:53–54, 1977.

[20] L. Cortelezzi. On the unsteady separated flow past a semi-infinite plate. exact solution of the brown and michael model. *Phys. Fluids*, 7:526–529, 1995.

[21] L. Cortelezzi. Nonlinear feedback control of the wake past a plate with a suction point on the downstream wall. *J. Fluid Mech.*, 327:303–324, 1996.

[22] L. Cortelezzi, Y. C. Chen, and H. L. Chang. Nonlinear feedback control of the wake past a plate: from a low-order model to a higher-order model. *Phys. Fluids*, 9:2009–2022, 1997.

[23] L. Cortelezzi and A. Leonard. Point vortex model of the unsteady separated flow past a semi-infinite plate with transverse motion. *Fluid Dyn. Res.*, 11:263–295, 1993.

[24] L. Cortelezzi, A. Leonard, and J. Doyle. An example of active circulation control of the unsteady separated flow past a semi-infinite plate. *J. Fluid Mech.*, 260:127–154, 1994.

[25] J. Degroote. Partitioned simulation of fluid-strcture interaction. *Arch. Comput. Methods Eng.*, 20:185–238, 2013.

[26] J. Degroote, K.-J. Bathe, and J. Vierendeels. Performance of a new partitioned procedure versus a monolithic procedure in fluid-structure interaction. *Comput. Struct.*, 87:793–801, 2009.

[27] M. H. Dickinson and K. G. Götz. Unsteady aerodynamic performancd of model wings at low reynolds numbers. *J. Exp. Biol.*, 174:45–64, 1993.

[28] M. H. Dickinson, F.-O. Lehmann, and S. P. Sane. Wing rotation and the aerodynamic basis of insect flight. *Science*, 284:1954–1960, 1999.

[29] M. S. Dodd and A. Ferrante. A fast pressure-correction method for incompressible two-fluid flows. *J. Comput. Phys.*, 273:416–434, 2014.

[30] B. Dore. The unsteady forces on finite wings in transient motion. Technical report, Technical report 3456. Aeronautical Research Council, 1966.

[31] J. D. Eldredge. Numerical simulation of the fluid dynamics of 2d rigid body motion with the vortex particle method. *J. Comput. Phys.*, 221:626–648, 2007.

[32] J. D. Eldredge. Dynamically coupled fluid-body interactions in vorticity-based numerical simulations. *J. Comput. Phys.*, 227:9170–9194, 2008.

[33] J. D. Eldredge. A reconciliation of viscous and inviscid approaches to computing locomotion of deforming bodies. *Exper. Mech.*, 50:1349–1353, 2010.

[34] J. D. Eldredge, J. Tommey, and A. Medina. On the rrole of chord-wise flexibility in a flapping wing with hovering kinematics. *J. Fluid Mech.*, 659:94–115, 2010.

[35] J. D. Eldredge and C. Wang. Improved low-order modeling of a pitching and perching plate. In *41st AIAA Fluid Dynamics Conference, June 2011, Honolulu, HI*, AIAA 2011-3579, 2011.

[36] C. P. Ellington, C. van den Berg, A. P. Willmott, and A. L. R. Thomas. Leading-edge vortices in insect flight. *Nature*, 384:626–630, 1996.

[37] C. Farhat, M. Lesoinne, and N. Maman. Mixed explicit/implicit time integration of coupled aeroelastic problems: three-field formulation, geometric conservation and distributed solution. *Int. J. Numer. Meth. Fluids*, 21:807–835, 1995.

[38] R. Featherstone. *Rigid Body Dynamics Algorithms*. Springer, 2007.

[39] F. Fish and J. Rohr. Review of dolphin hydrodynamics and swimming performance. Technical report, SPAWAR Systems Center San Diego, 1999.

[40] F. E. Fish, S. Innes, and K. Ronald. Kinematics and estimated thrust production of swimming harp and riring seals. *J. Exp. Biol.*, 137:157–173, 1988.

[41] F. E. Fish, P. Legac, T. M. Williams, and T. Wei. Measurement of hydrodynamic force generation by swimming ddolphin using bubble dpiv. *J. Exp. Biol.*, 217:252–260, 2014.

[42] F. E. Fish, M. K. Nusbaum, J. T. Beneski, and D. R. Ketten. Passive cambering and flexible propulsors: cetasean flukes. *Bioinsp. Biomim.*, 1:S42–S48, 2006.

[43] C. Förster, W. A. Wall, and E. Ramm. Artifical added mass instabilities in sequential staggered coupling of nonlinear structures and incompressible viscous flows. *Comput. Methods Appl. Mech. Engrg.*, 196:1278–1293, 2007.

[44] C. Führer and B. J. Leimkuhler. Numerical solution of differential-algebraic equations for constrained mechanical motion. *Numer. Math.*, 59:55–69, 1991.

[45] R. Glowinski, T. W. Pan, T. I. Hesla, D. D. Joseph, and J. Pèriaux. A fictitious domain approach to the direct numerical simulation of incompressible viscous flow past moving rigid bodies: application to particulate flow. *J. Comput. Phys.*, 169:363–426, 2001.

[46] R. Glowinski, T. W. Pan, and J. Périaux. Distributed Lagrange multiplier methods for incompressible viscous flow around moving rigid bodies. *Comput. Methods Appl. Mech. Engrg.*, 151:181–194, 1998.

[47] K. Granlund, M. OL, D. Garmann, M. Visbal, and L. Bernal. Experiments and computations on abstractions of perching. In *28th AIAA Applied Aerodynamics Conference, 28 June-1 July 2010, Chicago, Illinois*, AIAA 2010-4943, 2010.

[48] K. Gustafson and R. Leben. Computation of dragonfly aerodynamics. *Comput. Phys. Commun.*, 65:121–132, 1991.

[49] E. Hairer, M. Roche, and C. Lubich. *The numerical solution of differential-algebraic systems by Runge-Kutta methods*. Springer-Verlag, 1989.

[50] E. Hairer and G. Wanner. *Solving ordinary differential equations II. Stiff and differential algebraic problems*. Springer, 1992.

[51] F. Hollick. The flight of the dipterous fly muscina stabulans fallén. *Phil. Trans. R. Soc. Lond. B*, 230:357–390, 1940.

[52] G. Hou, J. Wang, and A. Layton. Numerical methods for fluid-structure interaction – a review. *Commun. Comput. Phys.*, 12:337–377, 2012.

[53] M. S. Howe. Emendation of the brown & michael equation, with application to sound generation by vortex motion near a half-plane. *J. Fluid Mech.*, 329:89–101, 1996.

[54] W.-X. Huang, S. J. Shin, and H. J. Sung. Simulation of flexible filaments in a uniform flow by the immersed boundary method. *J. Comput. Phys.*, 226:2206–2228, 2007.

[55] M. Jensen. Biology and physics of locust flight. iii. the aerodynamics of locust flight. *Phil. Trans. R. Soc. Lond. B*, 239:511–552, 1956.

[56] J. Jeong and F. Hussain. On the identification of a vortex. *J. Fluid Mech.*, 285:69–94, 1995.

[57] M. A. Jones. The separated flow of an inviscid fluid around a moving flat plate. *J. Fluid Mech.*, 496:405–441, 2003.

[58] M. A. Jones and M. J. Shelley. Falling cards. *J. Fluid Mech.*, 540:393–425, 2005.

[59] R. Jones. The unsteady lift of a wing of finite aspect ratio. Technical report, Technical report 681, NACA, 1939.

[60] M. M. Joosten, W. G. Dettmer, and D. Perić. Analysis of the block Gauss-Seidel solution procedure for a strongly coupled model problem with reference to fluid-structure interaction. *Int. J. Numer. Meth. Engng*, 78:757–778, 2009.

[61] J. Katz. A discrete vortex method for the non-steady separated flow over an airfoil. *J. Fluid Mech.*, 102:315–328, 1981.

[62] M. Kiya and M. Arie. A contribution to an inviscid vortex-shedding model for an inclined flat plate in uniform flow. *J. Fluid Mech.*, 82:223–240, 1977.

[63] P. Koumoutsakos. Multiscale flow simulations using particles. *Annu. Rev. Fluid Mech.*, 37:457–487, 2005.

[64] P. Koumoutsakos, A. Leonard, and F. Pépin. Boundary conditions for viscous vortex methods. *J. Comput. Phys.*, 113:52–61, 1994.

[65] R. Krechetnikov, J. Marsden, and H. Nagib. A low-dimensional model of separation bubbles. *Phys. D*, 238:1152–1160, 2009.

[66] U. Küttler and W. A. Wall. Fixed-point fluid-structure interaction solvers with dynamic relaxation. *Comput. Mech.*, 43:61–72, 2008.

[67] M.-C. Lai and C. S. Peskin. An immersed boundary method with formal second-order accuracy and reduced numerical viscosity. *J. Comput. Phys.*, 160:705–719, 2000.

[68] D. Lentink and M. H. Dickinson. Biofluiddynamic scaling of flapping, spinning and translating fins and wings. *J. Exp. Biol.*, 212:2691–2704, 2009.

[69] D. Lentink and M. H. Dickinson. Rotational accelerations stabilize leading edge vortices on revolving fly wings. *J. Exp. Biol.*, 212:2706–2719, 2009.

[70] M. J. Lighthill. Introduction: Boundary layer theory. In L. Rosenhead, editor, *Laminar Boundary Layers*. Clarendon Press, 1961.

[71] M. J. Lighthill. On the weis-fogh mechanism of lift generation. *J. Fluid Mech.*, 60:1–17, 1973.

[72] D. Lipinski and K. Mohseni. Flow structures and fluid transport for the hydromedusae *Saria tubulosa* and *Aequorea victoria*. *J. Exp. Biol.*, 212:2439–2447, 2009.

[73] D. Lipinski and K. Mohseni. A ridge tracking algorithm and error extimate for efficient computation of lagrangian coherent structures. *Chaos*, 20:017504, 2010.

[74] C. Liu, X. Zheng, and C. Sung. Preconditioned multigrid methods for unsteady incompressible flows. *J. Comput. Phys.*, 139:35–57, 1998.

[75] H. Luo, R. Mittal, X. Zheng, S. A. Bielamowicz, R. J. Walsh, and J. K. Hahn. An immersed-boundary method for flow-structure interaction in biological systems with application to phonation. *J. Comput. Phys.*, 227:9303–9332, 2008.

[76] H. G. Matthies, R. Niekamp, and J. Steindorf. Algorithms for strong coupling procedures. *Comput. Methods Appl. Mech. Engrg.*, 195:2028–2049, 2006.

[77] H. G. Matthies and J. Steindorf. Partitioned but strongly coupled iteration schemes for nonlinear fluid-structure interaction. *Comput. Struct.*, 80:1991–1999, 2002.

[78] T. Maxworthy. Experiments on the wei-fogh mechanism of lift generation by insects in hovering flight. part 1. dynamics of the 'fling'. *J. Fluid Mech.*, 93:47–63, 1979.

[79] S. Michelin and S. G. L. Smith. An unsteady point vortex method for coupled fluid-solid problems. *Theor. Comput. Fluid Dyn.*, 23:127–153, 2009.

[80] S. Michelin and S. G. L. Smith. Falling cards and flappping flags: understanding fluid-solid interactions using and unsteady point vortex model. *Theor. Comput. Fluid Dyn.*, 24:195–200, 2010.

[81] M. Milano and M. Gharib. Uncovering the physics of flapping flat plates with artificial evolution. *J. Fluid Mech.*, 534:403–409, 2005.

[82] L. A. Miller and C. S. Peskin. A computational fluid dydnamics of 'clap and fling' in the smallest insects. *J. Exp. Biol.*, 208:195–212, 2005.

[83] F. O. Minotti. Unsteady two-dimentional theory of a flapping wing. *Physical Review E: Statistical, Nonlinear, and Soft Matter Physics*, 66:051907, 2002.

[84] R. Mittal, H. Dong, M. Bozkurttas, F. M. Najjar, A. Vargas, and A. von Lobbecke. A versatile sharp interface immersed boundary method for incompressible flows with complex boundaries. *J. Comput. Phys.*, 227:4825–4852, 2008.

[85] R. Mittal and G. Iaccarino. Immersed boundary methods. *Annu. Rev. Fluid Mech.*, 37:239–261, 2005.

[86] S. Nair and E. Kanso. Hydrodynamically coupled rigid bodies. *J. Fluid Mech.*, 592:393–411, 2007.

[87] C. S. Peskin. Flow patterns around heart valves: a numerical method. *J. Comput. Phys.*, 10:252–271, 1972.

[88] C. S. Peskin. Numerical analysis of blood flow in the heart. *J. Comput. Phys.*, 25:220–252, 1977.

[89] E. Polhamus. A concept of the vortex lift of sharp-edge delta wings based on a leading-edge-suction analogy. Technical report, Technical report TN D-3767, NASA, 1966.

[90] B. Protas. Vortex dynamics models in flow control problems. *Nonlinearity*, 21:203–250, 2008.

[91] D. I. Pullin and Z. J. Wang. Unsteady forces on an accelerating plate and application to hovering insect flight. *J. Fluid Mech.*, 509:1–21, 2004.

[92] R. Ramamurti and W. C. Sandberg. A three-dimensional computational study of the aerodynamic mechanisms of insect flight. *J. Exp. Biol.*, 205:1507–1518, 2002.

[93] K. Ramesh, A. Gopalarathnam, M. Ol, K. Granlund, and J. Edwards. Augmentation of invisid airfoil theory to predict and model 2d unsteady vortex dominated flows. *AIAA Paper*, pages 2011–3578, 2011.

[94] D. Rempfer. On low-dimensional galerkin models for fluid flow. *Theor. Comput. Fluid Dyn.*, 14:75–88, 2000.

[95] D. Rempfer. Low-dimensional modeling and numerical simulation of transition in simple shear flows. *Annu. Rev. Fluid Mech.*, 35:229–265, 2003.

[96] M. J. Ringuette, M. Milano, and M. Gharib. Role of the tip vortex in the force generation of low-aspect-ratio normal flat plates. *J. Fluid Mech.*, 581:453–468, 2007.

[97] N. Rott. Diffraction of a weak shock with vortex generation. *J. Fluid Mech.*, 1:111–128, 1956.

[98] P. G. Saffman and J. S. Sheffield. Flow over a wing with an attached free vortex. *Studies Appl. Math.*, 57:107–117, 1977.

[99] S. P. Sane. The aerodynamics of insect flight. *J. Exp. Biol.*, 206:4191–4208, 2003.

[100] T. Sarpkaya. An inviscid model of two-dimentional vortex shedding for transient and asymptotically steady separated flow over an inclined plate. *J. Fluid Mech.*, 68:109–128, 1975.

[101] T. Sarpkaya. Computational methods with vortices - the 1988 freeman scholar lecture. *Trans. ASME: J. Fluids Engng Trans.*, 111:5–52, 1989.

[102] T. Sawada and T. Hisada. Fluid-structure interaction analysis of the two-dimensional flag-in-wind problem by an interface-tracking ale finite element method. *Comput. Fluids*, 36:136–146, 2007.

[103] R. K. Shukla and J. D. Eldredge. An inviscid model for vortex shedding from a deforming body. *Theor. Comput. Fluid Dyn.*, 21:343–368, 2007.

[104] W. Shyy, H. Aono, S. Chimakurthi, P. Trizila, C.-K. Kang, C. Cesnik, and H. Liu. Recent progress in flapping wing aerodynamics and aeroelasticity. *Prog. Aerosp. Sci.*, 46:284–327, 2010.

[105] W. Shyy, M. Berg, and D. Ljungqvist. Flappping and flexible wings for biological and micro air vehicles. *Prog. Aerosp. Sci.*, 35:455–505, 1999.

[106] G. R. Spedding and T. Maxworthy. The generation of circulation and lift in a rigid two-dimensional fling. *J. Fluid Mech.*, 165:247–272, 1986.

[107] R. B. Srygley and A. L. R. Thomas. Unconventional lift-generating mechanisms in free-flying butterflies. *Nature*, 420:660–664, 2002.

[108] M. Sun and J. Tang. Unsteady aerodynamic force generation by a model fruit fly wing in flapping motion. *J. Exp. Biol.*, 205:55–70, 2002.

[109] S. Sunada, K. Kawachi, I. Watanabe, and A. Azuma. Fundamental analysis of three-dimensional 'near fling'. *J. Exp. Biol.*, 183:217–248, 1993.

[110] K. Taira and T. Colonius. The immersed boundary method: a projection approach. *J. Comput. Phys.*, 225:2118–2137, 2007.

[111] A. A. Tchieu, A. T. Kutay, J. A. Muse, and A. Leonard. Validation of a low-order model for closed-loop flow control enable flight. In *4th Flow Control Conference, 23-26 June 2008, Seattle, Washington*, 2008-3863, 2008.

[112] A. A. Tchieu and A. Leonard. A discrete-vortex model for the arbitrary motion of a thin airfoil with fluidic control. *J. Fluid. Struct.*, 27:680–693, 2011.

[113] F.-B. Tian, H. Dai, H. Luo, J. F. Doyle, and B. Rousseau. Fluid-structure interaction involving large deformations: 3D simulations and applications to biological systems. *J. Comput. Phys.*, 258:451–469, 2014.

[114] J. Toomey and J. D. Eldredge. Numerical and experimental study of the fluid dynamics of a flapping wing with low order flexibility. *Phys. Fluids*, 20:073603, 2008.

[115] G. Triantafyllou, M. Triantafyllou, and M. Grosenbaugh. Optefficiency development in oscillating foils with application to fish propulsion. *J. Fluid. Struct.*, 7:205–224, 1993.

[116] M. Triantafyllou, G. Triantafyllou, and D. Yue. Hydrodynamics of fishlike swimming. *Annu. Rev. Fluid Mech.*, 32:33–53, 2000.

[117] M. S. Triantafyllou, G. S. Triantafyllou, and R. Gopalkrishnan. Wake mechanics for thrust generation in oscillating foils. *Phys. Fluids*, 3:2835–2837, 1991.

[118] H. S. Udaykumar, R. Mittal, P. Rampunggoon, and A. Khanna. A sharp interface cartesian grid method for simulating flows with complex moving boundaries. *J. Comput. Phys.*, 174:345–380, 2001.

[119] D. Vainchtein and I. Mezić. Vortex-based control algorithms. *Lect. Notes. Contr. Inf.*, 330:189–212, 2006.

[120] C. van den Berg and C. P. Ellington. The three-dimensional leading-edge vortex of a 'hovering' model hawkmoth. *Phil. Trans. R. Soc. Lond. B*, 352:329–340, 1997.

[121] J. Vierendeels, K. Dumont, and P. R. Verdonck. A partitioned strongly coupled fluid-structure interaction method to model heart valve dynamics. *J. Comput. Appl. Math*, 215:602–609, 2008.

[122] T. von Karman and W. R. Sears. Airfoil theory for non-uniform motion. *J. Aeronaut. Sci*, 5:379–390, 1938.

[123] H. Wagner. Über die entstehung des dynamicschen auftriebes von tragflügeln. *Z. agnew. Mat. Mech*, 5:17–35, 1925.

[124] C. Wang and J. D. Eldredge. Low-order phenomenological modeling of leading-edge vortex formation. *Theor. Comput. Fluid Dyn.*, 27:577–598, 2013.

[125] Z. J. Wang. Vortex shedding and frequency selection in flapping flight. *J. Fluid Mech.*, 410:323–341, 2000.

[126] Z. J. Wang, J. M. Birch, and M. H. Dickinson. Unsteady forces and flows in low Reynolds number hovering flight: two-dimensional computations *vs* robotic wing experiments. *J. Exp. Biol.*, 207:449–460, 2004.

[127] T. Weis-Fogh. Quick esitmates of flight fitness in hovering animals, including novel mechanisms for lift production. *J. Exp. Biol.*, 59:169–230, 1973.

[128] T. Weis-Fogh and M. Jensen. Biology and physics of locust flight. i. basic principles in insect flight. a critical review. *Phil. Trans. R. Soc. Lond. B*, 239:415–458, 1956.

[129] P. J. Wilkin and M. H. Williams. Comparison of the aerodynamic forces on a flying sphingid moth with those predicted by quasi-steady theory. *Physiol. Zool.*, 66:1015–1044, 1993.

[130] A. P. Willmott, C. P. Ellington, and A. L. R. Thomas. Flow visualization an dunsteady aerodynamics in the flight of the hawkmoth, *Manduca sexta*. *Phil. Trans. R. Soc. Lond. B*, 352:303–316, 1997.

[131] G. S. Winckelmans and A. Leonard. Contributions to vortex particle methods for the computation of three-dimensional incompressible unsteady flows. *J. Comput. Phys.*, 109:247–273, 1993.

[132] T. Ye, R. Mittal, H. S. Udaykumar, and W. Shyy. An accurate cartesian grid method for viscous incompressible flows with complex immersed boundaries. *J. Comput. Phys.*, 156:209–240, 1999.

[133] L. Zannetti and A. Iollo. Passive control of the vortex wake past a flat plate at incidence. *Theor. Comput. Fluid Dyn.*, 16:211–230, 2003.

[134] L. J. Zhang and J. D. Eldredge. A viscous vortex particle method for deforming bodies with application to biolocomotion. *Int. J. Numer. Mech. Fluids*, 59:1299–1320, 2009.

[135] L. Zhu and C. S. Peskin. Simulation of a flapping flexible flilament in a flowing soap film by the immersed boundary method. *J. Comput. Phys.*, 179:452–468, 2002.